International Journal of Optics

Advances in Lasers and Optical Amplifiers: Materials, Components, and Systems

Guest Editors: Francesco Prudenzano, Frédéric Smektala, and Luciano Mescia

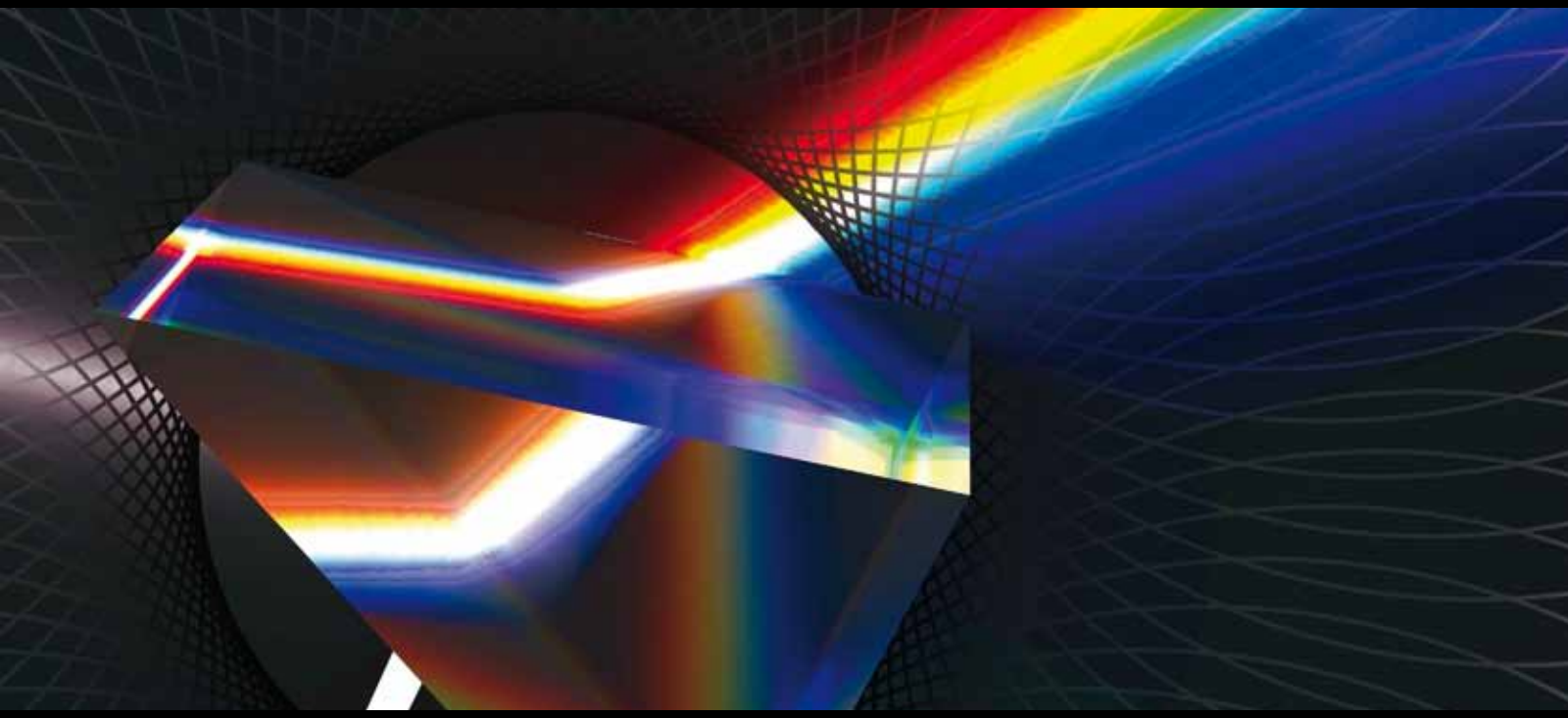

Advances in Lasers and Optical Amplifiers: Materials, Components, and Systems

International Journal of Optics

Advances in Lasers and Optical Amplifiers: Materials, Components, and Systems

Guest Editors: Francesco Prudenzano, Frédéric Smektala, and Luciano Mescia

Editorial Board

Contents

Hindawi Publishing Corporation
International Journal of Optics
Volume 2012, Article ID 807052, 2 pages
doi:10.1155/2012/807052

Editorial

Advances in Lasers and Optical Amplifiers: Materials, Components, and Systems

Francesco Prudenzano,[1] Frédéric Smektala,[2] and Luciano Mescia[1]

[1] *Dipartimento di Ingegneria Elettrica e dell'Informazione (DIEI), Politecnico di Bari, Via E. Orabona 4, 70125 Bari, Italy*
[2] *Laboratoire Interdisciplinaire Carnot de Bourgogne (ICB), UMR 6303 CNRS-Université de Bourgogne, 9 Avenue, Alain Savary, BP 47870, 21078 Dijon, France*

Correspondence should be addressed to Francesco Prudenzano, prudenzano@poliba.it

Received 6 November 2012; Accepted 6 November 2012

During the last decades a lot of research activities in the field of photonics have been accomplished and today there is a disruptive revolution underway where the photons are used to transmit, store, and process information. Laser and optical amplifier technology plays an important role in these events. In particular, the advances in lasers and optical amplifiers, enabling novel, powerful and exciting applications are based on research results arising from different investigation fields. This special issue is an example of these interdisciplinary contributions to the state of the art of optical amplification. Microresonators, interferometry, accurate modeling, grating, nonlinear optics, and novel materials are the subjects included in the volume.

In the paper entitled "*Modeling of mid-IR amplifier based on an erbium-doped chalcogenide microsphere*" the authors illustrate the design of an optical amplifier based on a tapered fiber and an Er^{3+}-doped chalcogenide microsphere. The obtained simulation results demonstrate that a high-efficiency mid-IR amplification can be obtained by using a quite small microsphere. The low threshold power and the high gain in the mid-IR suggest interesting application in sensing.

The paper "*Light combining for interferometric switching*" describes a novel switching device based on three input phase modulation ports. The interferometric switching as a routing method in sequence of coupled optical microresonators is investigated. Extended appendices facilitate the explanation of the implemented model. The proposed interferometer device shows the possibility to control a lightwave signal with the phase of another signal with interesting and feasible applications.

The paper "*Detailed theoretical model for adjustable gain-clamped semiconductor optical amplifier*" depicts the modeling and the experimental characterization of an adjustable gain-clamped semiconductor optical amplifier (AGC-SOA). The simulations agree very well with the experimental results. The proposed device could operate as power equalizer and linear amplifier in packet-based dynamic systems such as passive optical networks (PONs).

"*High-energy passive mode-locking of fiber lasers*" is a comprehensive study of achieving high-energy pulses in a ring cavity fiber laser, passively mode-locked by a series of waveplates and a polarizer. The obtained results may be used as practical guidelines for designing high-power lasers.

In the paper "*Tunable single-longitudinal-mode high-power fiber laser*" the authors show a novel CW tunable, high-power, single-longitudinal-mode fiber laser. A tunable fiber Bragg grating for wavelength selection is exploited. Due to the narrow linewidth and high output power, this laser could find applications in developing sensor based on nonlinear effects such as stimulated Brillouin scattering.

The paper "*New trends in amplifiers and sources via chalcogenide photonic crystal fibers*" is a review on amplification and lasing via rare earth doped chalcogenide photonic crystal fibers. Materials, devices, and feasible applications in the mid-IR are mentioned.

Acknowledgments

The guest editors are pleased and honored to submit this special issue to Hindawi Publishing Corporation and

thank all the authors and reviewers for their valuable contribution.

Francesco Prudenzano
Frédéric Smektala
Luciano Mescia

Hindawi Publishing Corporation
International Journal of Optics
Volume 2012, Article ID 575818, 8 pages
doi:10.1155/2012/575818

Review Article

New Trends in Amplifiers and Sources via Chalcogenide Photonic Crystal Fibers

L. Mescia,[1] F. Smektala,[2] and F. Prudenzano[1]

[1] *Dipartimento di Ingegneria Elettrica e dell'Informazione (DIEI), Politecnico di Bari, 70125 Bari, Italy*
[2] *Laboratoire Interdisciplinaire Carnot de Bourgogne (ICB), UMR 5209 CNRS-Université de Bourgogne, 21078 Dijon, France*

Correspondence should be addressed to F. Prudenzano, prudenzano@poliba.it

Received 19 July 2012; Revised 26 October 2012; Accepted 27 October 2012

Academic Editor: Dragomir Neshev

Rare-earth-doped chalcogenide glass fiber lasers and amplifiers have great applicative potential in many fields since they are key elements in the near and medium-infrared (mid-IR) wavelength range. In this paper, a review, even if not exhaustive, on amplification and lasing obtained by employing rare-earth-doped chalcogenide photonic crystal fibers is reported. Materials, devices, and feasible applications in the mid-IR are briefly mentioned.

1. Introduction

The current laser market does not provide efficient sources in most of the mid-IR spectrum. In particular, the shortage in availability of powerful, coherent, robust, and compact laser sources at wavelength longer than 3 microns constitutes the major obstacle to a widespread advancement of mid-IR science and technology. During the last decades, a number of mid-IR laser sources have been developed but they have shown low conversion efficiency, limited beam quality; moreover they are complex, bulky, and expensive [1, 2]. In fact, the unfavorable temperature dependence of thermal and thermooptical parameters set limitations to the power scalability since the large heat load can lead to glass fracture, and the strong thermal lensing can promote pronounced spherical aberrations [1, 2].

Over the last years, the continuing technological progress and innovations in lasing materials, in fabrication of sophisticated optical fibers and of beam-shaped high-power diode lasers have positioned the optical fiber technology as one of the most promising ones in order to develop a new generation of mid-IR sources [1, 2]. The compact footprint size, the rather cheap and simple maintenance, and the higher lasing efficiency make mid-IR fiber lasers attractive for ICT, industrial, and medical applications.

Silica-based fiber lasers have proved to be both efficient and compact sources in the near-IR wavelength range, but they are not able to provide mid-IR wavelengths because of their high phonon energy and their limited transparency beyond the wavelength of 2 μm. Various watt-level rare-earth-doped ZBLAN fiber lasers, oscillating in the spectral region around 2.7 microns in the CW mode, have been developed [1, 3]. Recently, the highest single-mode output power of about 20 W has been obtained with an Er^{3+}-doped fluoride glass fiber laser emitting at 2.8 μm [4]. In particular, a passively cooled setup, a 976 nm pump source, and a truncated circular pump cladding were employed. Moreover, a slope efficiency higher than the Stokes efficiency was achieved. This is the experimental confirmation of the pump energy recycling in a fiber laser. Ho^{3+}-doped ZBLAN fiber is able to oscillate at 2.9 microns, but one of its significant shortcomings is the lack of ground state absorption that overlaps with conventional high-power pump sources [5]. As a result, the sensitization of Ho^{3+} with Yb^{3+} or Pr^{3+} has been implemented in order to access the convenient absorption bands and to achieve higher output power without the costly requirement of an intermediate laser system [6–8]. Dy^{3+}-doped ZBLAN fiber lasers also can oscillate at 2.9 micron, but their output power and slope efficiency are low [9]. The operation of lasers at 3.22, 3.45, and 3.95 microns has

been obtained by doping ZBLAN fiber with holmium and erbium, but an increasing of the pump threshold and some saturation of the output power have been observed [10–13]. This problem combined with the use of unconventional pump sources has prevented the full utilization of these systems. As a consequence, it is clear that the fiber laser technology based on oxide and fluoride glasses is only useful for laser transitions up to 3 microns.

Advances in the fabrication of rare-earth-doped optical fibers based on chalcogenide glasses have dramatically pushed progress on active devices operating at wavelengths higher than 3 microns [14–18]. Chalcogenide glasses are chemically and mechanically durable, have a low toxicity, possess reasonably large glass-forming regions, and can be fabricated into low-loss fibers. Moreover, their high refractive index ($2 \div 3$) and low phonon energy ($250 \div 400\,\mathrm{cm}^{-1}$) result in a larger radiative decay rates, high absorption and emission cross sections of radiative electronic transitions, and low nonradiative multiphonon relaxation rates. These properties result in high quantum efficiency [14]. The electronic energy levels of rare-earth ions allow a number of useful transitions from 2 to 12 microns. However, only a few glass hosts can efficiently activate transitions at longer wavelengths. The low phonon energy of the chalcogenide glasses enables an efficient laser transition between closely spaced electronic energy levels allowing many IR transitions. As an example, chalcogenide glasses make possible the radiative transition from $^4I_{11/2}$ to $^4I_{13/2}$ erbium energy levels, quenched by the multiphonon decay in silica glasses, and from $^4I_{9/2}$ to $^4I_{11/2}$, quenched in fluoride glasses. Furthermore, the high rare earth solubility into several chalcogenide glasses facilitates the fabrication of efficient rare earth doped lasers and amplifiers since ion clustering and concentration quenching effects are minimized.

The chalcogenide glasses have been used to fabricate conventional optical fibers doped with a number of rare-earth ions for mid-IR luminescence [14, 15]. Unfortunately, the technology used to fabricate low-loss single-mode chalcogenide fibers in step-index configuration requires significant care and expertise. In fact, the different physical properties of the core and cladding glasses promote crystallization, bubbles, contamination at the core/cladding interface, and core ellipticity. Moreover, it is difficult to fabricate step-index fibers having very small and very large mode area, because a fine control of the refractive index of the core and cladding cannot be obtained. In order to overcome these problems, the use of photonic crystal fiber (PCF) technology is a feasible and attractive solution. In fact, it eliminates the problems induced by the core/cladding interface since a single materials is used. In addition, the single-heating step used to make the PCFs allows both the reduction of the crystallization problems and fiber losses. Lastly, the high refractive index of the chalcogenide glass enables a better confinement of the light by using only a few rings of air holes [19, 20]. The first chalcogenide PCF made of only one ring of air holes was presented in [20]. Recently, progresses on the $Ga_5Ge_{20}Sb_{10}S_{65}$ (2S2G) fiber fabrication using the "Stack and Draw" procedure were illustrated in order to build complex and regular PCFs made of several rings of holes [19]. Small-core PCFs made of chalcogenide glass 2S2G with single-mode operation for wavelength higher than 1550 nm have been obtained [21]. Moreover, the fabrication, linear and nonlinear optical characterization, and numerical simulations in the middle infrared of PCFs in different kinds of chalcogenide glass have been presented [16, 17, 19].

2. Chalcogenide Photonic Crystal Fiber for Midinfrared Amplification

A number of different rare-earth elements, such as erbium, ytterbium, praseodymium, neodymium, samarium, and thulium, can be used to fabricate fiber amplifiers operating at different wavelengths. In particular, erbium doped fiber amplifiers (EDFAs) are nowadays available for long-haul communication systems, allowing to abandon the use of optoelectronic and electrooptical conversions of signals. These devices are very attractive because of their high gain, wide optical bandwidth, high output saturation, near quantum-limited noise, low insertion losses, high reliability and compactness, polarization independence, immunity to saturation-induced and to crosstalk, and possibility of choosing the pumping laser diode at 980 nm or 1480 nm wavelengths.

Although this kind of technology is mature and widely employed, further researches are needed to obtain amplifiers with higher gain efficiency. The optimization of fiber transversal section is crucial to improve the amplifier performance in terms of gain, noise, and output power characteristics as well as device compactness and pump power consumption. In fact, in the rare-earth-doped devices, the fiber geometry strongly affects the pump intensity, the overlap of the pump, and the signal propagation modes with the doped core. As a consequence, it can lead to the suppression of the amplified spontaneous emission (ASE), the power scaling and the maximum inversion of rare-earth ions as well as to the reduction of the fiber length.

Sophisticated design methods and fabrication techniques have been developed to construct single-mode optical fiber amplifiers. To this aim, a fine control of refractive index profile of both core and cladding as well as more design flexibility of fiber cross section is needed. The conventional optical fibers are not able to completely respond to these requirements, while the PCF technology seems to be an attractive solution. A PCF is typically characterized by a transverse crystal lattice (usually periodically arranged) containing either air holes or glass strand running along the fiber axis. As a consequence, these fibers are different with respect to the conventional ones, and the main difference is in the refractive index profile of both core and cladding regions. The unique properties of PCFs are extremely attractive for a variety of rare-earth-doped fibers and devices because they enable more flexibility to control the interaction of both pump and signal modes with the rare-earth-doped host. In addition, the stacking procedure used to fabricate such fibers offers the possibility to accurately confine the rare-earth dopant in the central region of the fiber where the pump and signal intensity peaks occur [15, 22, 23].

In addition to the solid-core PCF, typically exploited for both optical amplification and nonlinear applications, hollow-core photonic-bandgap-chalcogenide fibers for high power mid-IR laser transmission and power delivery have been successfully fabricated [15, 24]. As an example, Figure 1 shows two prototypes made by Naval Research Laboratory, Washington, USA [15], to fabricate (a) photonic-bandgap fiber structures and (b) PCF structures. Moreover, the optimization procedure of both the cladding structure and the core size to obtain the overall losses lower than the material ones, the realization of a hollow-core PCF having six rings of air holes, and the comparison between experimental results and simulations are illustrated in [23].

The well-known PCF technology, allowing endless single mode propagation and group velocity control, via a proper design, exhibits further intriguing potentials coupled to the broad-bandwidth transmission, typical of chalcogenide glasses. In addition, the high quantum efficiencies of the mid-IR transitions make rare-earth-doped chalcogenide fibers attractive alternatives to obtain black-body sources for generating emission in the 3–5 μm wavelength range.

As an example, Figure 2 shows a diode-pumped Pr^{3+}-doped selenide glass fiber source, demonstrating broadband emission in the wavelength range 3–5 μm [15].

On the basis of the optical and spectroscopic parameters measured on fabricated Er^{3+}-doped solid core chalcogenide PCFs, the design of active devices in both near and medium-infrared wavelength range has been numerically performed [25–27]. The feasibility of Er^{3+}-doped, 2S2G chalcogenide glass has been demonstrated in order to obtain a high-performance optical amplifier in the third band of fiber-optic communication [25]. In particular, the gain and noise figure performances have been evaluated by varying numerous parameters such as doping region radius, erbium concentration, signal wavelength, input pump, and signal power. Figure 3(a) shows the image of the fabricated PCF considered in the simulations. Figures 3(b)–3(d) show the dependence of the optimal gain, optimal length, and noise figure as a function of the signal wavelength for the three different input pump powers. The effect of the variation of the erbium concentration, radius of the doped region, and the excited state absorption (ESA) at the pump wavelength on the amplifier characteristics has been investigated, too. In particular, the calculated optical gain of the optimized PCF amplifier, 2.79 m long, is close to 23 dB at the signal wavelength of 1.538 μm, by using a pump power of 200 mW and a signal power of 0.1 μW. This result indicates that the proposed fiber amplifier could be a good candidate in optical communication networks and systems. Therefore, by considering that (i) the high refractive index and the low phonon energy of the chalcogenide glass increase the efficiency of transitions among rare-earth energy levels; (ii) the excellent rare-earth solubility in chalcogenide glass allows high dopant concentration, without ion clustering and concentration quenching effects, fiber amplifiers based on chalcogenide glasses, operating at 1.5 μm, exhibit higher pump conversion efficiency and shorter fiber lengths than those based on silicate glasses.

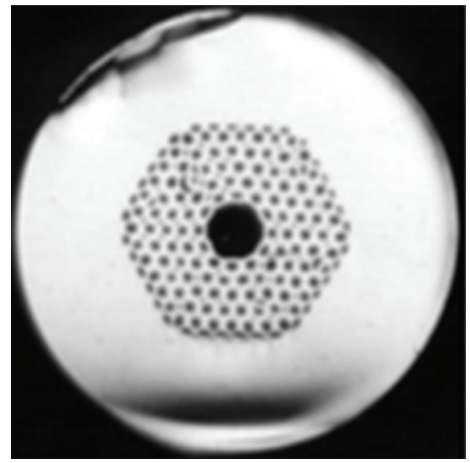

(a)

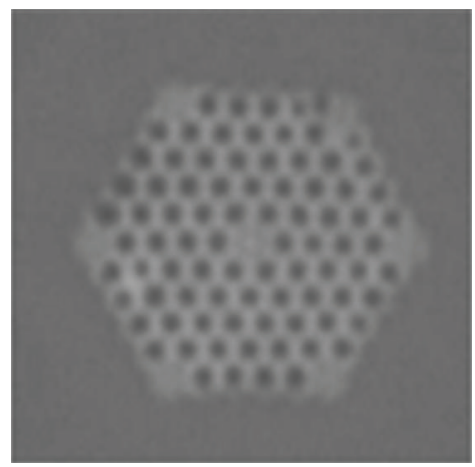

(b)

Figure 1: Attempts made by Naval Research Laboratory, Washington, USA, to fabricate (a) photonic bandgap fiber structures and (b) PCF structures by exploiting chalcogenide glasses [14].

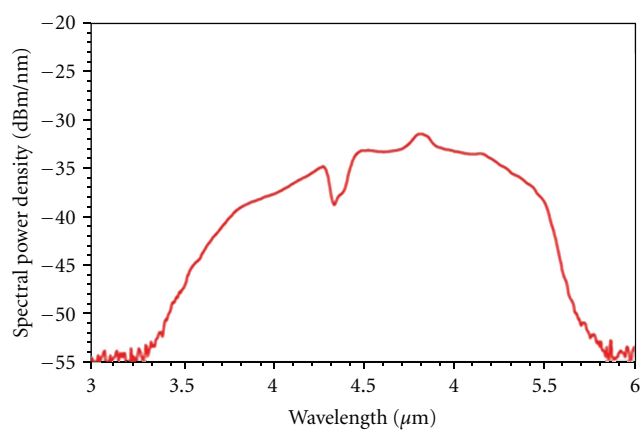

Figure 2: Pr^{3+}-doped chalcogenide fiber source with broadband emission in the 3–5 μm wavelength region [15].

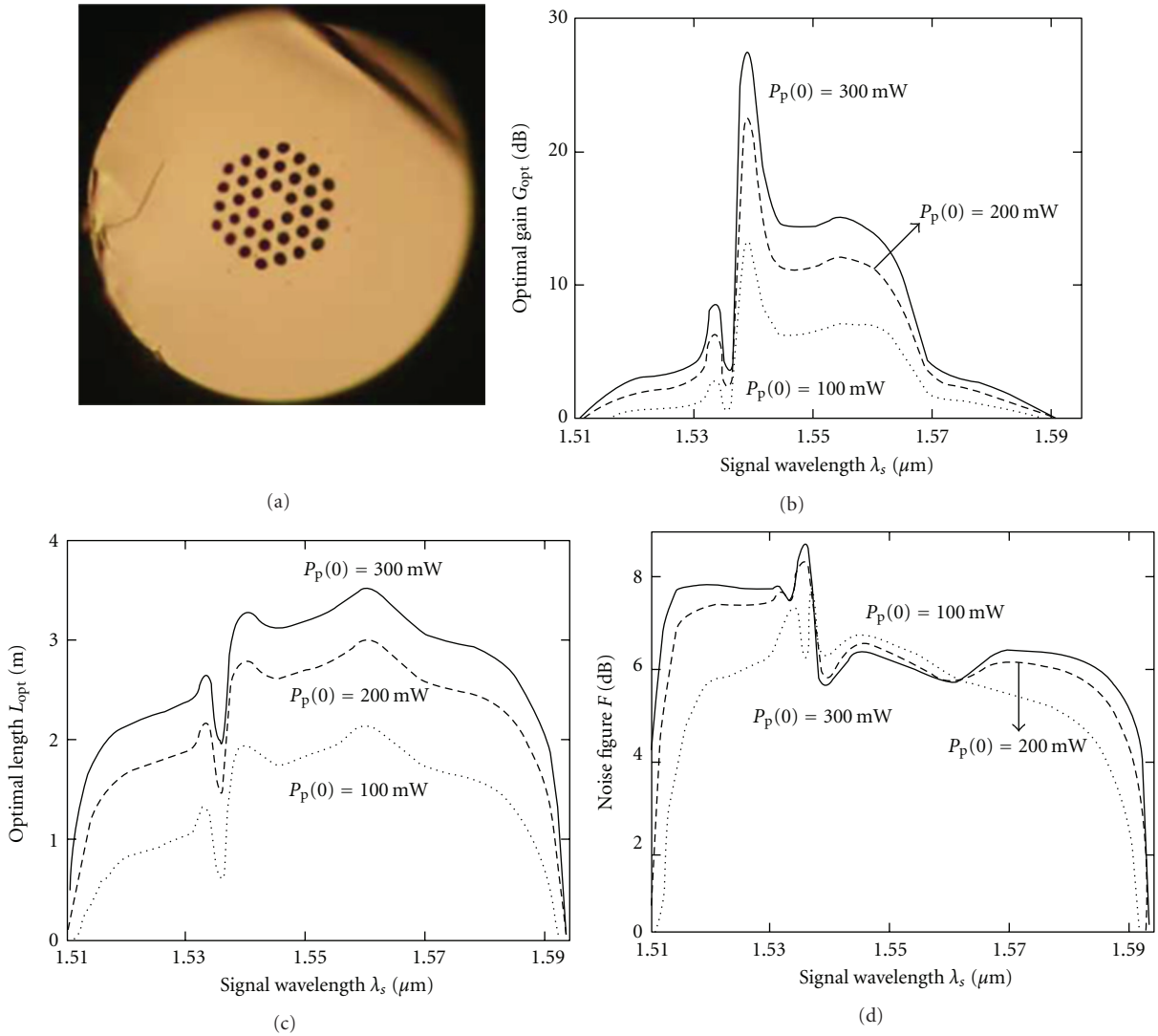

Figure 3: (a) SEM image of the fabricated chalcogenide PCF, (b) optimal gain G_{opt}, (c) optimal length L_{opt}, and (d) noise figure F versus signal wavelength λ_s for three different input pump power levels: $P_p(0)$ = 100 mW (dot curve), $P_p(0)$ = 200 mW (broken curve), and $P_p(0)$ = 300 mW (full curve). Input signal power $P_s(0) = 0.1\,\mu$W, erbium concentration $N_{Er} = 5.76 \times 10^{24}$ ions/m^3, and doped region radius $R_d = 5\,\mu$m [19, 25].

Moreover, simulation results regarding the propagation of pulse in Er^{3+}-doped, $Ga_5Ge_{20}Sb_{10}S_{65}$ chalcogenide glass amplifiers have been reported in a recent work [28]. The authors studied the effect of gain saturation on the propagation of fundamental dark soliton and verified that the dark soliton is more stable in the presence of gain saturation and gain dispersion effects. In particular, they showed that (i) bright solitons with energy less than the saturation energy are divided into many subpulses with time symmetry, (ii) bright solitons with energy close to the saturation energy are divided into many subpulses without time symmetry, and (iii) dark solitons in the absence of the gain saturation are amplified without creating any subpulses. These properties make possible the use of chalcogenide glasses for designing all optical devices.

Recently, a detailed spectroscopic study of Er^{3+}-doped 2S2G glass has been illustrated [27]. This doped glass (i) facilitates the optical fiber drawing, since it presents suitable thermo-mechanical properties, (ii) provides a better solubilization, since it contains gallium, and (iii) enables efficient $^4I_{11/2} \rightarrow {}^4I_{13/2}$ (2.7 μm) and $^4I_{9/2} \rightarrow {}^4I_{11/2}$ (4.5 μm) mid-IR transitions. The radiative lifetime of $^4F_{9/2}$, $^4I_{9/2}$, $^4I_{11/2}$, and $^4I_{13/2}$ energy levels and the related branching ratios are determined. The estimation of Er^{3+} emission cross section in the mid-IR spectral range was 2.85×10^{-25} m^2 at 4.6 μm. The $^4I_{9/2}$ radiative quantum efficiency was estimated to be 64%. The propagation of fluorescence signals around 2.7 μm and, for the first time, around 4.6 μm was clearly observed in two 2G2S fibers doped with erbium ions under laser pumping at 804 nm. In Figure 4 are reported the fluorescence intensities in (a) near-IR and (b) mid-IR emission bands with 804 nm laser pumping of a 1000 ppm Er^{3+}-doped 2S2G glass.

The design and refinement criteria pertaining to the chalcogenide erbium-doped PCF amplifier based on a 2S2G

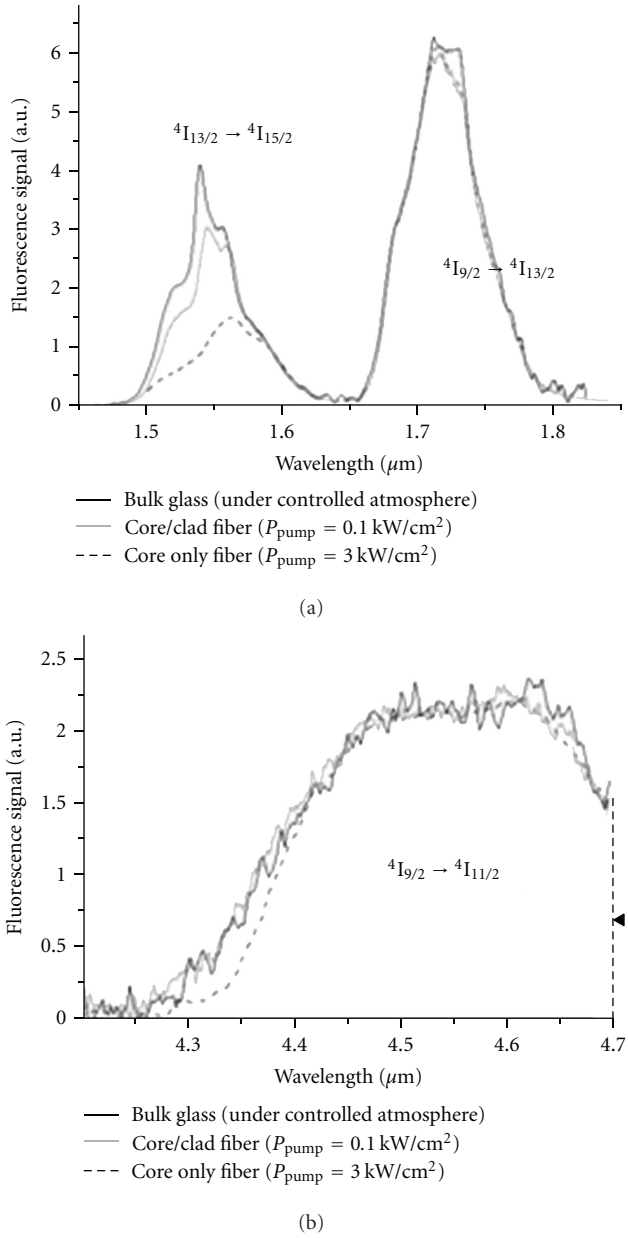

Figure 4: Fluorescence spectra of 1000 ppm Er-doped 2S2G glasses pumped at 804 nm. (a) 1.5 and 1.7 μm emissions and (b) 4.5 μm emission from a bulk glass, 20 cm of a 400 μm diameter monoindex fiber, and 20 cm of a 60 μm core diameter double index fiber [24].

glass, allowing the operation at 4.5 μm, were illustrated in [26]. The absorption cross-section spectrum employed in the simulation has been experimentally measured. In particular, the fluorescence spectrum of Er^{3+} ions around 4.5 m is experimentally recorded for a 10000 ppm-doped chalcogenide glass and the emission cross section of the $^4I_{9/2} \rightarrow {}^4I_{11/2}$ transition is then calculated using the Fuchtbauer-Ladenburg relation. High-gain PCF amplifier with gain values close to 30 dB, with a low value of noise figure and reduced fiber length has been theoretically demonstrated. A good amplification in the range 4.4–4.7 μm was calculated; thus the amplifier, opportunely optimized, could be employed in multichannel amplification application. These theoretical and experimental results demonstrate the suitability and goodness of the 2S2G chalcogenide glass as an attractive candidate to construct fiber amplifiers operating in the mid-IR spectral region.

The technological improvement in drawing chalcogenide fibers is an important research goal since soft glasses exhibit several drawbacks with respect to more conventional materials as silica or fluoride glasses. As an example, a new route to chalcogenide glass *microstructured optical fibers* (MOFs) was illustrated in [29]. The work demonstrated a flexible technology of great potential for new fiber devices from the far-visible to midinfrared. The approach was both scalable and adaptable. In particular, an As_{40} Se_{60} glass tube of 3.8 mm/10 mm internal diameter/outer diameter was cast by rotation. Into this tube were stacked eight fibers: one As Se fiber was located centrally to obtain the core; seven Ge As Se-As Se core-cladding (core-clad) fibers that were stacked around the core fiber. The aforesaid core-clad fibers were drawn from a preform prepared by coextrusion. The microstructured preform was drawn down to MOF.

The refinement of novel technological routes, developed even in other application fields, for example nonlinear optics, could find application also in the field of lasing\amplification. In [30] the authors presented a detailed design of a highly nonlinear chalcogenide core tellurite cladding composite microstructured fiber. The fabrication procedure for the microstructured fiber was illustrated. The applications to nonlinear phenomena were demonstrated by mean of a supercontinuum generation experiment. The application of nonlinear optics to lasing is apparent in the case of Raman amplification. The operation of a chalcogenide glass Raman fiber laser was reported in [31]. In the aforesaid work, to mitigate photoinduced effects and minimize impurity absorption, a 2051 nm Tm^{3+}-doped silica fiber laser was employed as the pump source. First Stokes emission at 2062 nm was produced, an output power of 0.64 W and a slope efficiency of ~66%. Second Stokes output at 2074 nm was produced when the fiber length was extended.

3. Chalcogenide Photonic Crystal Fiber for Midinfrared Sources

In medical and surgical applications the output laser properties such as power and wavelength are important aspects to be recognized. Beyond these ones, other practical quantities such as size, maintenance level, and input power requirements are essential features to be taken into account for a widespread use of the laser in the medical community. Moreover, other laser characteristics such as beam quality may be important for applications requiring precise and efficient ablation of hard and soft biological materials [32–34].

The recent technological progress in the development of lasing materials, in the fabrication of sophisticated optical fibers, and in the fabrication of beam-shaped high-power

diode laser has positioned the infrared fiber laser as one of the most promising technologies in bioscience and medicine. In surgery: cardiology bloodless operations, on abdominal and thoracic organs, skull and brain microsurgery, corneal surgery. In diagnostics: endoscopic investigations, confocal scanning microscopy and optical coherence tomography. In therapy: the treatment of cancer, spider veins, and vascular dysfunction. In cosmetics and aesthetic medicine: smoothing wrinkles, resurfacing the skin, and bleaching tattoos [35]. Therefore, due to their inherent flexibility of physical principles and design, fiber lasers have enormous potential to bring new opportunities to biophotonics and biosciences.

Generally, a lot of medical applications require the mid-infrared wavelengths, in the range $2 \div 10\,\mu$m. In particular, laser emitting in the 2-3 μm range has gained, in recent years, strong attention for accurate cutting, welding, removing, and coagulating of soft and hard biological tissues. Moreover, mid-IR laser is a promising technology for the study of biomolecules because most of these ones have a specific absorption in the mid-IR wavelength range, and the photon energies are an order of magnitude lower than those of UV lasers. Significant efforts have been done to develop mid-IR fiber lasers and amplifiers, but the high cost of fabricating fibers with sufficiently low losses in such wavelength range has slowed down the research efforts in this field. This is probably due to a lack of host materials having wide optical transparency, good drawing ability, low phonon energies of the glass matrix, good rare-earth solubility, suitable environmental durability, and mechanical properties.

Advances in the development of rare-earth-doped optical fiber based on chalcogenide glasses have dramatically pushed progress in mid-IR laser devices. In particular, the good midinfrared transparency permits them to scan the entire spectral range of biomolecules and the chalcogenide glass resistance to the chemical corrosion results in good biocompatibility with biological components.

The feasibility of a novel Er^{3+}-doped chalcogenide PCF laser, operating at 4.5 μm, was shown [36]. In order to increase the pump efficiency, a theoretical investigation of an innovative cascade laser source operating at 4.5 m and 2.7 μm is performed by using the erbium ion concentration $N_{\mathrm{Er}} = 7 \times 10^{26}$ ions/m^3. Both erbium concentration and fiber length were optimized to provide the maximization of the output power for both two signal wavelengths. In particular, the numerical results indicated that a laser characterized by a slope efficiency close to the maximum theoretical one, low threshold pump power, short fiber length, and a wide tunability in the mid-IR wavelength range can be obtained. In conclusion, both the theoretical and experimental results demonstrated the suitability of the 2S2G chalcogenide glass as a very attractive candidate to construct fiber laser sources and amplifiers operating in the mid-IR spectral region. Moreover, the feasibility of a novel Er^{3+}-doped 2S2G chalcogenide fiber laser, pumped at the wavelength 806 nm, designed in order to obtain high performance at the wavelength 4.5 μm, is investigated in [37]. In particular, the developed numerical code takes

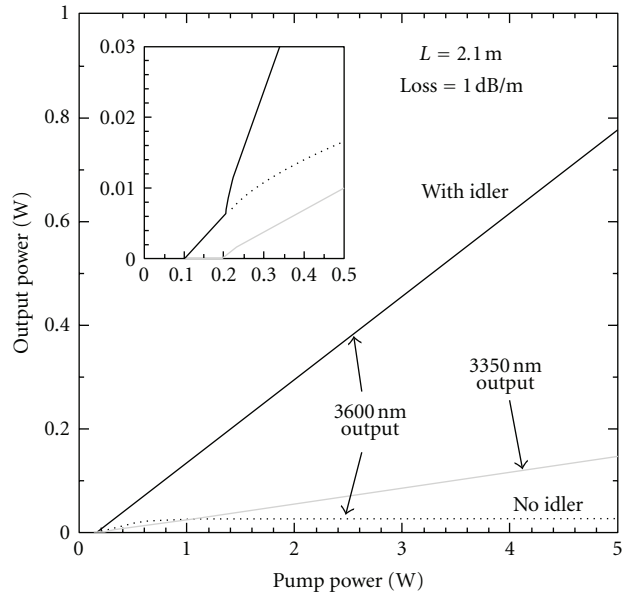

Figure 5: Simulated output power with respect to incident pump power. With idler output (dark solid curve) abruptly increases. With no idler (dotted curve) [39].

into account the erbium energy levels lifetimes, the emission and absorption cross section measured on 10000 ppm Er^{3+}-doped 2S2G preliminary sample. The large potential of chalcogenide glass was also highlighted in the review work [38], where it was briefly illustrated that the fiber laser configuration offers better beam quality than competing technologies, for example, than quantum cascade lasers and transition-metal-doped selenides, and more versatility for pulsed operation.

The performance of a continuous-wave Dy: GeAsGaSe chalcogenide glass fiber laser, in cascade configuration, operating at 4.2–4.7 m, was investigated via numerical modeling in [39]. Pump light at 1710 nm was coupled into the Dy: GeAsGaSe chalcogenide glass fiber. The Dy ions were promoted to the level $^6H_{11/2}$. Fluorescence from level $^6H_{11/2}$ to the level $^6H_{13/2}$ occurring between 4000 and 4800 nm was exploited to obtain the lasing via two fiber Bragg gratings. In addition, the other fluorescence from level $^6H_{13/2}$ to the ground state occurring between 2700 and 3400 nm and the simultaneous lasing were considered by using two additional fiber Bragg gratings with the aim to improve 4600 nm emission. Figure 5 illustrates the output power versus the input pump power for a fiber length $L = 2.1$ m and propagation loss of 1 dB/m at all wavelengths. The inset highlights that the slope efficiency strongly can be strongly increased when the idler reaches 0.2 W.

A better understanding of the local RE-ion environment to obviate unwanted nonradiative decay will permit to improve chalcogenide laser performance. Also a better understanding of the impact of host chalcogenide glass native defects on the doped RE-ion fluorescence could be a key element to obtain more efficient chalcogenide lasers.

It is well known that soft glasses as tellurite, bismuth-oxide-based glasses, and chalcogenide glasses have intrinsic nonlinearities from 10 to 100 times than those of silica glass [39]. Moreover, the Raman gain coefficients of chalcogenide glass fibers are very high, ∼300 times than that of silica fibers, and the Brillouin gain coefficient is more than 2 orders of magnitude higher than that of silica-based fibers. They show low linear absorption, low two-photon absorption, and fast response time because of the absence of the free-carrier effects [30]. As a result, optical fibers made of such glasses, especially, chalcogenide glasses, are highly applicable for generating mid-IR nonlinear phenomena, short active fiber devices and achieving fiber Raman and Brillouin lasers [30, 40–43].

Nonlinear optical processes such as four-wave mixing, parametric oscillation, and supercontinuum generation require high nonlinearity and zero or low group velocity dispersion for applying in the efficient low power, short-length fiber devices. Moreover, the group velocity dispersion is due by both the material and waveguide dispersion. Generally, because of the high refractive index, the dispersion of chalcogenide glasses originates mainly from the material dispersion and the zero-dispersion wavelength lies in the IR region, at longer wavelengths compared to silica and far from the wavelengths of conventional fiber-based pump lasers. Consequently, the use of nonsilica fibers to develop supercontinuum sources having an efficient spectral broadening up to the mid-IR often requires expensive and high-power pump lasers. The photonic crystal fiber technology seems to be a potential solution to these drawbacks since the design flexibility of the microstructure in the transverse plane can help the tuning of the chromatic dispersion, dispersion slope, relative dispersion slope, and zero-dispersion wavelength in a way which cannot be achieved by using conventional fibers. In fact, the number of holes, their sizes, shapes, orientations, and placements, as well as the nature of the bulk dielectric material and the refractive index of the inclusions can provide a number of possible variations enabling a fine control of the waveguide dispersion characteristics. In this way, the zero-dispersion wavelength can be tuned below 2 μm where cheaper diode-pumped solid-state lasers are commercially available. Recently, a midinfrared extension of supercontinuum has been experimentally demonstrated by using a suspended core chalcogenide fiber [44]. In particular, it has shown that by using a low-cost optical quasi-CW source at 1.53 μm, it is possible to extend a silica-based supercontinuum beyond 2.4 μm through the generation of a soliton gas inside an highly nonlinear silica fiber and its injection beyond the ZDW in a 50 cm-long chalcogenide suspended core PCF. Highly nonlinear chalcogenide core tellurite cladding composite microstructured fiber has been carefully designed and fabricated in order to achieve the zero-flattened chromatic dispersion with zero slope of the dispersion curve at 1.55 μm [30]. In particular, the nonlinear coefficient for the fabricated fiber is 9.3 $m^{-1}\,W^{-1}$ at 1.55 μm. In addition, a supercontinuum spectrum of 20 dB bandwidth covering 0.80–2.40 μm was generated by this fiber.

4. Conclusion

The progress and the challenges, in fabricating rare-earth-doped chalcogenide-glass fibers for developing midinfrared fiber amplifiers and lasers, have been reviewed. Potential applications of midinfrared fiber lasers have been recalled. In particular, biomedicine and sensing will be strongly favored by these devices. New communication and remote sensing systems operating in unexplored atmosphere wavelength windows could become feasible. Further efforts in technology and glass purity will permit to obtain more efficient amplification and lasing and to fabricate reliable devices for the market.

References

[1] M. Ebrahim-Zadeh and I. T. Sorokina, *Mid-Infrared Coherent Sources and Applications*, Springer, Barcelona, Spain, 2008.

[2] I. T. Sorokina and K. L. Vodopyanov, *Solid-State Mid-Infrared Laser Sources*, Springer, Berlin, Germany, 2003.

[3] X. Zhu and R. Jain, "10-W-level diode-pumped compact 2.78 μm ZBLAN fiber laser," *Optics Letters*, vol. 32, no. 1, pp. 26–28, 2007.

[4] D. Faucher, M. Bernier, G. Androz, N. Caron, and R. Vallée, "20 W passively cooled single-mode all-fiber laser at 2.8 μm," *Optics Letters*, vol. 36, no. 7, pp. 1104–1106, 2011.

[5] S. D. Jackson, "Midinfrared holmium fiber lasers," *IEEE Journal of Quantum Electronics*, vol. 42, no. 2, pp. 187–191, 2006.

[6] S. D. Jackson, "Single-transverse-mode 2.5 W holmium-doped fluoride fiber laser operating at 2.86 μm," *Optics Letters*, vol. 29, no. 4, pp. 334–336, 2004.

[7] S. D. Jackson, "High-power and highly efficient diode-cladding-pumped holmium-doped fluoride fiber laser operating at 2.94 μm," *Optics Letters*, vol. 34, no. 15, pp. 2327–2329, 2009.

[8] A. Diening, P. E. A. Möbert, E. Heumann, G. Huber, and B. H. T. Chai, "Diode-pumped cw lasing of Yb, Ho : KYF_4 in the 3 μm spectral range in comparison to Er : KYF_4," *Laser Physics*, vol. 8, no. 1, pp. 214–217, 1998.

[9] Y. H. Tsang, A. E. El-Taher, T. A. King, and S. D. Jackson, "Efficient 2.96 μm dysprosium-doped fluoride fibre laser pumped with a Nd:YAG laser operating at 1.3 μm," *Optics Express*, vol. 14, no. 2, pp. 678–685, 2006.

[10] J. Schneider, "Fluoride fibre laser operating at 3.9 μm," *Electronics Letters*, vol. 31, no. 15, pp. 1250–1251, 1995.

[11] C. Carbonnier, H. Többen, and U. B. Unrau, "Room temperature CW fibre laser at 3.22 μm," *Electronics Letters*, vol. 34, no. 9, pp. 893–894, 1998.

[12] H. Toebben, "CW lasing at 3.45 μm in erbium-doped fluorozirconate fibres," *Frequenz*, vol. 45, no. 9-10, pp. 250–252, 1991.

[13] J. Schneider, C. Carbonnier, and U. B. Unrau, "Characterization of a Ho^{3+}-doped fluoride fiber laser with a 3.9-μm emission wavelength," *Applied Optics*, vol. 36, no. 33, pp. 8595–8600, 1997.

[14] L. B. Shaw, B. Cole, P. A. Thielen, J. S. Sanghera, and I. D. Aggarwal, "Mid-wave IR and long-wave IR laser potential of rare-earth doped chalcogenide glass fiber," *IEEE Journal of Quantum Electronics*, vol. 37, no. 9, pp. 1127–1137, 2001.

[15] J. S. Sanghera, L. B. Shaw, and I. D. Aggarwal, "Chalcogenide glass-fiber-based mid-IR sources and applications," *IEEE*

Journal on Selected Topics in Quantum Electronics, vol. 15, no. 1, pp. 114–119, 2009.

[16] J. Fatome, C. Fortier, T. N. Nguyen et al., "Linear and nonlinear characterizations of chalcogenide photonic crystal fibers," *Journal of Lightwave Technology*, vol. 27, pp. 1707–1715, 2009.

[17] M. El-Amraoui, G. Gadret, J. C. Jules et al., "Microstructured chalcogenide optical fibers from As2S 3 glass: Towards new IR broadband sources," *Optics Express*, vol. 18, no. 25, pp. 26655–26665, 2010.

[18] A. P. Caricato, M. De Sario, M. Fernández et al., "Pulsed laser deposition of materials for optoelectronic applications," *Applied Surface Science*, vol. 197-198, pp. 458–462, 2002.

[19] L. Brilland, F. Smektala, G. Renversez et al., "Fabrication of complex structures of Holey Fibers in Chalcogenide glass," *Optics Express*, vol. 14, no. 3, pp. 1280–1285, 2006.

[20] T. M. Monro, Y. D. West, D. W. Hewak, N. G. R. Broderick, and D. J. Richardson, "Chalcogenide holey fibres," *Electronics Letters*, vol. 36, no. 24, pp. 1998–2000, 2000.

[21] F. Désévédavy, G. Renversez, L. Brilland et al., "Small-core chalcogenide microstructured fibers for the infrared," *Applied Optics*, vol. 47, no. 32, pp. 6014–6021, 2008.

[22] C. C. Wang, F. Zhang, Y. C. Lu et al., "Single-mode operations in the large flattened mode optical fiber lasers and amplifiers," *Journal of Optics A*, vol. 11, no. 6, Article ID 065402, 2009.

[23] A. Cucinotta, F. Poli, and S. Selleri, "Design of erbium-doped triangular photonic-crystal-fiber-based amplifiers," *IEEE Photonics Technology Letters*, vol. 16, no. 9, pp. 2027–2029, 2004.

[24] F. Désévédavy, G. Renversez, J. Troles et al., "Chalcogenide glass hollow core photonic crystal fibers," *Optical Materials*, vol. 32, no. 11, pp. 1532–1539, 2010.

[25] M. De Sario, L. Mescia, F. Prudenzano et al., "Feasibility of Er^{3+}-doped, $Ga_5Ge_{20}Sb_{10}S_{65}$ chalcogenide microstructured optical fiber amplifiers," *Optics and Laser Technology*, vol. 41, no. 1, pp. 99–106, 2009.

[26] F. Prudenzano, L. Mescia, L. Allegretti et al., "Simulation of mid-IR amplification in Er^{3+}-doped chalcogenide microstructured optical fiber," *Optical Materials*, vol. 31, no. 9, pp. 1292–1295, 2009.

[27] V. Moizan, V. Nazabal, J. Troles et al., "Er^{3+}-doped GeGaSbS glasses for mid-IR fibre laser application: synthesis and rare earth spectroscopy," *Optical Materials*, vol. 31, no. 1, pp. 39–46, 2008.

[28] Z. Tahmasebi and M. Hatami, "Study of the gain saturation effect on the propagation of dark soliton in Er^{3+}-doped, $Ga_5Ge_{20}Sb_{10}S_{65}$ chalcogenide fiber amplifier," *Optics Communications*, vol. 284, no. 2, pp. 656–659, 2011.

[29] Z. G. Lian, Q. Q. Li, D. Furniss, T. M. Benson, and A. B. Seddon, "Solid microstructured chalcogenide glass optical fibers for the near- and mid-infrared spectral regions," *IEEE Photonics Technology Letters*, vol. 21, no. 24, pp. 1804–1806, 2009.

[30] C. Chaudhari, M. Liao, T. Suzuki, and Y. Ohishi, "Chalcogenide core tellurite cladding composite microstructured fiber for nonlinear applications," *Journal of Lightwave Technology*, vol. 30, no. 13, Article ID 6179495, pp. 2069–2076, 2012.

[31] S. D. Jackson and G. Anzueto-Sánchez, "Chalcogenide glass Raman fiber laser," *Applied Physics Letters*, vol. 88, no. 22, Article ID 221106, 2006.

[32] M. C. Pierce, S. D. Jackson, M. R. Dickinson, and T. A. King, "Laser-tissue interaction with a high-power 2 μm fiber laser: preliminary studies with soft tissue," *Lasers in Surgery and Medicine*, vol. 25, no. 5, pp. 407–413, 1999.

[33] M. C. Pierce, S. D. Jackson, M. R. Dickinson, T. A. King, and P. Sloan, "Laser-tissue interaction with a continuous wave 3 μm fibre laser: preliminary studies with soft tissue," *Lasers in Surgery and Medicine*, vol. 26, no. 5, pp. 491–495, 2000.

[34] S. D. Jackson and A. Lauto, "Diode-pumped fiber lasers: a new clinical tool?" *Lasers in Surgery and Medicine*, vol. 30, no. 3, pp. 184–190, 2002.

[35] S. Popov, "Fiber laser overview and medical applications," in *Tunable Laser Applications*, F. J. Duarte, Ed., pp. 197–226, CRC Press, Boca Raton, Fla, USA, 2nd edition, 2009.

[36] F. Prudenzano, L. Mescia, L. Allegretti, V. Moizan, V. Nazabal, and F. Smektala, "Theoretical study of cascade laser in erbium-doped chalcogenide glass fibers," *Optical Materials*, vol. 33, no. 2, pp. 241–245, 2010.

[37] F. Prudenzano, L. Mescia, L. A. Allegretti et al., "Design of Er^{3+}-doped chalcogenide glass laser for MID-IR application," *Journal of Non-Crystalline Solids*, vol. 355, no. 18-21, pp. 1145–1148, 2009.

[38] A. B. Seddon, Z. Tang, D. Furniss, S. Sujecki, and T. M. Benson, "Progress in rare-earth-doped mid-infrared fiber lasers," *Optics Express*, vol. 18, no. 25, pp. 26704–26719, 2010.

[39] R. S. Quimby, L. B. Shaw, J. S. Sanghera, and I. D. Aggarwal, "Modeling of cascade lasing in dy:chalcogenide glass fiber laser with efficient output at 4.5 μm," *IEEE Photonics Technology Letters*, vol. 20, pp. 123–125, 2008.

[40] P. A. Thielen, L. B. Shaw, J. S. Sanghera, and I. D. Aggarwal, "Modeling of a mid-IR chalcogenide fiber Raman laser," *Optics Express*, vol. 11, no. 24, pp. 3248–3253, 2003.

[41] J. Li, Y. Chen, M. Chen et al., "Theoretical analysis and heat dissipation of mid-infrared chalcogenide fiber Raman laser," *Optics Communications*, vol. 284, no. 5, pp. 1278–1283, 2011.

[42] K. H. Tow, Y. Léguillon, P. Besnard et al., "Relative intensity noise and frequency noise of a compact Brillouin laser made of $As_{38}Se_{62}$ suspended-core chalcogenide fiber," *Optics Letters*, vol. 37, no. 7, pp. 1157–1159, 2012.

[43] J. Hu, C. R. Menyuk, L. B. Shaw, J. S. Sanghera, and I. D. Aggarwal, "Computational study of 3–5 μm source created by using supercontinuum generation in As_2S_3 chalcogenide fibers with a pump at 2 μm," *Optics Letters*, vol. 35, no. 17, pp. 2907–2909, 2010.

[44] J. Fatome, B. Kibler, M. El-Amraoui et al., "Mid-infrared extension of supercontinuum in chalcogenide suspended core fibre through soliton gas pumping," *Electronics Letters*, vol. 47, no. 6, pp. 398–400, 2011.

Hindawi Publishing Corporation
International Journal of Optics
Volume 2012, Article ID 808679, 5 pages
doi:10.1155/2012/808679

Research Article

Modeling of Mid-IR Amplifier Based on an Erbium-Doped Chalcogenide Microsphere

P. Bia, A. Di Tommaso, and M. De Sario

Dipartimento di Elettrotecnica ed Elettronica, Politecnico di Bari, Via E. Orabona, 4-70125 Bari, Italy

Correspondence should be addressed to M. De Sario, desario@poliba.it

Received 2 March 2012; Accepted 30 May 2012

Academic Editor: Francesco Prudenzano

An optical amplifier based on a tapered fiber and an Er^{3+}-doped chalcogenide microsphere is designed and optimized. A dedicated 3D numerical model, which exploits the coupled mode theory and the rate equations, is used. The main transitions among the erbium energy levels, the amplified spontaneous emission, and the most important secondary transitions pertaining to the ion-ion interactions have been considered. Both the pump and signal beams are efficiently injected and obtained by a suitable design of the taper angle and the fiber-microsphere gap. Moreover, a good overlapping between the optical signals and the rare-earth-doped region is also obtained. In order to evaluate the amplifier performance in reduced computational time, the doped area is partitioned in sectors. The obtained simulation results highlight that a high-efficiency midinfrared amplification can be obtained by using a quite small microsphere.

1. Introduction

In recent years, the micro- and nanospherical resonators have attracted great interest for their high quality Q-factor, material versatility, manufacturing easiness, and dopant hosting flexibility for active devices. In rare-earth-doped microspheres, Whispering Gallery Modes (WGMs) can strongly enhance the light-matter interaction, because of their very high Q-factor and small mode volume. A number of application fields could exploit the intriguing WGM properties, such as those involving polarization transmission, coupled-resonator-induced transparency, biosensor analysis [1, 2], nonlinear optics, cavity quantum electrodynamics (QED), and quantum information processing [3].

Rare-earth-doped microspheres based on silica, phosphate, tellurite, and ZBLAN glass host materials [3–7] show ultralow lasing thresholds and very narrow emission linewidths. Chalcogenide glass has recently attracted significant interest as a material for the manufacturing of active microsphere resonators. In fact, they exhibit lower modal volumes, higher refractive indices, and high absorption and emission cross-sections [8]. Moreover, these glasses allow realizing efficient mid-IR amplifiers, thanks to their low phonon energy and to their high capability to host rare earth ions.

In this work, the mathematical model of a microsphere amplifier is described. The signal wavelength is $\lambda_s = 2.76\,\mu$m and the pump wavelength is $\lambda_p = 980$ nm. The model appears more complete than those reported in the literature for active [9–11] and passive [12, 13] devices and it improves the previous work [14]. It involves the coupled mode theory and the rate equations and it allows the simulation of a tapered fiber coupled to the rare-earth-doped chalcogenide glass microsphere. The following features are considered: (i) the radiative and nonradiative rates, at both pump and signal wavelengths, (ii) the stimulated emission at the signal wavelength, (iii) the amplified spontaneous emission noise (ASE), (iv) the lifetime of the considered energy levels, and (v) the ion-ion energy transfers. The model is implemented with a homemade 3D numerical code and the numerical results are shown.

The paper is structured as follows: Section 2 includes the mathematical model, Section 3 the numerical results, and finally Section 4 the conclusions.

2. Mathematical Model

A sketch of the considered system is shown in Figure 1. It consists of a microsphere and a tapered fiber both in

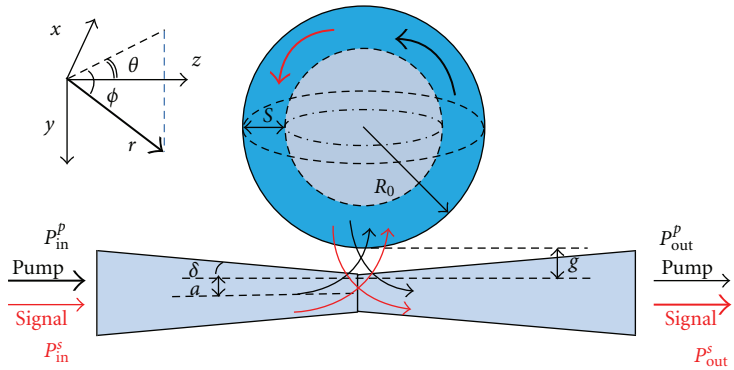

Figure 1: Schematic of a microsphere coupled to a tapered fiber.

$Ga_5Ge_{20}Sb_{10}S_{65}$ chalcogenide glass. P_p^{in} and P_s^{in} stand for the input pump and signal powers, respectively, P_p^{out} and P_s^{out} for the output pump and signal powers, respectively, δ is the angle of the taper, g is the gap between the cavity and the fiber, R_0 is the sphere radius, and a is the waist fiber radius and S is the thickness of doped area.

By assuming that the input signals are narrowband, each one gives rise to a single l, m, n WGM within the microsphere. Moreover, on the assumption that the microsphere is only doped in the outer layer, the most amplified WGM is the fundamental one ($n = 1$).

Figure 2 shows the transitions among the energy levels considered in the developed numerical code. In particular, the population inversion is possible between $^4I_{11/2}$ and $^4I_{13/2}$ energy levels, by pumping at the wavelength $\lambda_p = 980$ nm. As a consequence, the amplification can occur at the signal wavelength $\lambda_s = 2760$ nm. Moreover, the energy transitions due to cross-relaxation and cooperative upconversion effects have also to be considered in the simulations, because of the high dopant concentration and the comparable lifetime of $^4I_{13/2}$, $^4I_{11/2}$, and $^4I_{9/2}$ energy levels. The numerical values of absorption, emission cross-sections, upconversion, and cross-relaxation coefficients as well as the energy level lifetimes are reported in Table 1.

The active behavior is modeled by calculating the coupling coefficients, the quality factor, the mode volume, the transition rates. These parameters are obtained with an accurate evaluation of electromagnetic field mode properties in both fiber and microsphere [15]. The following conditions are considered:

(i) the energy gaps between the Stark levels of each manifold are small when compared to the energy separation between different manifolds;

(ii) the rates between the Stark levels are much faster than those between two different manifolds;

(iii) the population in any manifold is in local thermal equilibrium with the glass lattice.

The following differential equations describe the time-variation of the field amplitude A_s (signal) and A_p (pump) inside the microsphere, considering both the dopant ions and the fiber coupling:

$$\begin{aligned}\frac{dA_s(t)}{dt} &= -\frac{1}{2}\left(\frac{1}{\tau_{ext}^s}+\frac{1}{\tau_0^s}\right)A_s(t)\\ &\quad + j\sqrt{\frac{1}{\tau_{ext}^s T_c^s}}A_s^{in}(t) - j\Delta\omega^s A_s(t) + g_s A_s(t),\\ \frac{dA_p(t)}{dt} &= -\frac{1}{2}\left(\frac{1}{\tau_{ext}^p}+\frac{1}{\tau_0^p}\right)A_p(t)\\ &\quad + j\sqrt{\frac{1}{\tau_{ext}^p T_c^p}}A_p^{in}(t) - j\Delta\omega^p A_p(t) + g_p A_p(t),\end{aligned} \tag{1}$$

where A_s^{in} and A_p^{in} are the field amplitudes at the input end of the optical fiber; being $a = \{s, p\}$, $\Delta\omega^a = \omega_{WGM}^a - \omega_{in}^a$ is the frequency detuning of the fiber input signal from the WGM frequency ω_{WGM}, $T_c^a = 2\pi R_0 n_{eff}^a/c$ is the circulating time inside the microsphere (round trip time), c is the speed of light in vacuum, and n_{eff}^a is the WGM effective refractive index. More precisely, the effective index is almost constant in the resonance bandwidth, because of its narrowness. As a consequence, the modal dispersion can be neglected, and the group index results are almost equal to the effective index. The intrinsic lifetime is $\tau_0 = 1/(\kappa_0^2) = Q_0/\omega_{WGM}$, where Q_0 is the intrinsic quality factor. κ_0 is the intrinsic cavity decay rate, which depends on the total losses due to material

Table 1: Spectroscopic parameters of Er^{3+}-doped $Ga_5Ge_{20}Sb_{10}S_{65}$ chalcogenide glass.

Parameters	Values
σ_{13} at 980 nm	1.32×10^{-24} m^2
σ_{32} at 2760 nm	1.60×10^{-24} m^2
C_{33}	20×10^{-24} m^2 s^{-1}
C_{22}	30×10^{-24} m^2 s^{-1}
C_{41}	5×10^{-24} m^2 s^{-1}
τ_{21}	1.83×10^{-3} s
τ_{32}	1.37×10^{-3} s
τ_{43}	1.08×10^{-3} s
τ_{54}	0.13×10^{-3} s

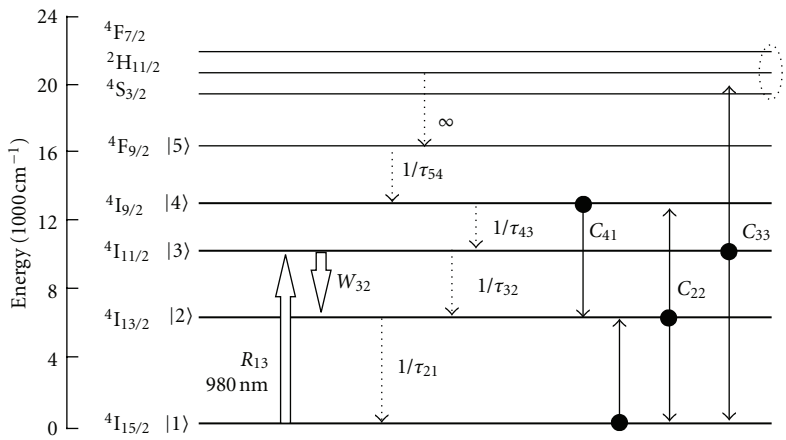

Figure 2: Diagram of energy levels.

absorption, surface scattering losses, radiative losses, and whispering gallery losses. Both the radiative and surface scattering losses can be neglected in the microspheres having the diameter around a few tens of microns and a perfect surface. The coupling lifetime $\tau_{\text{ext}} = 1/\kappa_{\text{ext}}^2 = m\pi/(\omega K^2)$, where κ_{ext} is the cavity decay rate or coupling coefficient, denotes the coupling phenomenon between microsphere and optical fiber. The field overlapping, K, is calculated according to the overlap integral [15]:

$$K = \int_V \frac{k_0^2(n_s^2 - n_0^2)}{2\beta_f} \mathbf{E}_f \cdot \mathbf{E}_s^* dV, \tag{2}$$

where $k_0 = 2\pi/\lambda$; n_s and n_0 are, respectively, the wave vector in the vacuum, the microsphere, and background refractive indices; β_f is the fiber propagation constant; $\mathbf{E}_f$ is the electric field of the fiber fundamental mode; $\mathbf{E}_s$ is the WGM field both normalized on the $\hat{r} \cdot \hat{\theta}$ plane. Moreover, in (1) the gain/attenuation due to the dopant ions, evaluated over a round-trip, is defined as follows:

$$g_a = \frac{c}{2n_{\text{eff}}^a} \Gamma_a \sum_{i=2}^{5} \sum_{j=1}^{i-1} \left(N_i \sigma_{ij} - N_j \sigma_{ji} \right) \quad a = \{s, p\}, \tag{3}$$

where N_i is ion population of the i-th energy level, σ_{ji} is the absorption cross-section, and σ_{ij} is the emission cross-section, Γ_a is the overlap factor of each WGM with the rare-earth-doped region. The N_i values are obtained by using the rate equation model, arising from the energy level diagrams in Figure 2 and reported in [14].

The evolution of both the pump and signal field amplitudes at the fiber output end is given by:

$$A_a^{\text{out}}(t) = \sqrt{1 - \frac{T_c^a}{\tau_{\text{ext}}^a}} A_a^{\text{in}}(t) + j\sqrt{\frac{T_c^a}{\tau_{\text{ext}}^a}} A_a(t) \quad a = \{s, p\}, \tag{4}$$

where A_a is evaluated at the nearest point between the microsphere and the optical fiber ($r = R_0$, $\theta = 0$, $\phi = \pi/2$). Finally, the overall gain (transmittance) of the amplifier, is calculated by using [16]:

$$G = \left| \frac{A_s^{\text{out}}}{A_s^{\text{in}}} \right|^2 = \left| \sqrt{1 - \frac{T_c^s}{\tau_{\text{ext}}^s}} + j\sqrt{\frac{T_c^s}{\tau_{\text{ext}}^s}} \frac{A_s}{A_s^{\text{in}}} \right|^2. \tag{5}$$

3. Numerical Results

The developed numerical code has a low computational cost (reduced computational time and memory) compared with FDTD and FEM-based algorithms. Moreover, it is flexible and it can be easily used to evaluate the amplifier performance in several configurations. In fact, the geometrical parameters (e.g., R_0, δ, a, g), the operational ones (e.g., modulation, frequency, power of the input signals) as well as the physical ones (the rare earth concentration, the thickness of the doped region, and the refractive indices) can be varied. Moreover, the numerical code can be easily extended to the analysis of more complex rare earth and lasing systems.

A number of simulations have been performed to demonstrate the feasibility of 2760 nm signal amplification. In particular, a parametric investigation is carried out to evaluate the amplifier performances. In the simulations, the following parameters are used: input signal power $P_s^{\text{in}} = 10$ nW, input pump power $P_p^{\text{in}} = 100$ mW, thickness of doped region $S = 3\,\mu$m, for which the corresponding overlap factors are $\Gamma_s = 0.89$ for the signal and $\Gamma_p = 0.99$ for the pump.

Figure 3 depicts the signal gain as a function of fiber-microsphere gap g, for three different microsphere radii $R_0 = 20\,\mu$m, $30\,\mu$m and $40\,\mu$m, with the taper angle $\delta = 0.03$ rad, and dopant concentration equal to 0.5% in weight percentage ($N_{\text{tot}} = 5.77 \times 10^{25}$ ions/m^3). It can be observed that the gain increases with the gap until a value beyond which the transmittance drastically decreases. This is caused by the undercoupling condition for the power signal, being low the power coupled to the microsphere. Undercoupling condition occurs for smaller gap by increasing the microsphere radius, since the structure better confines the evanescent wave.

Figure 4 illustrates the signal gain as a function of the taper angle δ, for three different fiber radii $a = 500$ nm,

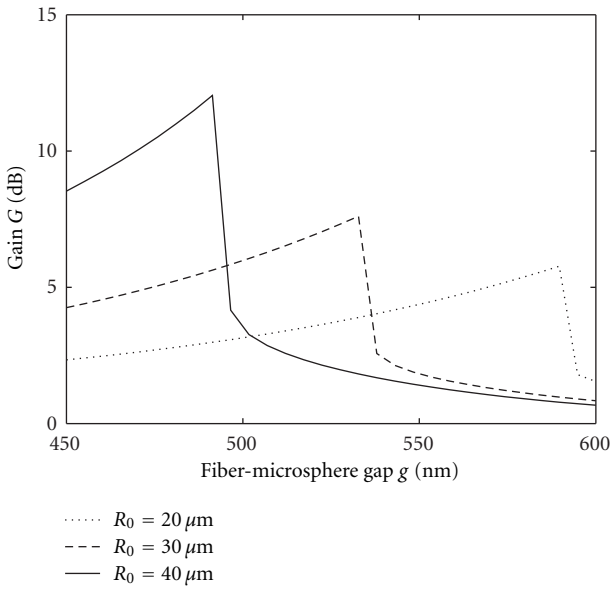

Figure 3: Signal amplification as a function of fiber-microsphere gap g for three different microsphere radii.

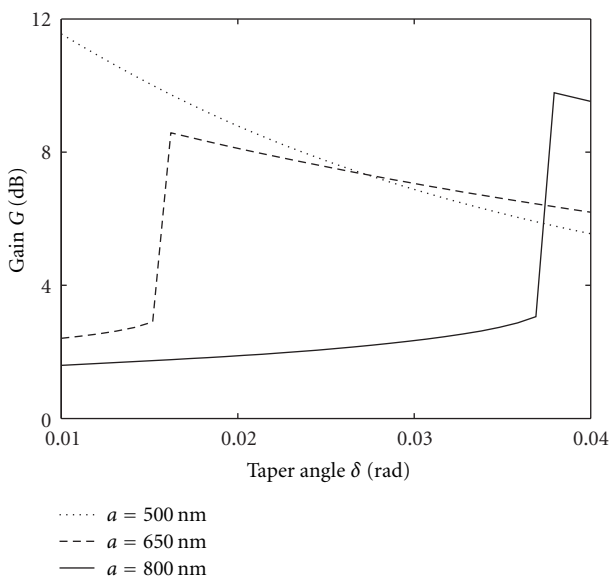

Figure 4: Signal amplification as a function of the taper angle for three different values of the waist fiber radius.

650 nm, and 800 nm. The choice of the range of the taper angle takes into account the structure durability. The geometrical and physical parameters are $R_0 = 30\,\mu$m, $g = 540$ nm, and $N_{\text{tot}} = 5.77\times10^{25}$ ions/m^3. If the fiber radius $a = 500$ nm, the gain increases by decreasing the taper angle and also the decreasing of the coupling factor occurs. Moreover, the amplification occurs for high coupling factor values, corresponding to high taper angle values. In particular, the minimum δ value required for the signal amplification depends on the fiber radius. In fact, by using a small fiber radius, the increasing of the coupling factor occurs due to the

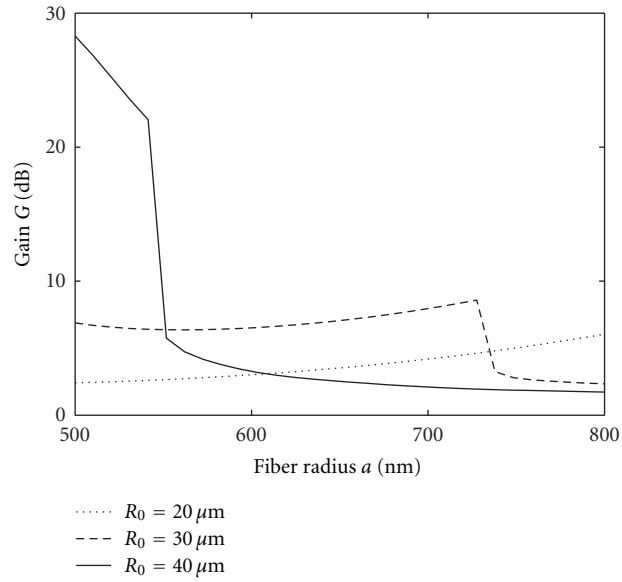

Figure 5: Signal amplification as a function of the taper angle for three different values of the waist fiber radius.

enhancement of the output evanescent wave. In Figure 4, the undercoupling condition is not occurring for the whole δ range, if $a = 500$ nm; whereas the undercoupling condition occurs for $\delta < 0.035$ rad, if $a = 800$ nm.

Figure 5 depicts the signal gain as a function of a fiber radius, for three microsphere radii $R_0 = 20\,\mu$m, $30\,\mu$m, $40\,\mu$m, with taper angle $\delta = 0.03$ rad, and dopant concentration $N_{\text{tot}} = 5.77 \times 10^{25}$ ions/m^3. These fiber radii have been considered because lower values determine a signal leakage due to the low confinement strength at the signal wavelength. Whereas, the greater radii induce a multimodal propagation at the pump wavelength. The maximum gain value occurs for the microsphere radius $R_0 = 40\,\mu$m and fiber radius $a = 500$ nm. Moreover, by increasing the fiber radius, the coupling decreases leading to the undercoupling condition and reducing the amplifier performances.

Figure 6 shows the signal gain as a function of the erbium concentration N_{Er}, for three different microsphere-fiber gaps $g = 500$ mm, 550 mm, 600 mm, with $\delta = 0.03$ rad, $R_0 = 30\,\mu$m, $a = 700$ nm. By increasing the ion concentration, the enhancement of the signal amplification occurs until a threshold value. In fact, if high erbium concentrations are used, the population inversion occurs as long as the available power is sufficient. The threshold value can be suitably increased by enhancing the coupling (e.g., by reducing the gap) or decreased by reducing the coupling (e.g., by increasing the gap). Low gap values induce the cavity power reduction, reaching the value not allowing the doped ion population inversion, thus limiting the amplifier performances.

4. Conclusions

In this paper, an Er^{3+}-doped chalcogenide microsphere amplifier evanescently coupled with a tapered optical fiber

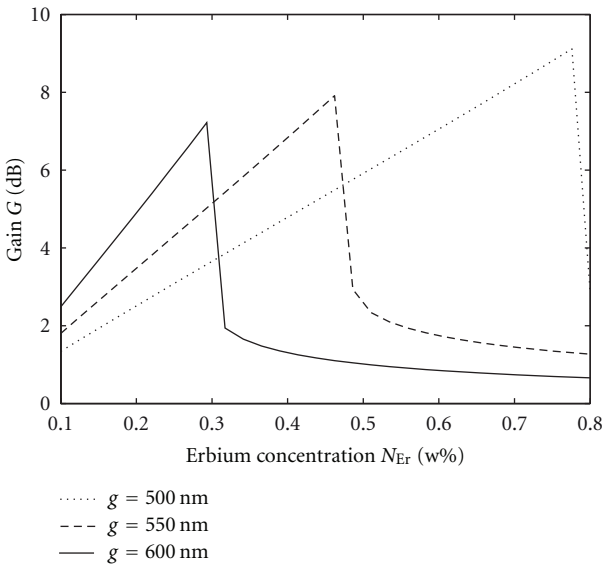

Figure 6: Signal amplification as a function of the erbium concentration for three different values of fiber gap.

has been designed by means of a homemade 3D numerical code. It includes both the rate equation and coupled mode theory models. Spherical coordinates are used to find the solution of the scalar Helmholtz equation needed for the electromagnetic analysis of the microsphere. The homemade numerical code allows to evaluate the amplifier performance by changing several parameters: fiber-microsphere gap, thickness of erbium doped region, fiber taper angle, erbium concentration, and operative parameters such as pump and signal power.

The microsphere resonator shows low threshold power ($\approx$ 80 mW) and high gain ($\approx$ 8 dB) at the signal wavelength $\lambda_s = 2760$ nm. Moreover the total size of the device is few tens of microns. As future developments, slow light phenomenon could be obtained, exploiting the coherent population oscillations in order to realize buffers for optical telecommunications and optical logic gates. In addition, this device could be used to generate low threshold pump powers. Finally, the model can be easily extended to take into account both the mode degeneracy and the multimodal pump and signal, in order to match the simulation dynamics with the realistic device one. As a drawback, a more complete calculation will require more computational time.

References

[1] H. C. Ren, F. Vollmer, S. Arnold, and A. Libchaber, "High-Q microsphere biosensor—analysis for adsorption of rodlike bacteria," *Optics Express*, vol. 15, no. 25, pp. 17410–17423, 2007.

[2] F. Vollmer and S. Arnold, "Whispering-gallery-mode biosensing: label-free detection down to single molecules," *Nature Methods*, vol. 5, no. 7, pp. 591–596, 2008.

[3] L. Yang and K. J. Vahala, "Gain functionalization of silica microresonators," *Optics Letters*, vol. 28, no. 8, pp. 592–594, 2003.

[4] G. S. Murugan, M. N. Zervas, Y. Panitchob, and J. S. Wilkinson, "Integrated Nd-doped borosilicate glass microsphere laser," *Optics Letters*, vol. 36, no. 1, pp. 73–75, 2011.

[5] S. Y. Chen, T. Sun, K. T. V. Grattan, K. Annapurna, and R. Sen, "Characteristics of Er and Er-Yb-Cr doped phosphate microsphere fibre lasers," *Optics Communications*, vol. 282, no. 18, pp. 3765–3769, 2009.

[6] P. Féron, "Whispering gallery mode lasers in erbium doped fluoride glasses," *Annales de la Fondation Louis de Broglie*, vol. 29, no. 1-2, pp. 317–329, 2004.

[7] G. Nunzi Conti, A. Chiasera, L. Ghisa et al., "Spectroscopic and lasing properties of Er^{3+}-doped glass microspheres," *Journal of Non-Crystalline Solids*, vol. 352, no. 23-25, pp. 2360–2363, 2006.

[8] G. R. Elliott, D. W. Hewak, G. S. Murugan, and J. S. Wilkinson, "Chalcogenide glass microspheres; their production, characterization and potential," *Optics Express*, vol. 15, no. 26, pp. 17542–17553, 2007.

[9] L. Mescia, F. Prudenzano, M. De Sario, T. Palmisano, M. Ferrari, and G. C. Righini, "Design of rare-earth-doped microspheres," *IEEE Photonics Technology Letters*, vol. 22, no. 6, pp. 422–424, 2010.

[10] K. Totsuka and M. Tomita, "Optical microsphere amplification system," *Optics Letters*, vol. 32, no. 21, pp. 3197–3199, 2007.

[11] Y. G. Boucher and P. Féron, "Generalized transfer function: a simple model applied to active single-mode microring resonators," *Optics Communications*, vol. 282, no. 19, pp. 3940–3947, 2009.

[12] M. L. Gorodetsky and V. S. Ilchenko, "Optical microsphere resonators: optimal coupling to high-Q whispering-gallery modes," *Journal of the Optical Society of America B*, vol. 16, no. 1, pp. 147–154, 1999.

[13] C. L. Zou, Y. Yang, C. H. Dong et al., "Taper-microsphere coupling with numerical calculation of coupled-mode theory," *Journal of the Optical Society of America B*, vol. 25, no. 11, pp. 1895–1898, 2008.

[14] L. Mescia, P. Bia, M. De Sario, A. Di Tommaso, and F. Prudenzano, "Design of mid-infrared amplifiers based on fiber taper coupling to erbium-dopedmicrospherical resonator," *Optics Express*, vol. 20, no. 7, pp. 7616–7629, 2012.

[15] B. E. Little, J. P. Laine, and H. A. Haus, "Analytic theory of coupling from tapered fibers and half-blocks into microsphere resonators," *Journal of Lightwave Technology*, vol. 17, no. 4, pp. 704–715, 1999.

[16] K. Vahala, *Optical Microcavities*, World Scientific Publishing, Singapore, 2004.

Hindawi Publishing Corporation
International Journal of Optics
Volume 2012, Article ID 130517, 17 pages
doi:10.1155/2012/130517

Research Article

Light Combining for Interferometric Switching

Marco Masi,[1] Mattia Mancinelli,[2] Paolo Bettotti,[2] and Lorenzo Pavesi[2]

[1] *Institut des Nanotechnologies de Lyon, Université de Lyon, INL-UMR5270, CNRS, INSA de Lyon, 69621 Villeurbanne, France*
[2] *Nanoscience Laboratory, Department of Physics, University of Trento, Via Sommarive 14, 38121 Trento, Italy*

Correspondence should be addressed to Marco Masi, marco.masi@gmail.com

Received 4 February 2012; Accepted 11 April 2012

Academic Editor: Francesco Prudenzano

Interferometric switching as a routing method in sequence of coupled optical microresonators is explored. Mach-Zhender interferometry is extended to systems of side-coupled integrated sequences of resonators (SCISSORs) and coupled resonators optical waveguides (CROWs). We generalized Coupled Mode Theory (CMT) to a system of three coupled waveguides. The two bus interferometric switching functions of SCISSOR and CROW resonant structures are investigated. A novel switching device based on three input phase modulation ports is presented. This device displays a wide range of switching behaviors which might lead to new interesting applications.

1. Introduction

The tremendous growth of communication services and information technologies demands new and enhanced networking capabilities. Switching is one of the main functions of communication systems and networks. In particular, novel optical switching technologies have the potential to play a decisive role in future telecommunication and information processing systems. The extensive deployment of wavelength division multiplexing (WDM) technologies demands for high-speed, scalable, and rapidly reconfigurable network switching. Several optical switching technologies exist, like electrooptic (EO), acoustooptic (AO), thermooptic (TO), optomechanical (OM), and optical amplifier (OA) based switching. Refractive index modulation, inducing phase differences for switching functionalities, resorts especially to EO or TO effects. These are widely used in directional couplers, Mach-Zehnder interferometers, and multi-mode interference (MMI) switches (for a good review see, e.g., [1]). The present paper focuses on some possible extensions of these interferometric techniques by means of sequences of microoptical resonator systems, like SCISSORs (side-coupled integrated spaced-sequences of resonators) and CROWs (coupled resonator optical waveguides) [2–6]. A particular combination of these allows to use three input waveguides for amplitude and phase modulation. The advantage of a system of resonators over conventional single-resonator scheme coupling is its larger spectral band, the possibility to operate through interferometry on several channels and its higher design flexibility. In particular, this latter aspect allows for a diversity of behaviors compared to usual directional coupling switching.

The practical realization of such kind of phase switching devices is, however, still limited by present photonic fabrication tolerances. Phase shifting of light requires the same interferometric precision as the device operation itself. For example, the phase difference between two interfering light beams needs to be tightly controlled at the subwavelength level to provide efficient switching. Even more sensitive to small deviations from the nominal parameters are devices where coherent addition of signals is achieved by arranging complex systems of resonator chains. These require nanometer level accuracy in the fabrication of the single resonators and their mutual spacings. For instance, coupled resonator induced transparency (CRIT) effects emerge easily only for few nanometer deviations [7–12]. However, while present optical lithography still suffers of few nanometers imprecision needing further improvements, the next generation optical lithography is likely to achieve an order of magnitude leap in accuracy paving the way to novel interferometric devices [13]. Also, the fabrication of electrooptic silicon-photonic modulators which are capable of providing smooth

and uniform phase shifts over a broad spectrum is a topic of intense research and promises to find a wide area of applications [14]. Elsewhere we have demonstrated the practical realization of a novel silicon photonic interferometric switching device showing that resonator phase switching is indeed feasible [12]. Therefore, it is interesting to explore from the theoretical point of view some extensions of conventional directional coupling methods which could have potential applications in upcoming interferometric devices.

The next section will briefly summarize the basics of coupled mode theory (CMT) which will be particularly useful in our context. Section 2 will set the stage for interferometric switching between three waveguides which in turn will be used in Section 3 where interferometric switching with a dual bus waveguide resonator system is described. Section 4 will extend this to a particular arrangement of three-bus resonator systems.

2. CMT and Phase Switching for the Double-Sided Symmetric Codirectional Coupler

CMT has grown to a vast subject in the last three decades (for a good introduction see e.g., [15]). Let us quickly recall some standard equations which describe in particular the coupling between two waveguides.

We assume that the two waveguides have the same geometry and propagation constants β, and they are homogenous and isotropic. Material or other types of losses are negligible. Within these assumptions, the fields in the first and second waveguide are given by the solution of the following coupled differential equations:

$$\begin{aligned} \frac{\partial A_1(z)}{\partial z} &= icA_2(z), \\ \frac{\partial A_2(z)}{\partial z} &= icA_1(z), \end{aligned} \tag{1}$$

with $A_1(z)$ and $A_2(z)$ are the z dependent parts of the fields, and c a mutual mode coupling coefficient. c is obtained from perturbation theory by the amplitudes cross-sectional integral over the section of the two waveguides of the codirectional coupler and has the dimension of an inverse length. If we impose as initial conditions

$$A_1(0) = A_1 e^{i\phi_1}, \qquad A_2(0) = A_2 e^{i\phi_2}, \tag{2}$$

then the solutions at z are

$$\begin{aligned} A_1(z) &= tA_1 e^{i\phi_1} + i\kappa A_2 e^{i\phi_2}, \\ A_2(z) &= i\kappa A_1 e^{i\phi_1} + tA_2 e^{i\phi_2}, \end{aligned} \tag{3}$$

with

$$\kappa = \sin(cz)e^{i\beta z}, \qquad t = \cos(cz)e^{i\beta z}, \tag{4}$$

being κ and t the cross- and through-coupling coefficients, respectively, and $e^{i\beta z}$ accounts for the phase shift. κ and t are given by

$$\kappa = \sin\left(\frac{\pi L}{2L_c}\right)e^{i\beta L}, \qquad t = \cos\left(\frac{\pi L}{2L_c}\right)e^{i\beta L}, \tag{5}$$

where

$$L_c = \frac{\lambda}{2(n_{\text{effe}}(\lambda) - n_{\text{effo}}(\lambda))} \tag{6}$$

is the coupling length, λ the wavelength, L the length of the coupling section, while n_{effe} and n_{effo} are the even and odd mode wavelength-dependent effective indexes, respectively. Then, from (4) and (5), one obtains

$$c = \frac{\pi}{2L_c}. \tag{7}$$

From (3), it follows that

$$\begin{aligned} |A_1(z)|^2 &= |t|^2|A_1|^2 + |\kappa|^2|A_2|^2 + 2|\kappa||t||A_1||A_2|\sin\Delta\phi, \\ |A_2(z)|^2 &= |\kappa|^2|A_1|^2 + |t|^2|A_2|^2 - 2|\kappa||t||A_1||A_2|\sin\Delta\phi, \end{aligned} \tag{8}$$

with $\Delta\phi = \phi_1 - \phi_2$. For simplicity in (8), the dependence of the coupling coefficients on z is omitted. Power conservation condition for the lossless system follows straightforwardly from (5), or (8), as $|t|^2 + |\kappa|^2 = 1$.

If we set $A_2 = 0$, we obtain the well-known power exchange expressions for the single-sided codirectional coupler made of two equal waveguides

$$\begin{aligned} |A_1(z)|^2 &= \cos^2(cz)|A_1|^2 = |t|^2|A_1|^2, \\ |A_2(z)|^2 &= \sin^2(cz)|A_1|^2 = |\kappa|^2|A_1|^2. \end{aligned} \tag{9}$$

The Mach-Zehnder modulator is obtained when two signals with same amplitude ($A_1 = A_2 = A$) are coupled into the waveguides. In fact, (8) becomes

$$\begin{aligned} |A_1(z)|^2 &= |A|^2(1 + 2|\kappa||t|\sin\Delta\phi), \\ |A_2(z)|^2 &= |A|^2(1 - 2|\kappa||t|\sin\Delta\phi), \end{aligned} \tag{10}$$

which shows that, when $\Delta\phi = 0$, no power exchange between the two waveguides occurs, while, for $\Delta\phi = m(\pi/2)$ (m an integer), the power oscillates between the two waveguides depending on the coupling section length, L. If $cL = \pi/4$ and $\Delta\phi = \pm\pi/2$, then all the power is transferred into one or the other waveguide.

Let us now extend (1) to the situation of Figure 1, where three waveguides couple. We call the central waveguide the Drop waveguide for a reason that will be clear in the following. We consider the case of a Drop signal A_D excited by the fields A_1 and A_2 in the upper and lower waveguides. Then, neglecting the direct coupling between the two outer waveguides, we write a set of three coupled differential equations:

$$\begin{aligned} \frac{\partial A_1(z)}{\partial z} &= icA_D(z), \\ \frac{\partial A_D(z)}{\partial z} &= icA_1(z) + icA_2(z), \\ \frac{\partial A_2(z)}{\partial z} &= icA_D(z). \end{aligned} \tag{11}$$

We impose the initial conditions

$$\begin{aligned} A_1(0) &= A_1 e^{i\phi_1}, \\ A_D(0) &= A_D e^{i\phi_D}, \\ A_2(0) &= A_2 e^{i\phi_2}, \end{aligned} \tag{12}$$

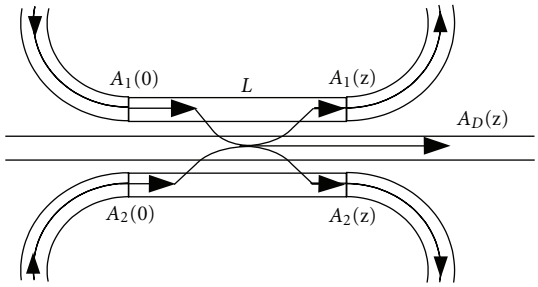

Figure 1: Double sided symmetric codirectional coupler.

where ϕ_1, ϕ_1, and ϕ_D express the phase of A_1, A_2, and A_D, respectively. The solutions of (11) are

$$\begin{aligned} A_1(z) &= t' A_1 e^{i\phi_1} + i\kappa_D A_D e^{i\phi_D} - \kappa' A_2 e^{i\phi_2}, \\ A_D(z) &= i\kappa_D A_1 e^{i\phi_1} + t_D A_D e^{i\phi_D} + i\kappa_D A_2 e^{i\phi_2}, \\ A_2(z) &= -\kappa' A_1 e^{i\phi_1} + i\kappa_D A_D e^{i\phi_D} + t' A_2 e^{i\phi_2}, \end{aligned} \tag{13}$$

with

$$t' = \cos^2\left(\frac{cz}{\sqrt{2}}\right) e^{i\beta z}, \qquad t_D = \cos\left(\sqrt{2}cz\right) e^{i\beta z}, \tag{14}$$

$$\kappa' = \sin^2\left(\frac{cz}{\sqrt{2}}\right) e^{i\beta z}, \qquad \kappa_D = \frac{1}{\sqrt{2}} \sin\left(\sqrt{2}cz\right) e^{i\beta z}. \tag{15}$$

The term $1/\sqrt{2}$ in (15) is a consequence of the symmetry of the system (symmetric coupling and geometry). For simplicity, let us consider $A_D = 0$, then

$$\begin{aligned} |A_1(z)|^2 = {} & |t'|^2 |A_1|^2 + |\kappa'|^2 |A_2|^2 \\ & - 2|\kappa'||t'||A_1||A_2| \cos\Delta\phi, \end{aligned} \tag{16}$$

$$|A_D(z)|^2 = |\kappa_D|^2 \left(|A_1|^2 + |A_2|^2 + 2|A_1||A_2| \cos\Delta\phi\right), \tag{17}$$

$$\begin{aligned} |A_2(z)|^2 = {} & |\kappa'|^2 |A_1|^2 + |t'|^2 |A_2|^2 \\ & - 2|\kappa'||t'||A_1||A_2| \cos\Delta\phi. \end{aligned} \tag{18}$$

If the system is lossless, power conservation implies $|k'|^2 + |k_D|^2 + |t'|^2 = 1$. Despite not being directly coupled to each others, (16) and (18) show a possible crosstalk between the outer waveguides through the intermediate Drop port (crossing of arrows through the Drop port shown in Figure 1). This can be quantified by using as initial condition, for example, $A_2 = 0$ which implies from (16)–(18)

$$\begin{aligned} |A_1(z)|^2 &= |A_1|^2 \cos^4\left(\frac{cz}{\sqrt{2}}\right), \\ |A_D(z)|^2 &= \frac{|A_1|^2}{2} \sin^2\left(\sqrt{2}cz\right), \\ |A_2(z)|^2 &= |A_1|^2 \sin^4\left(\frac{cz}{\sqrt{2}}\right). \end{aligned} \tag{19}$$

Equation (19) is plotted in Figure 2 in normalized intensity and distance. These show that the signal from the upper (lower) waveguide is never completely recovered in the Drop port because part of it recouples towards the lower (upper) waveguide. The Drop behaves like a "power transiting" port, and the amount of light that crosses the structure can be considered as a measure of crosstalk. However, we will see that this interpretation must be taken with caution.

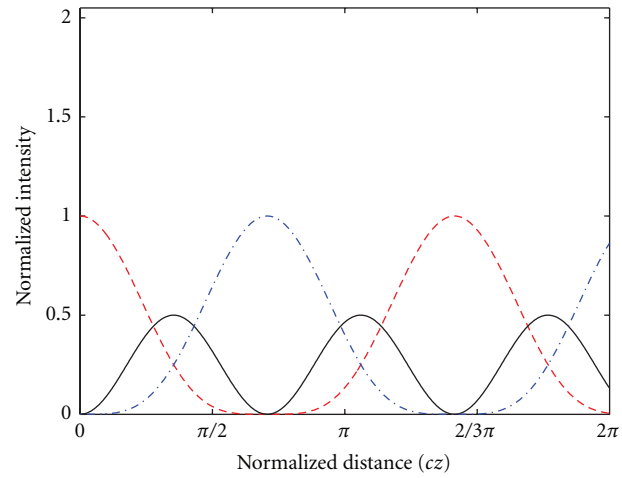

Figure 2: Power transfer in the waveguides of the ds-coupler for one input signal only ((16), (17), and (18), with initial conditions $A_1 = 1$, $A_2 = 0$). Red dashed line: amplitude $A_1(cz)$; blue dotted-dashed line: amplitude $A_2(cz)$; black solid line: amplitude $A_D(cz)$.

In fact, if we consider a same input signal ($A_1 = A_2 = A$) on the top and bottom waveguides, (16)–(18) simplify to

$$\begin{aligned} |A_1(z)|^2 = |A_2(z)|^2 &= |A|^2 \left(1 - \frac{1}{2}\sin^2\left(\sqrt{2}cz\right)(1 + \cos\Delta\phi)\right), \\ |A_D(z)|^2 &= |A|^2 (1 + \cos\Delta\phi) \sin^2\left(\sqrt{2}cz\right). \end{aligned} \tag{20}$$

The case for in phase signals ($\Delta\phi = 0$) is shown in Figure 3(a). In this case, the energy transfer between the Drop and external ports occurs harmonically. A 100% power transfer to the Drop port occurs when

$$L = \frac{\pi}{2\sqrt{2}c} = \frac{L_c}{\sqrt{2}}. \tag{21}$$

Figures 3(b) and 3(c) show this case for a phase difference of $\Delta\phi = \pi/4$ and $\Delta\phi = (3/4)\pi$: the power in the outer waveguides 1 and 2 (magenta dotted-dashed line) oscillates around the initial input value but is never zero, while the Drop signal (black solid line) oscillates according to the propagation length like in the previous case, but with less maximum intensity. If instead a phase difference of $\Delta\phi = \pi$ is applied (Figure 3(d)), there is no power in the Drop port.

Therefore, a particularly interesting situation occurs when a ds-coupler has a coupling section long as in (21) ($cz = (1/\sqrt{2})(\pi/2)$ in Figure 3). In fact, for two equal input signals the ds-coupler acts as an interferometric switch: for $\Delta\phi = 0$, all the power goes into the drop port (Figure 4), while, for $\Delta\phi = \pi$, all the power stays in waveguides 1 and 2 (Figure 5). Under these circumstances, the crosstalk between waveguide 1 and 2 has been suppressed. At first, this seems to be at odds with what shown in Figure 2 where a

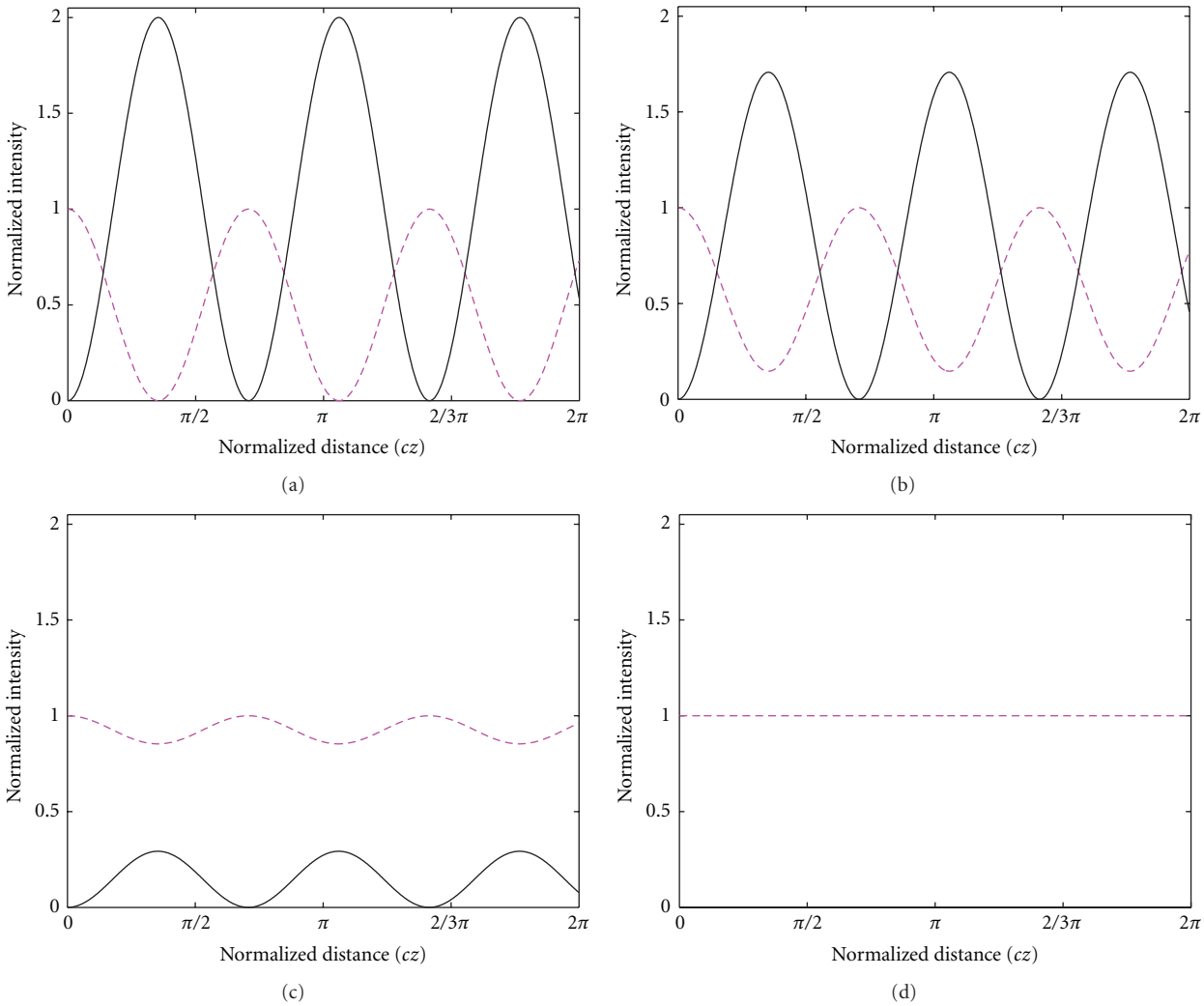

Figure 3: Power transfer in the waveguides of the ds-coupler for two equal input signals ((16), (17), and (18), with initial conditions $A_1 = 1$, $A_2 = 1$, $\Delta\phi = (0, \pi/4, (3/4)\pi, \pi)$ in (a), (b), (c), (d), resp.). Magenta dotted-dashed line: amplitude $A_1(cz)$ and $A_2(cz)$; black solid line: amplitude $A_D(cz)$.

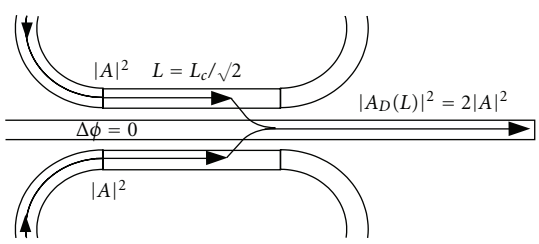

Figure 4: The ds-coupler switch in phase: all the power goes into the Drop port.

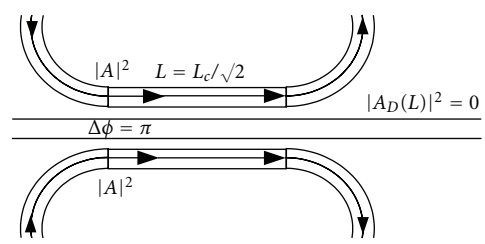

Figure 5: The ds-coupler switch out of phase: no power couples into the Drop port.

significant power transfer from waveguide 1 to waveguide 2 is observed. This apparent contradiction is explained by the fact that the signal in waveguide 1 (waveguide 2) undergoes twice a phase change of $\pi/2$ (evanescent waves have always a $\pi/2$ phase difference with respect to the waveguide core field phase) and the net π dephased cross coupled wave interferes destructively in waveguide 2 (waveguide 1). This interference effect leads to a mutual subtraction of the cross-coupled powers.

For completeness, we mention also the case when the light is injected only in the Drop waveguide, that is,

$$A_1(0) = 0, \qquad A_D(0) = A_D, \qquad A_2(0) = 0, \tag{22}$$

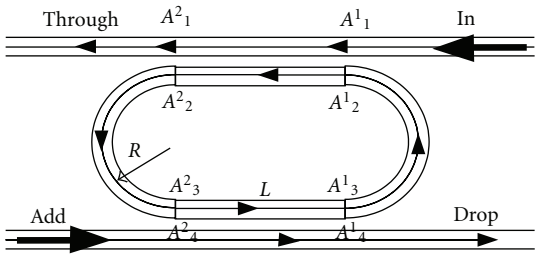

FIGURE 6: The single racetrack switch.

then

$$A_1(z) = A_2(z) = \frac{iA_D \sin(\sqrt{2}cz)}{\sqrt{2}} e^{i\beta z},$$
$$A_D(z) = A_D \cos\left(\sqrt{2}cz\right) e^{i\beta z}, \tag{23}$$

whereby of course

$$|A_1(z)|^2 = |A_2(z)|^2 = \frac{|A_D|^2}{2}\sin^2\left(\sqrt{2}cz\right) = |A_D|^2 \frac{|\kappa_D|^2}{2},$$
$$|A_D(z)|^2 = |A_D|^2 \cos^2\left(\sqrt{2}cz\right) = |A_D|^2 |t_D|^2. \tag{24}$$

These show that the power is equally distributed among the outer waveguides. Note that by imposing a coupling section length equal to the value given by (21), it leads to a complete power transfer into waveguide 1 and 2, that is, the ds-coupler can be used as a splitter. Its advantage over other splitting devices, as Y-branches or MMI splitters, is that it is less sensitive to imbalances, provided that the spacing difference between the waveguides arising due to fabrication imperfections is negligible. Its disadvantage is obviously that it is wavelength dependent.

3. Dual Bus Resonator Interferometric Switch

A further extension of the formalism is to consider a single resonator as in Figure 6. We consider a racetrack resonator so that we can apply the CMT extension developed in Section 2. For simplicity, the bus-waveguide gaps and the coupling section lengths are the same everywhere. To apply the transfer matrix approach [16–21], a first step is to relate the amplitudes (A_1^1, A_2^1) with (A_1^2, A_2^2) (see Figure 6 for the definitions). From (3), we have:

$$\begin{pmatrix} A_1^2 \\ A_2^2 \end{pmatrix} = \mathbf{M}\begin{pmatrix} A_1^1 \\ A_2^1 \end{pmatrix} = \begin{pmatrix} t & i\kappa \\ i\kappa & t \end{pmatrix}\begin{pmatrix} A_1^1 \\ A_2^1 \end{pmatrix}. \tag{25}$$

In order to "transfer" the signal, it is more appropriate to write the relationships $(A_1^1, A_1^2) \rightarrow (A_2^1, A_2^2)$. For which one obtains the coupling matrix $\mathbf{K}$:

$$\begin{pmatrix} A_2^1 \\ A_2^2 \end{pmatrix} = \mathbf{K}\begin{pmatrix} A_1^1 \\ A_1^2 \end{pmatrix} = \frac{1}{i|k|}\begin{pmatrix} -|t| & e^{-i\beta L} \\ -e^{i\beta L} & |t| \end{pmatrix}\begin{pmatrix} A_1^1 \\ A_1^2 \end{pmatrix}, \tag{26}$$

where, for the straight sections, the lossless case $(|\kappa_1|^2 + |t_1|^2 = 1)$ was considered. We instead assume bending losses

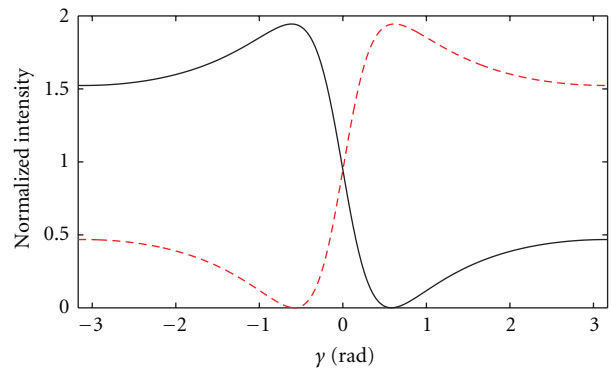

FIGURE 7: The dual-bus single resonator Fano resonance spectrum for $\Delta\phi = \pi/2$ (Drop: black solid line, Through: red dashed line).

in the racetrack. The (forward and backward) internal propagation matrix $\mathbf{P}$ is

$$\begin{pmatrix} A_3^2 \\ A_3^1 \end{pmatrix} = \mathbf{P}\begin{pmatrix} A_2^1 \\ A_2^2 \end{pmatrix} = \begin{pmatrix} 0 & ae^{i\beta\pi R} \\ \frac{1}{a}e^{-i\beta\pi R} & 0 \end{pmatrix}\begin{pmatrix} A_2^1 \\ A_2^2 \end{pmatrix}, \tag{27}$$

where $a = e^{-\alpha\pi R}$ is the half round trip loss factor, α the total loss per unit length, and R the curvature radius.

Equations (26) and (27) define a transfer matrix $\mathbf{T^{PK}}$ as

$$\begin{pmatrix} A_3^2 \\ A_3^1 \end{pmatrix} = \mathbf{T^{PK}}\begin{pmatrix} A_1^1 \\ A_1^2 \end{pmatrix} = \mathbf{PK}\begin{pmatrix} A_1^1 \\ A_1^2 \end{pmatrix}. \tag{28}$$

With the definition of the Input, Through, Drop, and Add ports as in Figure 6, we define A_{In}, A_{Th}, A_D, and A_{Ad} the respective field amplitudes. Therefore,

$$\begin{pmatrix} A_{\mathrm{Ad}} \\ A_D \end{pmatrix} = \mathbf{T^1}\begin{pmatrix} A_{\mathrm{In}} \\ A_{\mathrm{Th}} \end{pmatrix} = \mathbf{KT^{PK}}\begin{pmatrix} A_{\mathrm{In}} \\ A_{\mathrm{Th}} \end{pmatrix}. \tag{29}$$

By rearranging the elements of the transfer matrix $\mathbf{T^1}$ into the scattering matrix $\mathbf{S^1}$, one obtains

$$\begin{pmatrix} A_{\mathrm{Th}} \\ A_D \end{pmatrix} = \mathbf{S^1}\begin{pmatrix} A_{\mathrm{In}} \\ A_{\mathrm{Ad}} \end{pmatrix}. \tag{30}$$

To simulate the device of Figure 6, we use the following parameters: bent curvature radius of 3.25 μm, gap spacing of 0.2 μm, silicon waveguides width of 0.45 μm, silicon waveguide core height of 0.22 μm, SiO_2 cladding of 0.75 μm, and −0.03 dB/90° bent loss in TE polarization [22].

The first interesting situation is when we inject two input signals, one in the Input port and the other in the Add port such that $A_{\mathrm{In}} = e^{i\phi_1}$ and $A_{\mathrm{Ad}} = e^{i\phi_2}$, with ϕ_1 and ϕ_2 their phases. For $\Delta\phi = \phi_2 - \phi_1 = \pi/2$, we obtain Figure 7. The parameter γ represents the round-trip dephasing of the resonator given as $\gamma = 2\pi p_{\mathrm{opt}}(\Delta\lambda/\lambda^2)$, where $p_{\mathrm{opt}} = (2\pi R + 2L)\, n_{\mathrm{eff}}$ is the optical path of the resonator, $\Delta\lambda$ the wavelength shift from a racetrack resonance, and n_{eff} the effective index (at resonance wavelength) of the waveguides (see Appendix A).

The γ dependencies of the Drop and Through signals are asymmetric. This is the manifestation of the Fano resonance

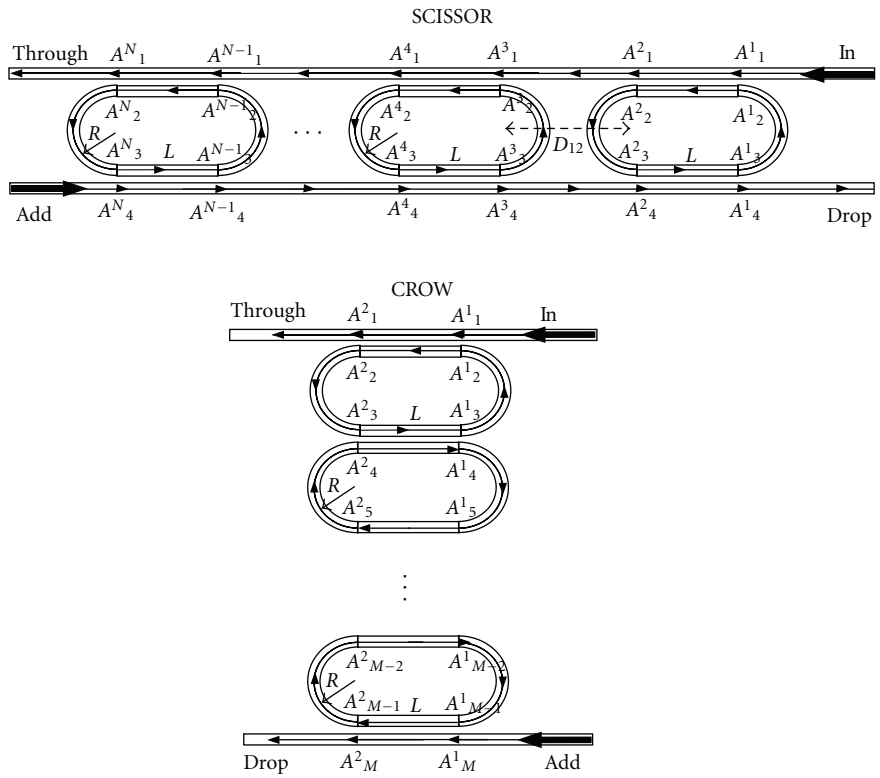

Figure 8: The SCISSOR and CROW resonant structures.

that arises from the interference between the resonant modes in the racetrack, where a narrow band superimposes on the waveguide flat spectral background [23, 24].

Devices where two phase modulated incoming signals are injected can be used for light switching functions. In this case, a high extinction ratio is obtained. For instance, at $\gamma = \pm 0.6$, in Figure 7, the drop and through signals have a maximum or vanish (the maximum intensity does not reach 2 because bent losses are considered). Now, if $\Delta\phi$ is changed from $\pi/2$, as in Figure 7, to $3/2\pi$, a similar spectrum is found with the two signals changed (the black solid line would go into the red dashed line). This means that, by phase modulation, the signal output can be switched in the Through port or in the Drop port.

It is possible to extend this interferometric switching functions to a parallel or serial chain of coupled resonators, that is, in CROW or SCISSOR, Figure 8.

To model a SCISSOR, we introduce an external propagation matrix $\mathbf{Q}^j$ connecting the jth to the $(j+1)$th resonator

$$\begin{pmatrix} A_1^{j+1} \\ A_4^{j+1} \end{pmatrix} = \mathbf{Q}^j \begin{pmatrix} A_1^{j} \\ A_4^{j} \end{pmatrix} = \begin{pmatrix} e^{i\beta D^{jj+1}} & 0 \\ 0 & e^{-i\beta D^{jj+1}} \end{pmatrix} \begin{pmatrix} A_1^{j} \\ A_4^{j} \end{pmatrix}, \quad (31)$$

where D^{jj+1} is the distance which separates the jth to $(j+1)$th resonator. Then, (30) can be generalized to the SCISSOR structure with a scattering matrix $\mathbf{S_h}$:

$$\begin{pmatrix} A_{\mathrm{Th}} \\ A_D \end{pmatrix} = \mathbf{S_h} \begin{pmatrix} A_{\mathrm{In}} \\ A_{\mathrm{Ad}} \end{pmatrix} = \mathbf{S}^N \mathbf{Q}^{N-1} \mathbf{S}^{N-1} \cdots \mathbf{Q}^1 \mathbf{S}^1 \begin{pmatrix} A_{\mathrm{In}} \\ A_{\mathrm{Ad}} \end{pmatrix}. \quad (32)$$

For the CROW, we simply generalize (29) to

$$\begin{pmatrix} A_{\mathrm{Ad}} \\ A_D \end{pmatrix} = \mathbf{T}^N \cdots \mathbf{T}^2 \mathbf{T}^1 \begin{pmatrix} A_{\mathrm{In}} \\ A_{\mathrm{Th}} \end{pmatrix}, \quad (33)$$

where $\mathbf{T}^k$ $(k = 1, \ldots, N)$ is the transfer matrix for the kth resonator and is given by (28). From this we obtain, the scattering matrix $\mathbf{S_v}$

$$\begin{pmatrix} A_{\mathrm{Th}} \\ A_D \end{pmatrix} = \mathbf{S_v} \begin{pmatrix} A_{\mathrm{In}} \\ A_{\mathrm{Ad}} \end{pmatrix}. \quad (34)$$

Figure 9 shows a spectrum of a SCISSOR made of a chain of eight racetrack resonators. Figure 9(a) represents the spectrum when only one signal is injected: high-order filter flat-box spectrum appears. When a second signal is injected at the Add port with the same amplitude but with a phase difference $\Delta\phi = \pi/2$ with respect to the signal injected in the In port, Figure 9(b) is obtained. We call this situation, where we have two input signals, the double bus situation. The point $\gamma = \pm 1.5$ can be used to switch the signal from the Through to the Drop port by controlling the phase at the Add signal. Moving the Add signal phase from $\pi/2$ to $3/2\pi$ switches the output from the Through to the Drop port. Possibly, a wavelength band can be switched by using the $\gamma = \pm 1.75$ point, though with low extinction rates. Therefore, with this respect, the SCISSOR geometry presents limited advantages over the single resonator case of Figure 7.

An eight racetrack CROW structure has a behavior shown in Figure 10. As in the previous case, the left and right

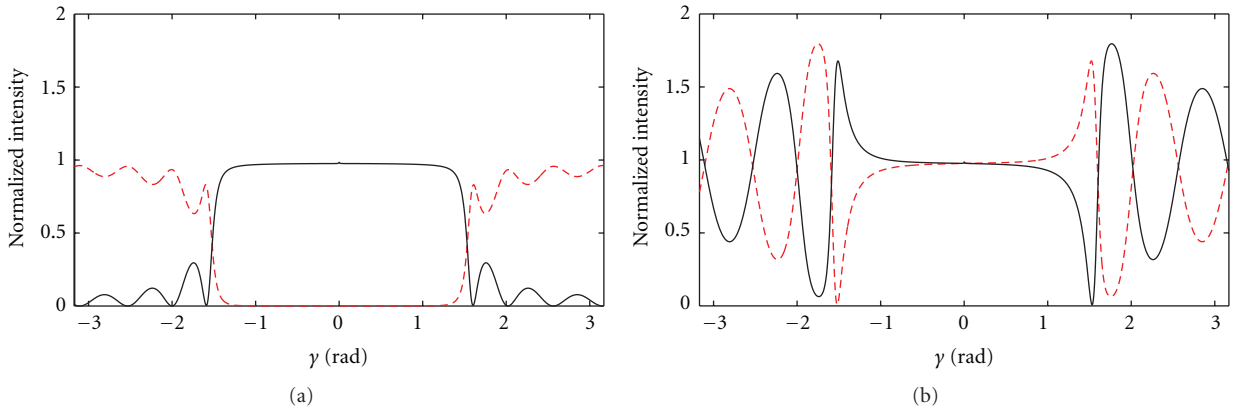

Figure 9: The single (a) and dual-bus (b) eight resonator SCISSOR spectrum for $\Delta\phi = \pi/2$. (Drop: black solid line, Through: red dashed line).

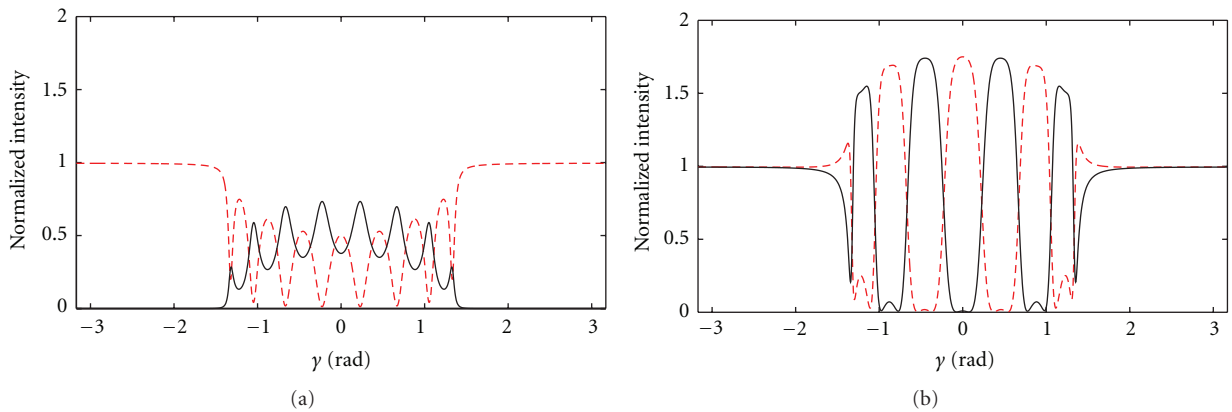

Figure 10: The single (a) and dual-bus (b) eight resonator CROW spectrum for $\Delta\phi = \pi/2$. (Lines as in Figure 9).

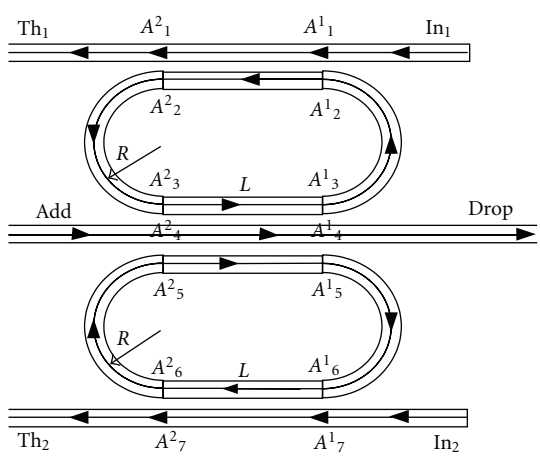

Figure 11: The resonator pair ds-coupler switch.

graphs represent the single- and double-bus spectra for the same dephasing. CROW are very different from SCISSOR: given a N resonator CROW, the single bus device has N Drop resonances (Figure 10(a)) while the double bus device has $N - 1$ bands when a $\Delta\phi = \pi/2$ is considered (Figure 10(b)). Also, in this case, for a dephasing of $\Delta\phi = (3/2)\pi$, one can flip the Through $\leftrightarrow$ Drop port outputs. Not all bands have the same extinction efficiency, only the central ones exhibit an almost ideal on-off. The CROW has the advantage with respect to the SCISSOR and single resonator that it allows band routing or it can be used as an optical interleaver, that is, as a device that separates a set of channels into two sets, routing them separately towards the Drop and Through ports. The width of each band depends on the structural parameters.

4. Three-Bus Resonator Interferometric Switch

A further interesting situation is to model a structure like that of Figure 11. It shows a single pair of racetrack resonators coupled to three-bus waveguides. This interferometric switch works as follows: the input signals In_1 and In_2 are tuned to a resonance wavelength and have the same amplitude. Then, depending on their relative phase, they interfere constructively or destructively in the Drop waveguide. In the former case, the signal is expected to couple into the Drop port, while, in the latter case, the signal is transmitted to the Through ports. Experiments demonstrate this principle [11, 12].

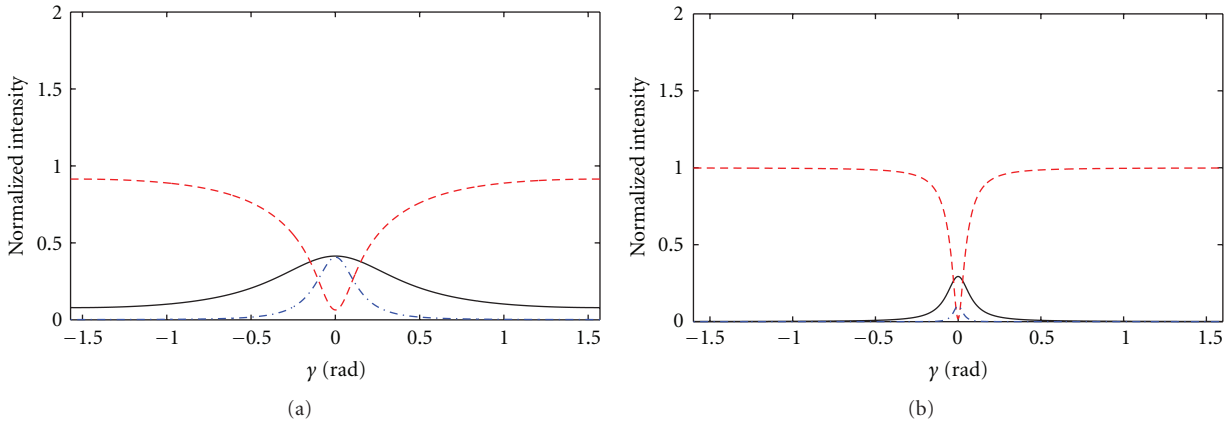

FIGURE 12: Spectral response of the device in Figure 11, with $A_{\mathrm{In}_1} = 1$, $A_{\mathrm{Ad}} = 0$, $A_{\mathrm{In}_2} = 0$, $L = 10\,\mu$m (a), and $L = 3\,\mu$m (b) (Drop port: black solid line, Through1 port: red dashed line, Through2 port: blue dotted-dashed line).

In this section, we model the device as a three-bus device, that is, we drive it with three input signals whose phase is independently controlled. To relate the known signals $A_1^1 = A_{\mathrm{In}_1}$, $A_4^2 = A_{\mathrm{Ad}}$, $A_7^1 = A_{\mathrm{In}_2}$ to the unknown $A_1^2 = A_{\mathrm{Th}_1}$, $A_4^1 = A_D$, and $A_7^2 = A_{\mathrm{Th}_2}$ (Figure 11), we use a general transfer matrix $\mathbf{T}$:

$$\begin{pmatrix} A_{\mathrm{Th}_1} \\ A_D \\ A_{\mathrm{Th}_2} \end{pmatrix} = \begin{pmatrix} T_{11} & T_{21} & T_{31} \\ T_{21} & T_{22} & T_{21} \\ T_{31} & T_{21} & T_{11} \end{pmatrix} \begin{pmatrix} A_{\mathrm{In}_1} \\ A_{\mathrm{Ad}} \\ A_{\mathrm{In}_2} \end{pmatrix} = \mathbf{T} \begin{pmatrix} A_{\mathrm{In}_1} \\ A_{\mathrm{Ad}} \\ A_{\mathrm{In}_2} \end{pmatrix}, \tag{35}$$

whose elements are reported in Appendix B. The device (and therefore $\mathbf{T}$) is symmetric: the paths $\mathrm{In}_1 \to \mathrm{Through}_1$, $\mathrm{In}_1 \to \mathrm{Drop}$, $\mathrm{In}_1 \to \mathrm{Through}_2$ are equivalent to the paths $\mathrm{In}_2 \to \mathrm{Through}_2$, $\mathrm{In}_2 \to \mathrm{Drop}$, $\mathrm{In}_2 \to \mathrm{Through}_1$.

Figure 12 shows the spectral response of the device when used in single bus configuration, that is, only one input signal is injected ($A_{\mathrm{In}_1} = 1$, $A_{\mathrm{Ad}} = 0$, $A_{\mathrm{In}_2} = 0$), for two coupling section lengths of $L = 10\,\mu$m and $L = 3\,\mu$m. The drop signal (black line) shows a typical resonant behavior with a sharper feature for the $L = 3\,\mu$m device than for the $L = 10\,\mu$m device because of its lower coupling efficiency. It is also interesting to note that the crosstalk is much higher for $L = 10\,\mu$m than for $3\,\mu$m. At resonance, the power is almost equally distributed between the Drop and $\mathrm{Through}_2$ ports.

Figure 13 shows the case of a device operated in a duals bus configuration. We used $L = 10\,\mu$m for the coupling section. The input signals have the same amplitude and a phase difference of $\Delta\phi = 0, \pi/4, 3/4\pi, \pi$ for Figures 13(a), 13(b), 13(c), 13(d), respectively. When the two input signals are in phase, and the wavelength is resonant with the two racetracks, then most of the power is transferred to the Drop port. This situation was experimentally confirmed in [11, 12].

The Through ports will not exhibit complete extinction due to crosstalk effects (Figure 13(a)). Similarly, when the two input signals are in antiphase (Figure 13(d)), a complete destructive interference is achieved in the Drop waveguide and no Drop signal is observed. Most of the power goes straight in the Through ports. Note that the minima at resonance in the Through signals are due to the resonator round trip losses. With no dephasing, the Through signal minima coincide, with the Drop signal maximum at resonance λ_0 (Figure 13(a)). In the other case, the Through signals show the behaviors of a Fano resonance (Figures 13(b) and 13(c)). When there is a phase shift between the input signals, the Through signals show characteristics of Fano resonance with a different minimum at $\lambda_F = \lambda_0 \pm 0.8$ nm. This occurs already for a small $\Delta\phi = \pi/10$. Moreover, the Through signal resonance depth depends on the phase shift and vanishes almost completely at $\Delta\phi = \pi/4$ (Figure 13(b)). This is potentially useful to build interferometric switching devices with good on-off extinctions.

To highlight the phase shift dependence, we repeated the calculations at the resonant or at the Fano wavelengths (λ_0 or λ_F, resp.) by varying $\Delta\phi$. At the same time, we varied the intensity of the input signals. The results are shown in Figure 14 for λ_0 and in Figure 15 for λ_F, for $|A_{\mathrm{In}_2}|^2 = \delta \times |A_{\mathrm{In}_1}|^2$ with $\delta = (1, 0.75, 0.25, 0)$. Several features can be observed. First, for perfect input balance (Figure 14(a) and Figure 15(a)), the Drop signal goes to zero at $\Delta\phi = \pi$, while the Through signals vanish only for λ_F and not for λ_0. For this reason, interferometric switching is at λ_F than at λ_0. Second, for λ_F (Figure 15), the three output signals (Drop, $\mathrm{Through}_1$ and $\mathrm{Through}_2$) vanish for three different values of $\Delta\phi$: $\Delta\phi = \pi/4$ the $\mathrm{Through}_2$, $\Delta\phi = \pi$ the Drop, and $\Delta\phi = 7/4\pi$ the $\mathrm{Through}_1$. Third, the transmission of the input signals to the through ports is more effective for λ_F than for λ_0, which might be useful for practical purposes. Fourth, from Figures 14 and 15, it is clear that an interferometric switch device must be robust against input signal imbalance.

Similar features are obtained for a device with $L = 3\,\mu$m. The main difference is that λ_F is more near to λ_0 which makes difficult the use of the Fano concepts for interferometric routing.

A further extension of the ds-router concept is a double SCISSOR structure as shown in Figure 16. To model it, we transform $\mathbf{T}$ (35) into the "scattering matrix" $\mathbf{S}$ such that

$$\begin{pmatrix} A_{\mathrm{Th}_1} \\ A_{\mathrm{Ad}} \\ A_{\mathrm{Th}_2} \end{pmatrix} = \mathbf{S} \begin{pmatrix} A_{\mathrm{In}_1} \\ A_D \\ A_{\mathrm{In}_2} \end{pmatrix}. \tag{36}$$

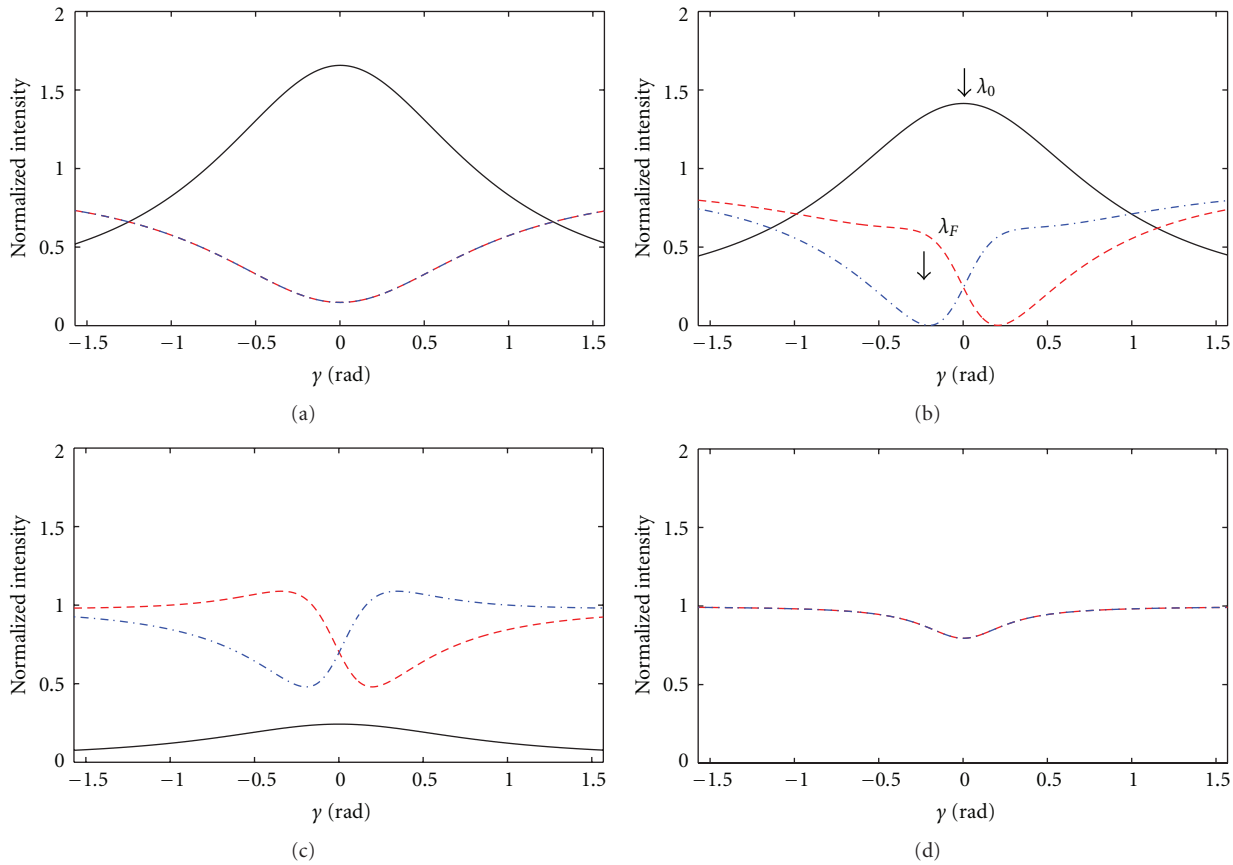

FIGURE 13: Spectral response of the device in Figure 11, with $A_{\mathrm{In}_1} = (1, e^{i(\pi/4)}, e^{i(3/4)\pi}, e^{i\pi})$ ((a), (b), (c), (d), resp.), $A_{\mathrm{Ad}} = 0$, $A_{\mathrm{In}_2} = 1$. (Lines as in Figure 12.)

After simple algebraic manipulation, one finds

$$\mathbf{S} = \frac{1}{T_{22}} \begin{pmatrix} T_{11}T_{22} - T_{12}T_{21} & T_{12} & T_{31}T_{22} - T_{12}T_{21} \\ -T_{21} & 1 & -T_{21} \\ T_{31}T_{22} - T_{12}T_{21} & T_{12} & T_{11}T_{22} - T_{12}T_{21} \end{pmatrix}, \quad (37)$$

where the lower indexes indicate the row $\times$ column element of $\mathbf{T}$.

Then, by introducing an external propagation matrix $\mathbf{Q}^k$ which connects the Through and Add ports of the kth pair of resonators with the In and Drop ports of the $(k+1)$th pair as

$$\begin{pmatrix} A_{\mathrm{In}_1^{k+1}} \\ A_{D^{k+1}} \\ A_{\mathrm{In}_2^{k+1}} \end{pmatrix} = \mathbf{Q}^{\mathbf{k}} \begin{pmatrix} A_{\mathrm{Th}_1^k} \\ A_{\mathrm{Ad}^k} \\ A_{\mathrm{Th}_2^k} \end{pmatrix} = \begin{pmatrix} e^{i\beta D^k} & 0 & 0 \\ 0 & e^{-i\beta D^k} & 0 \\ 0 & 0 & e^{i\beta D^k} \end{pmatrix} \begin{pmatrix} A_{\mathrm{Th}_1^k} \\ A_{\mathrm{Ad}^k} \\ A_{\mathrm{Th}_2^k} \end{pmatrix} \quad (k = 1, \ldots, N), \quad (38)$$

we can express the general equations for the device of Figure 16 with a total transfer matrix $\mathbf{S}_{\mathrm{Tot}}$:

$$\begin{pmatrix} A_{\mathrm{Th}_1^N} \\ A_{\mathrm{Ad}^N} \\ A_{\mathrm{Th}_2^N} \end{pmatrix} = \mathbf{S}_{\mathrm{Tot}} \begin{pmatrix} A_{\mathrm{In}_1^1} \\ A_{D^1} \\ A_{\mathrm{In}_2^1} \end{pmatrix} = \mathbf{S}^N \mathbf{Q}^{N-1} \mathbf{S}^{N-1} \cdots \mathbf{Q}^1 \mathbf{S}^1 \begin{pmatrix} A_{\mathrm{In}_1^1} \\ A_{D^1} \\ A_{\mathrm{In}_2^1} \end{pmatrix}. \quad (39)$$

And, finally, after inverting $\mathbf{S}_{\mathrm{Tot}}$ (37), we get

$$\begin{pmatrix} A_{\mathrm{Th}_1^N} \\ A_{D^1} \\ A_{\mathrm{Th}_2^N} \end{pmatrix} = \mathbf{T}_{\mathrm{Tot}} \begin{pmatrix} A_{\mathrm{In}_1^1} \\ A_{\mathrm{Ad}^N} \\ A_{\mathrm{In}_2^1} \end{pmatrix}, \quad (40)$$

which is the generalized version of (35).

Figure 17 shows the spectral response for the 1,2,4, and 8 pair SCISSOR interferometric switch (Figures 17(a), 17(b), 17(c), 17(d), resp.) with only one input signal. The $(N-1)$ central dips are *not* due to fabrication imperfections [11, 12] but are intrinsic features due to the existence of the central Drop waveguide between the two resonator chains. The system behaves like a single SCISSOR row with asymmetric gaps which introduce a correspondent asymmetric phase shift at each resonator gap leading to CRIT-like features. It is in this spectral region, near the center of the resonance band, where light couples more efficiently into the resonators and travels repeatedly through them producing slow light effects. For this reason, it is also in this central CRIT-like region where most of the attenuation occurs due to radiation and roughness losses on the resonator bent. Note how, aside from the flat-box spectrum, despite strong input imbalance, the two Through ports response (red dashed and blue dotted-dashed lines) tend to merge together inside the mode's spectral range with increasing the number of

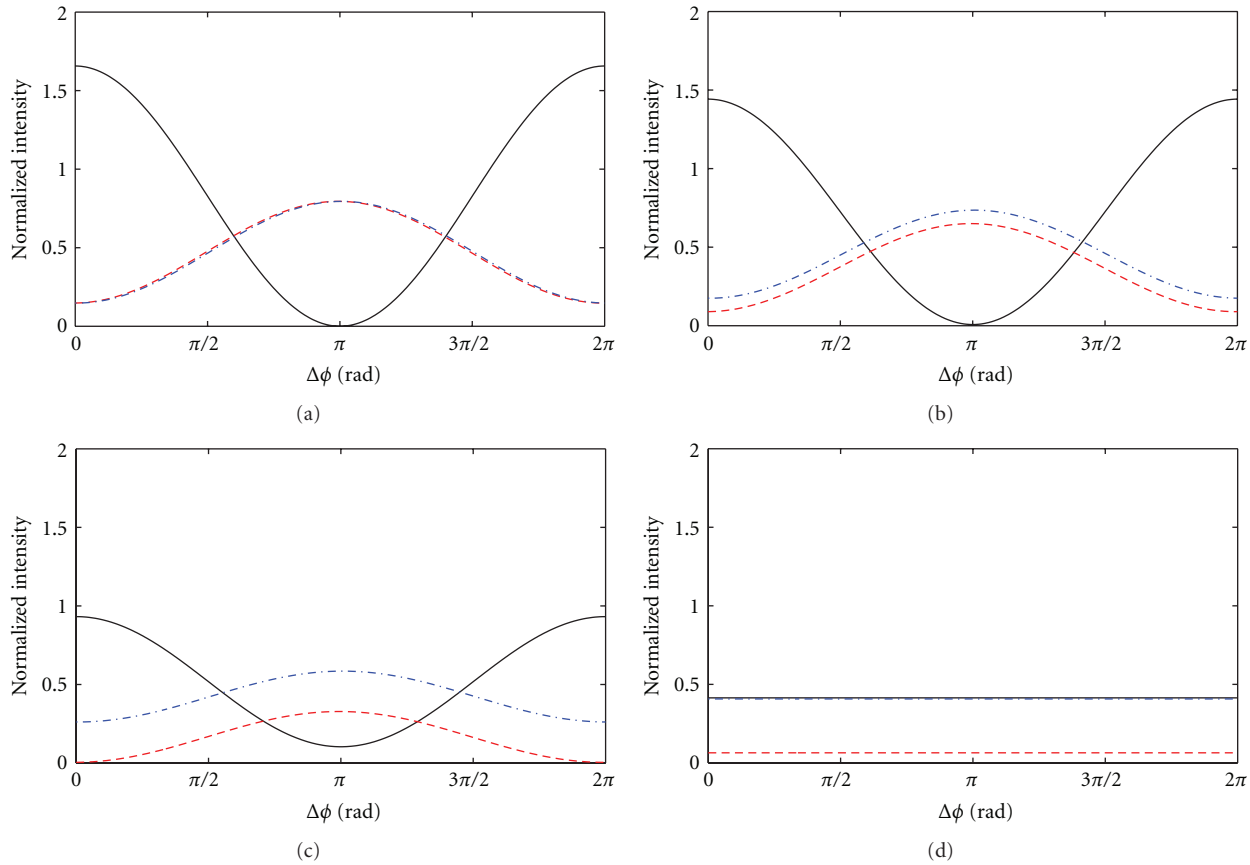

Figure 14: Phase response of the device in Figure 11 at λ_0, with $A_{\mathrm{In}_1} = e^{i\Delta\Phi}$, $A_{\mathrm{Ad}} = 0$, $|A_{\mathrm{In}_2}|^2 = (1,\ 0.75,\ 0.25,\ 0)$ ((a), (b), (c), (d), resp.) (Lines as in Figure 12.)

resonator pairs. This is because in an N-pair SCISSOR the input signals couple to the various resonator pairs, and, while they are propagating along the sequence, their power is progressively balanced due to the large crosstalk. This robustness of SCISSOR devices against input imbalances could have practical advantages where a power injection is uncertain or difficult to tailor.

Figure 18 illustrates the use of a dual bus SCISSOR interferometric switch with two equal input signals. Increasing the number of resonator, the response gets a flat-box shape and a good rejection of the input signal at the two Through ports is obtained.

Figure 19 shows the effect of a phase shift between the two input signals. As $\Delta\phi$ increases, the Drop signal decreases and vanishes for $\Delta\phi = \pi$. The Through signals are coincident within the stop-band and differ outside this wavelength region when $\Delta\phi \neq 0$.

We studied also the effect of an imbalance between the two input signals. A phase sweep at $\gamma = 1$ for four different intensities is shown in Figure 20. Contrary to the single pair interferometric switch affected by Fano resonance asymmetries and unequal Through port signal intensities along the phase sweep, the 2×8 SCISSOR interferometric switch flattens out the differences on the Through signals and shows its robustness against imbalances.

5. Three-Bus Interferometric Switch with Three Input Signals

Another potentially interesting application is to operate the ds-coupler interferometric switch of Figure 11 with three input signals, that is, to use the Add port as a third input port. Figure 21 shows its spectral response when $A_{\mathrm{In}_1} = e^{i\phi_1}$, $A_{\mathrm{Ad}} = e^{i\phi_{\mathrm{Add}}}$, $A_{\mathrm{In}_2} = e^{i\phi_2}$. Figure 21(a) shows the case of all three equal input phases ($(\phi_1, \phi_{\mathrm{Add}}, \phi_2) = (0, 0, 0)$): the Drop and the two Through signals are equal with slight differences caused by the bending losses. Figure 21(b) reproduces the case $(\phi_1,\ \phi_{\mathrm{Add}},\ \phi_2) = (0, \pi/4, \pi/2)$: at the resonance wavelength, the two Through signals are high while the Drop signals are low. The Through signal resonances are Fano resonances. Figure 21(c) represents the alternative case where only a π-shift on the Add signal is applied ($(\phi_1, \phi_{\mathrm{Add}}, \phi_2) = (0, \pi, 0)$): the Drop signal maximizes at resonance, while the two Through signals are low. Figure 21(d) shows the case when a π-shift is applied to both the Add and one Input signal $(\phi_1, \phi_{\mathrm{Add}}, \phi_2) = (0, \pi, \pi)$: all the input signals are addressed to the Through$_1$ port. The symmetric case where the signals are directed to the Through$_2$ port is obtained by applying the same phase shift to the other Input signal.

This three input signal configuration allows using the Add signal as a control signal to drive the interferometric

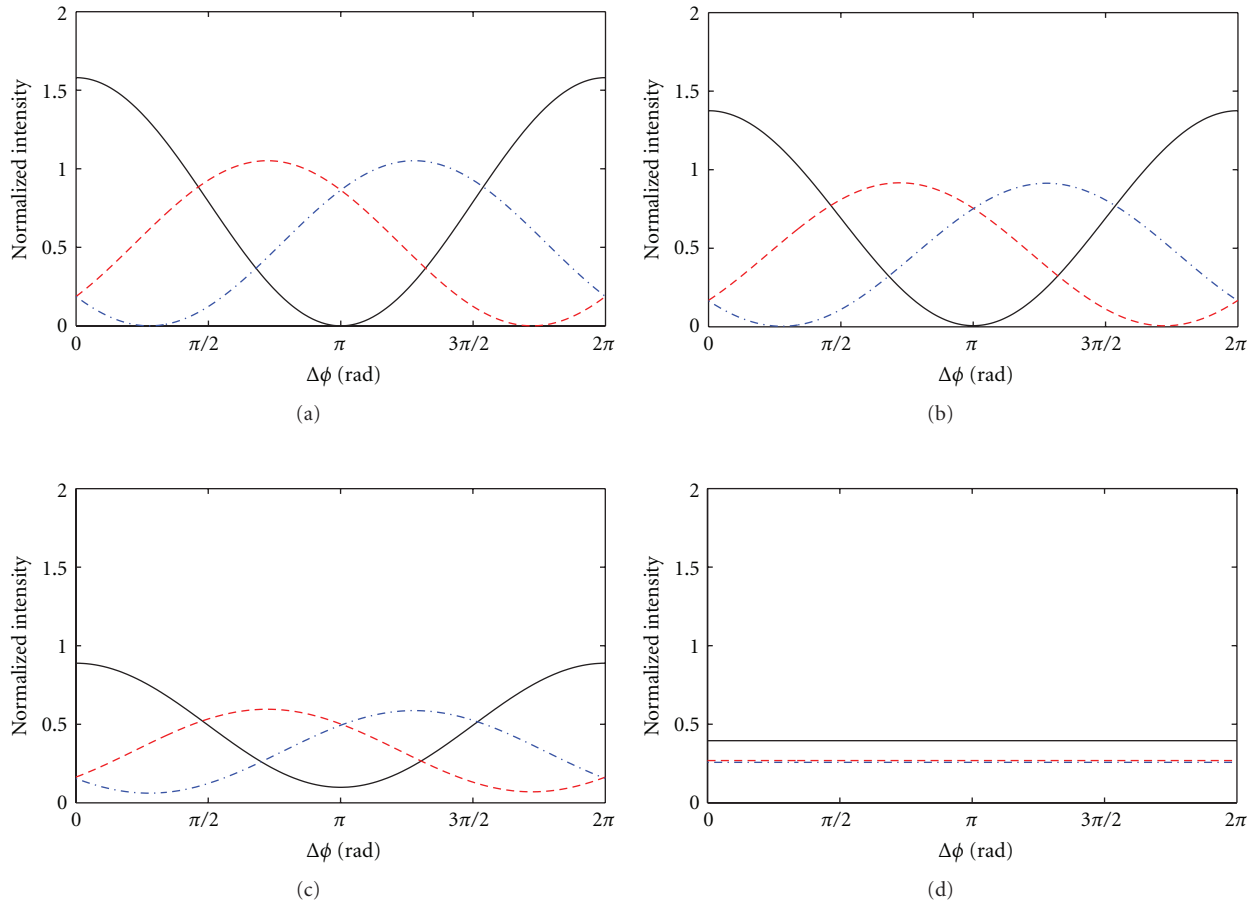

Figure 15: Phase response of the device in Figure 11 at λ_F, with $A_{\mathrm{In}_1} = e^{i\Delta\Phi}$, $A_{\mathrm{Ad}} = 0$, $|A_{\mathrm{In}_2}|^2 = (1,\ 0.75,\ 0.25,\ 0)$ ((a), (b), (c), (d), resp.). (Lines as in Figure 12.)

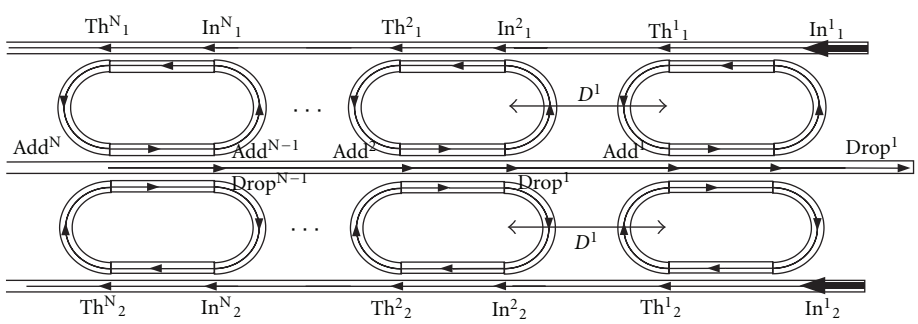

Figure 16: The $2 \times N$ SCISSOR phase switch.

switch to different functionalities (compare Figure 13 with Figure 21). In fact, if the phase of the Add signal is changed from 0 to π, the Drop signal is switched from 1 to 3 (in absence of bending losses); while, if the phase of one of the input is changed from 0 to π and $\phi_{\mathrm{Add}} = \pi$, one can switch off and on the Through signals. Many other sorts of combinations in phase and intensity at the Input ports, resonator numbers, and overall resonant device geometry for phase switching applications could be imagined in the most diverse configurations.

6. Conclusions

A three-bus waveguide multiple resonator-based interferometric switching device was discussed which is able to route light over a broad range of wavelengths by phase

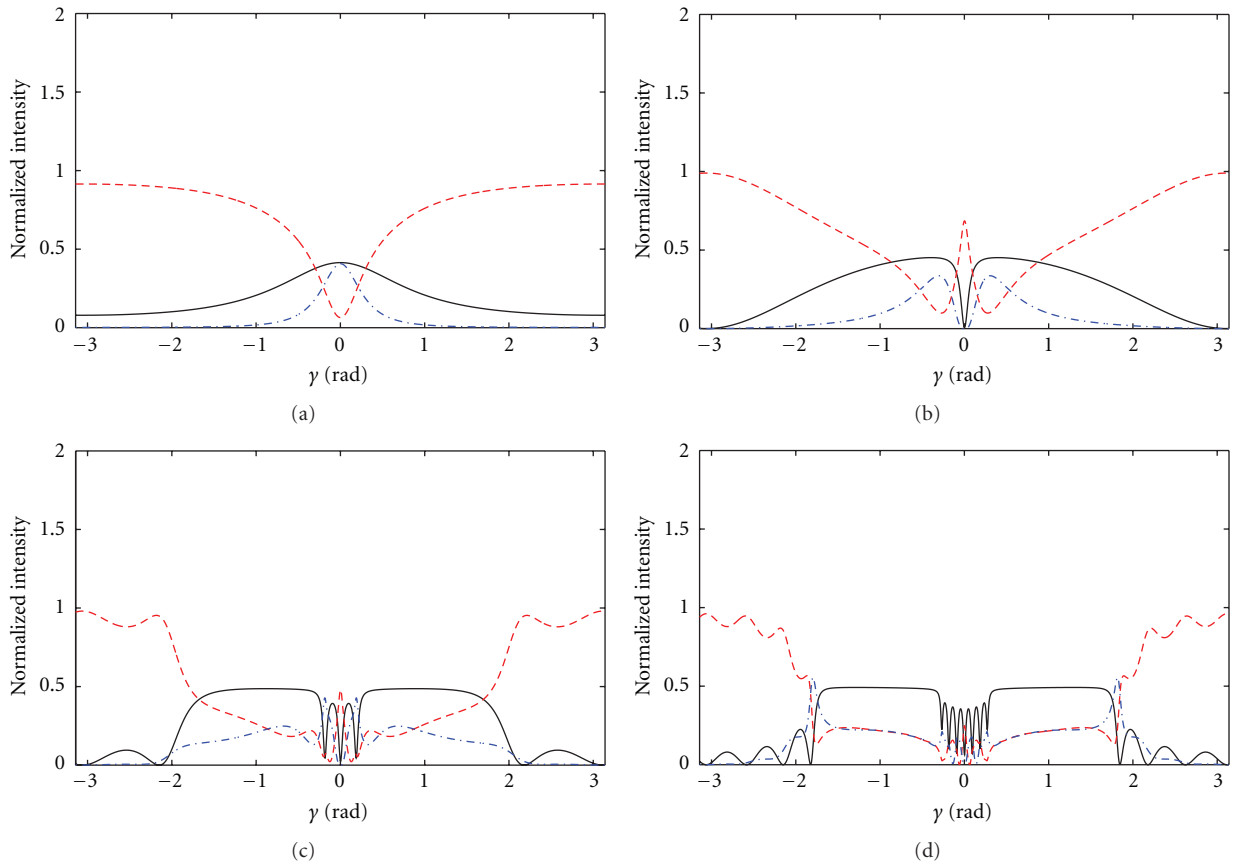

Figure 17: Spectral response of the SCISSOR switch with 1, 2, 4, 8 pairs of resonators ((a), (b), (c), (d), resp.) and inputs $A_{\mathrm{In}_1} = 1$, $A_{\mathrm{Ad}} = 0$, $A_{\mathrm{In}_2} = 0$. (Lines as in Figure 12.)

modulation. To obtain its behavior, it was necessary to analyze first the performance of the two bus waveguide single resonator and SCISSOR and CROW systems. We showed that extending side coupling and Mach-Zehnder phase switching techniques to multiple waveguides and to chains of resonators could be useful to enhance their switching capabilities. The proposed interferometer device shows the possibility to control a lightwave signal with the phase of another signal. This allows to add a further degree of freedom in designing reconfigurable optical routers and complex networks. Simple examples can be foreseen in single channel switches where the switch redirects the signal in two different channels without absorbing the light (Figure 7), or in a dual channel interleaver where the signal bands can be alternatively directed on one or the other channels by phase control (Figure 10(b)), or in a three channel router where the signal is routed along three different directions by controlling the wavelength and the phase (Figure 13(b)). It is clear, though, that the potentiality of the scheme proposed in this work is not exhausted by these examples and more can be envisaged by optical network specialists. However, we believe that herewith we outlined some proposals which display how this is a field with vast possibilities, hopefully inspiring further investigations of possible applications of novel interferometric switching devices.

Appendices

A.

Instead of displaying the spectral response of a resonant structure in terms of the wavelength, it is possible to express it as a resonator round trip dephasing, clearly with the assumption of a nondispersive system. The resonant wavelength of the mth mode, λ_m, is thus in general

$$\lambda_m = \frac{p_{\mathrm{opt}}(\lambda_m)}{m}, \tag{A.1}$$

with the wavelength-dependent optical path of the racetrack resonator $p_{\mathrm{opt}} = (2\pi R + 2L)n_{\mathrm{eff}}(\lambda_m)$, $n_{\mathrm{eff}}(\lambda_m)$ the effective index of the resonator waveguides at the mth resonant wavelength, and m the resonance azimutal number. In the case of dispersionless systems, (A.1) is no longer an implicit function, and any two modes at λ_1 and λ_2 are determined solely by the optical path of the resonator ($p_{\mathrm{opt}}(\lambda_m) = p_{\mathrm{opt}}$ for all m) and by the mode azimutal number m, as

$$\lambda_1 = \frac{p_{\mathrm{opt}}}{m}, \qquad \lambda_2 = \frac{p_{\mathrm{opt}}}{m+1}. \tag{A.2}$$

This means that the difference (i.e., the FSR) is

$$\lambda_2 - \lambda_1 = -\frac{p_{\mathrm{opt}}}{m(m+1)} = -\frac{\lambda_1}{m+1} = -\frac{\lambda_1\lambda_2}{p_{\mathrm{opt}}}. \tag{A.3}$$

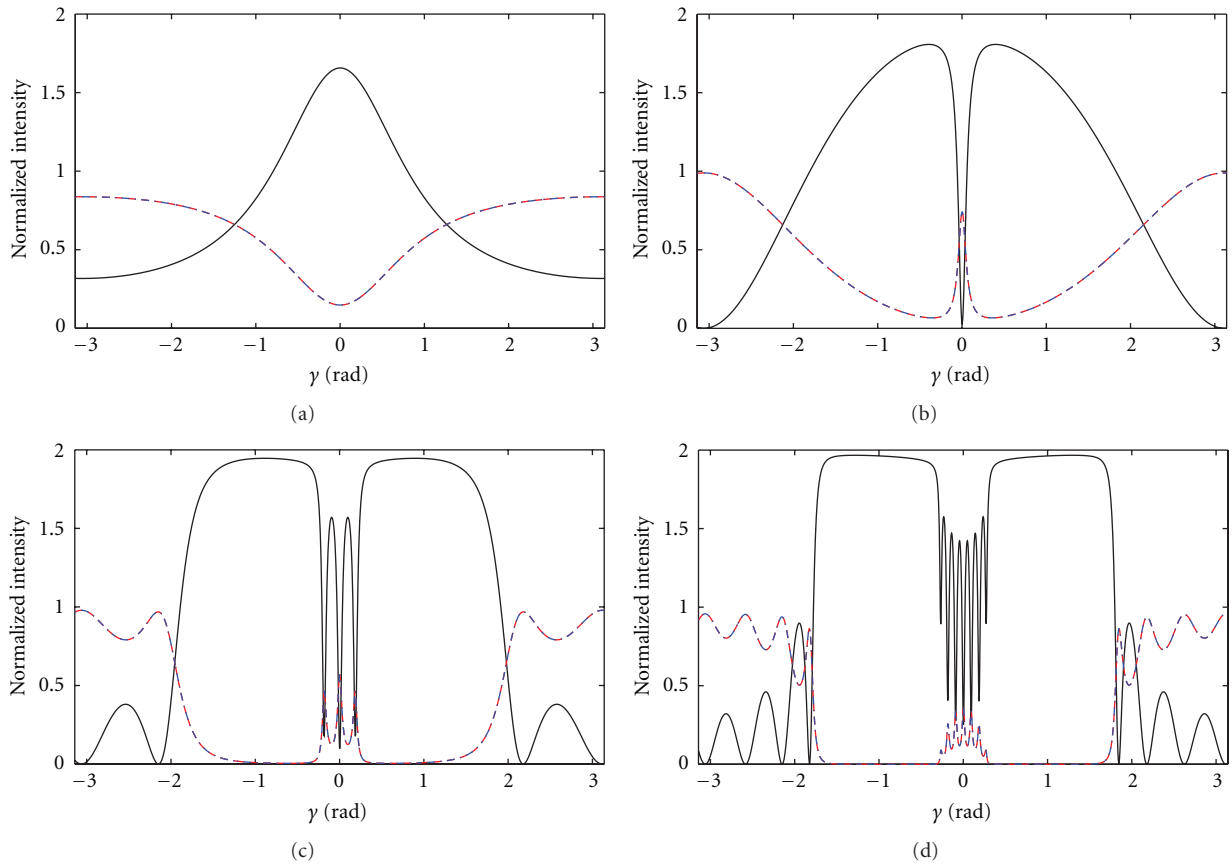

Figure 18: Spectral response of the SCISSOR switch with 1, 2, 4, 8 pairs of resonators ((a), (b), (c), (d), resp.), and inputs $A_{\mathrm{In}_1} = 1$, $A_{\mathrm{Ad}} = 0$, $A_{\mathrm{In}_2} = 1$, with same phase. (Lines as in Figure 12.)

Then, the parameter γ representing the round-trip dephasing of the resonator can be defined as an "angular deviation" from resonance at some wavelength λ as

$$\lambda = \lambda_1 + \frac{\gamma}{2\pi}(\lambda_2 - \lambda_1) = \lambda_1 - \frac{\gamma}{2\pi}\frac{\lambda_1\lambda_2}{p_{\mathrm{opt}}}, \tag{A.4}$$

and from which

$$\gamma = 2\pi p_{\mathrm{opt}}\frac{\lambda_1 - \lambda}{\lambda_1\lambda_2} \approx 2\pi p_{\mathrm{opt}}\frac{\Delta\lambda}{\lambda^2}. \tag{A.5}$$

B.

In Figure 11, we can relate $(A_3^2, A_4^2, A_5^2) \rightarrow (A_3^1, A_4^1, A_5^1)$ through (13) as

$$\begin{pmatrix} A_3^1 \\ A_4^1 \\ A_5^1 \end{pmatrix} = \mathcal{M}\begin{pmatrix} A_3^2 \\ A_4^2 \\ A_5^2 \end{pmatrix} = \begin{pmatrix} t' & i\kappa_D & -\kappa' \\ i\kappa_D & t_D & i\kappa_D \\ -\kappa' & i\kappa_D & t' \end{pmatrix}\begin{pmatrix} A_3^2 \\ A_4^2 \\ A_5^2 \end{pmatrix}. \tag{B.1}$$

Proceeding in the same way as we have done with matrix $\mathbf{M}$ of (25), we look for the coupling matrix that relates in the interference section the upper to the lower waveguide through the middle one, that is, $(A_3^2, A_4^2, A_3^1) \rightarrow (A_5^2, A_4^1, A_5^1)$, and obtain the second transfer matrix $\mathbf{T^b}$:

$$\begin{aligned} \begin{pmatrix} A_5^2 \\ A_4^1 \\ A_5^1 \end{pmatrix} &= \mathbf{T^b}\begin{pmatrix} A_3^2 \\ A_4^2 \\ A_3^1 \end{pmatrix} \\ &= \frac{1}{\kappa'}\begin{pmatrix} t' & i\kappa_D & -1 \\ i\kappa_D(\kappa' + t') & t_D\kappa' - \kappa_D^2 & -i\kappa_D \\ t'^2 - \kappa'^2 & i\kappa_D(\kappa' + t') & -t' \end{pmatrix}\begin{pmatrix} A_3^2 \\ A_4^2 \\ A_3^1 \end{pmatrix}. \end{aligned} \tag{B.2}$$

Due to a symmetric coupling, $\mathbf{K}$ of (26) can be applied also at $(A_6^1, A_6^2) \rightarrow (A_7^1, A_7^2)$. For the same reason, the same internal propagation matrix of (27) can be applied also at $(A_5^2, A_5^1) \rightarrow (A_6^1, A_6^2)$. Therefore, the third transfer matrix connects $(A_5^2, A_5^1) \rightarrow (A_7^1, A_7^2)$ in the same way as (28) (but with the order of the propagation and coupling matrixes inverted):

$$\begin{pmatrix} A_7^1 \\ A_7^2 \end{pmatrix} = \mathbf{T^{KP}}\begin{pmatrix} A_5^2 \\ A_5^1 \end{pmatrix} = \mathbf{KP}\begin{pmatrix} A_5^2 \\ A_5^1 \end{pmatrix}. \tag{B.3}$$

To proceed in the inverse direction, that is, from ports $(\mathrm{In}_2, \mathrm{Through}_2)$ to $(\mathrm{In}_1, \mathrm{Through}_1)$, note that, again because of coupling symmetry, $\mathbf{T^{PK}}$ relates also $(A_7^1, A_7^2) \rightarrow (A_5^2, A_5^1)$, $\mathbf{T^{KP}}$ does the same with $(A_3^2, A_3^1) \rightarrow (A_1^1, A_1^2)$, and $\mathbf{T^b}$ connects also $(A_5^2, A_4^2, A_5^1) \rightarrow (A_3^2, A_4^1, A_3^1)$.

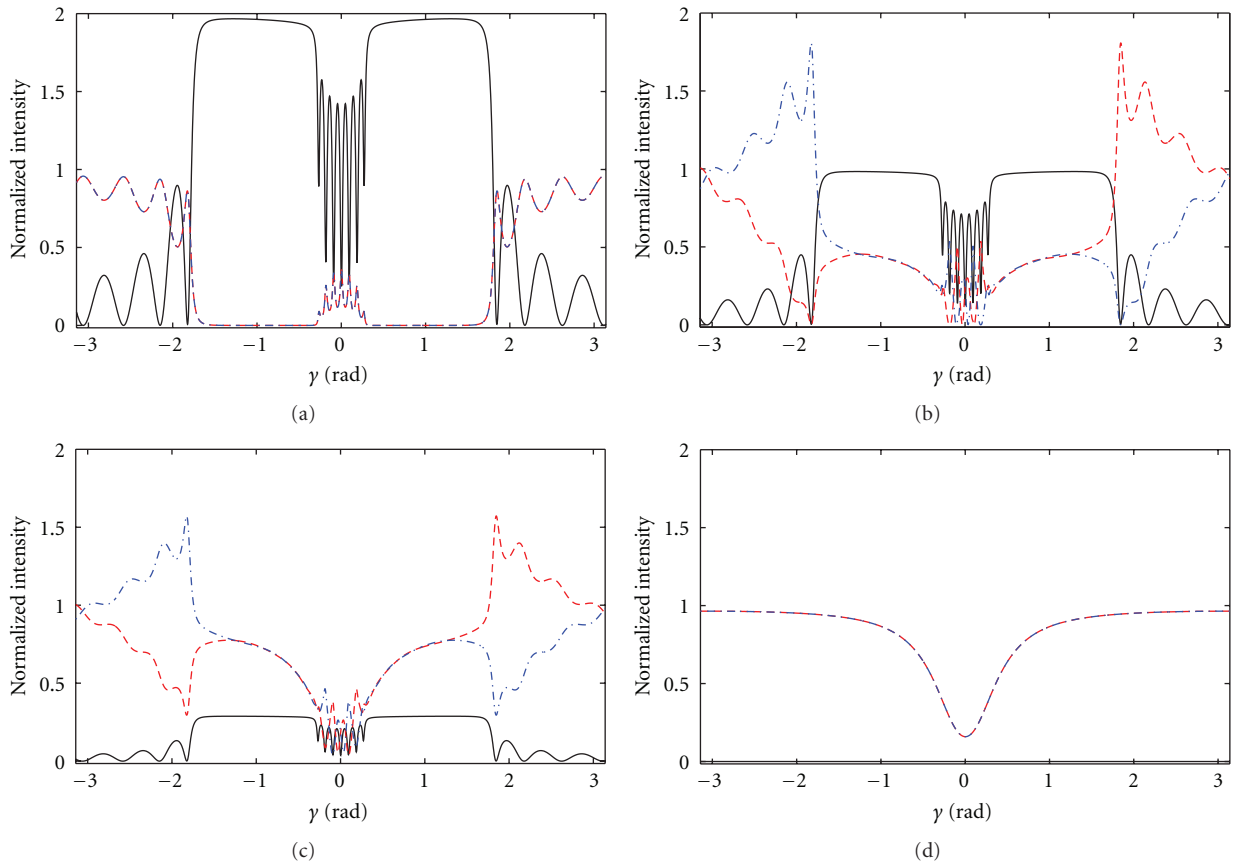

Figure 19: Spectral response of the 2×8 SCISSOR switch of Figure 16 with inputs, $A_{\mathrm{In}_1} = (1,\ e^{i(\pi/2)}, e^{i(3/4)\pi}, e^{i\pi})$ ((a), (b), (c), (d) resp.), $A_{\mathrm{Ad}} = 0$, $A_{\mathrm{In}_2} = 1$ (Lines as in Figure 12.)

Now, we can obtain the overall device response of Figure 11 by separating the contributions to the two Through and the Drop ports as the sum of three different terms corresponding to the three following device states.

State (I). Input signal in In_1 only is injected and propagated from the top to the bottom of the device

$$\begin{pmatrix} A_{\mathrm{In}_1} = |A_{\mathrm{In}_1}| e^{i\phi_1} \\ A_{\mathrm{Ad}} = 0 \\ A_{\mathrm{In}_2} = 0 \end{pmatrix} \longmapsto \begin{pmatrix} A_{\mathrm{Th}_1^{(\mathrm{I})}} \\ A_{D^{(\mathrm{I})}} \\ A_{\mathrm{Th}_2^{(\mathrm{I})}} \end{pmatrix}. \tag{B.4}$$

Schematically, this goes as follows (from the right to the left):

$$\longleftarrow \begin{pmatrix} A_3^2 \\ A_3^1 \end{pmatrix} = \mathbf{T^{PK}} \begin{pmatrix} A_{\mathrm{In}_1} \\ A_{\mathrm{Th}_1^{(\mathrm{I})}} \end{pmatrix} \tag{B.5}$$

$$\longleftarrow \begin{pmatrix} A_5^2 \\ A_{D^{(\mathrm{I})}} \\ A_5^1 \end{pmatrix} = \mathbf{T^b} \begin{pmatrix} A_3^2 \\ 0 \\ A_3^1 \end{pmatrix} \longleftarrow \tag{B.6}$$

$$\begin{pmatrix} 0 \\ A_{\mathrm{Th}_2^{(\mathrm{I})}} \end{pmatrix} = \mathbf{T^{KP}} \begin{pmatrix} A_5^2 \\ A_5^1 \end{pmatrix} \longleftarrow . \tag{B.7}$$

This means that the first set of equations from the first transferral of (B.5)

$$\begin{aligned} A_3^2 &= T_{11}^{\mathrm{PK}} A_{\mathrm{In}_1} + T_{12}^{\mathrm{PK}} A_{\mathrm{Th}_1^{(\mathrm{I})}}, \\ A_3^1 &= T_{21}^{\mathrm{PK}} A_{\mathrm{In}_1} + T_{22}^{\mathrm{PK}} A_{\mathrm{Th}_1^{(\mathrm{I})}}, \end{aligned} \tag{B.8}$$

have to be inserted into (B.6) to obtain

$$\begin{aligned} A_5^2 = {} & \left(T_{11}^b T_{11}^{\mathrm{PK}} + T_{13}^b T_{21}^{\mathrm{PK}}\right) A_{\mathrm{In}_1} \\ & + \left(T_{11}^b T_{12}^{\mathrm{PK}} + T_{13}^b T_{22}^{\mathrm{PK}}\right) A_{\mathrm{Th}_1^{(\mathrm{I})}}, \end{aligned} \tag{B.9}$$

$$\begin{aligned} A_{D^{(\mathrm{I})}} = {} & \left(T_{21}^b T_{11}^{\mathrm{PK}} + T_{23}^b T_{21}^{\mathrm{PK}}\right) A_{\mathrm{In}_1} \\ & + \left(T_{21}^b T_{12}^{\mathrm{PK}} + T_{23}^b T_{22}^{\mathrm{PK}}\right) A_{\mathrm{Th}_1^{(\mathrm{I})}}, \end{aligned} \tag{B.10}$$

$$\begin{aligned} A_5^1 = {} & \left(T_{31}^b T_{11}^{\mathrm{PK}} + T_{33}^b T_{21}^{\mathrm{PK}}\right) A_{\mathrm{In}_1} \\ & + \left(T_{31}^b T_{12}^{\mathrm{PK}} + T_{33}^b T_{22}^{\mathrm{PK}}\right) A_{\mathrm{Th}_1^{(\mathrm{I})}}. \end{aligned} \tag{B.11}$$

Proceeding further with the next transfer, we have from (B.7) that

$$\begin{aligned} 0 &= T_{11}^{\mathrm{KP}} A_5^2 + T_{12}^{\mathrm{KP}} A_5^1, \\ A_{\mathrm{Th}_2^{(\mathrm{I})}} &= T_{21}^{\mathrm{KP}} A_5^2 + T_{22}^{\mathrm{KP}} A_5^1, \end{aligned} \tag{B.12}$$

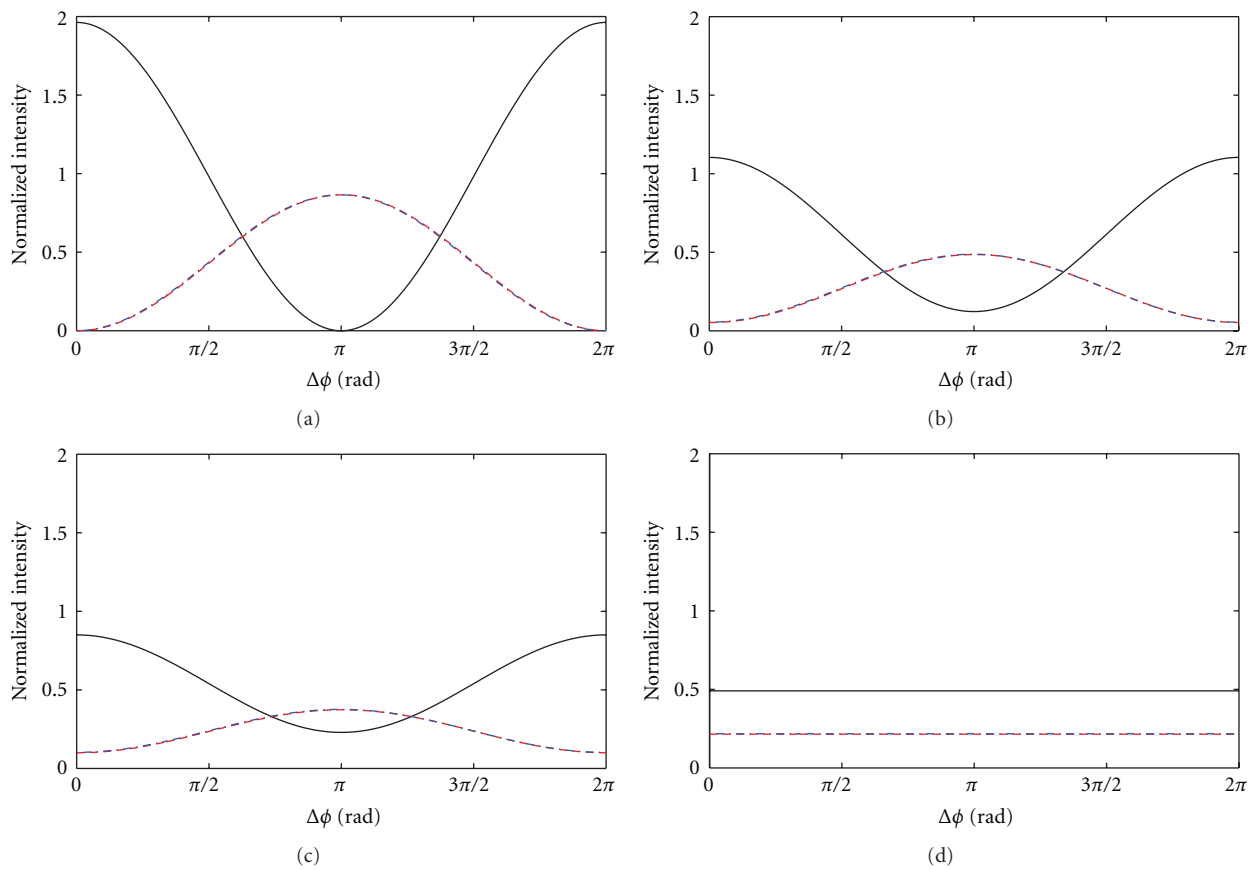

FIGURE 20: Phase response of the 2×8 SCISSOR switch of Figure 16 with input imbalances $|A_{\mathrm{In}_1}|^2 = (1,\ 0.25,\ 0.1,\ 0)$ ((a), (b), (c), (d), resp.), $A_{\mathrm{Ad}} = 0$, $A_{\mathrm{In}_2} = 1$, at phase round-trip shift $\gamma = 1$ (Lines as in Figure 12.)

which, through (B.9), (B.10), and (B.11), leads to

$$\begin{aligned} A_{\mathrm{Th}_1^{(\mathrm{I})}} &= T_{11} A_{\mathrm{In}_1}, \\ A_{D^{(\mathrm{I})}} &= T_{21} A_{\mathrm{In}_1}, \\ A_{\mathrm{Th}_2^{(\mathrm{I})}} &= T_{31} A_{\mathrm{In}_1}, \end{aligned} \tag{B.13}$$

with

$$\begin{aligned} T_{11} &= -\frac{T_{11}^{\mathrm{KP}} A + T_{12}^{\mathrm{KP}} B}{T_{11}^{\mathrm{KP}} C + T_{12}^{\mathrm{KP}} D}, \\ T_{21} &= E + F T_{11}, \\ T_{31} &= G + H T_{11}, \\ A &= T_{11}^{b} T_{11}^{\mathrm{PK}} + T_{13}^{b} T_{21}^{\mathrm{PK}}, \\ B &= T_{31}^{b} T_{11}^{\mathrm{PK}} + T_{33}^{b} T_{21}^{\mathrm{PK}}, \\ C &= T_{11}^{b} T_{12}^{\mathrm{PK}} + T_{13}^{b} T_{22}^{\mathrm{PK}}, \\ D &= T_{31}^{b} T_{12}^{\mathrm{PK}} + T_{33}^{b} T_{22}^{\mathrm{PK}}, \\ E &= T_{21}^{b} T_{11}^{\mathrm{PK}} + T_{23}^{b} T_{21}^{\mathrm{PK}}, \\ F &= T_{21}^{b} T_{12}^{\mathrm{PK}} + T_{23}^{b} T_{22}^{\mathrm{PK}}, \\ G &= T_{21}^{\mathrm{KP}} A + T_{22}^{\mathrm{KP}} B, \\ H &= T_{21}^{\mathrm{KP}} C + T_{22}^{\mathrm{KP}} D. \end{aligned} \tag{B.14}$$

State (II). Input signal in In_2 only is injected and propagated from the bottom to the top of the device.

$$\begin{pmatrix} A_{\mathrm{In}_1} = 0 \\ A_{\mathrm{Ad}} = 0 \\ A_{\mathrm{In}_2} = |A_{\mathrm{In}_2}| e^{i\phi_2} \end{pmatrix} \longmapsto \begin{pmatrix} A_{\mathrm{Th}_1^{(\mathrm{III})}} \\ A_{D^{(\mathrm{III})}} \\ A_{\mathrm{Th}_2^{(\mathrm{III})}} \end{pmatrix}. \tag{B.15}$$

One proceeds exactly as for State (I), but in the opposite direction. The only difference in the final result is that in (B.13) the ports (In_1, $\mathrm{Through}_1^{(\mathrm{I})}$, $\mathrm{Through}_2^{(\mathrm{I})}$) have to be exchanged with (In_2, $\mathrm{Through}_2^{(\mathrm{III})}$, $\mathrm{Through}_1^{(\mathrm{III})}$):

$$\begin{aligned} A_{\mathrm{Th}_1^{(\mathrm{III})}} &= T_{13} A_{\mathrm{In}_2}, \\ A_{\mathrm{Drop}^{(\mathrm{III})}} &= T_{23} A_{\mathrm{In}_2}, \\ A_{\mathrm{Th}_2^{(\mathrm{III})}} &= T_{33} A_{\mathrm{In}_2}, \end{aligned} \tag{B.16}$$

with $T_{13} = T_{31}$, $T_{23} = T_{21}$, and $T_{33} = T_{11}$.

State (III). Add port signal only is injected and propagated from the central Add waveguide towards the Drop and upper and lower Through ports.

In the transfer matrix of (35), only one coefficient is missing, namely, T_{22}. This is fixed by the other matrix elements and power conservation criteria. Expressing explicitly

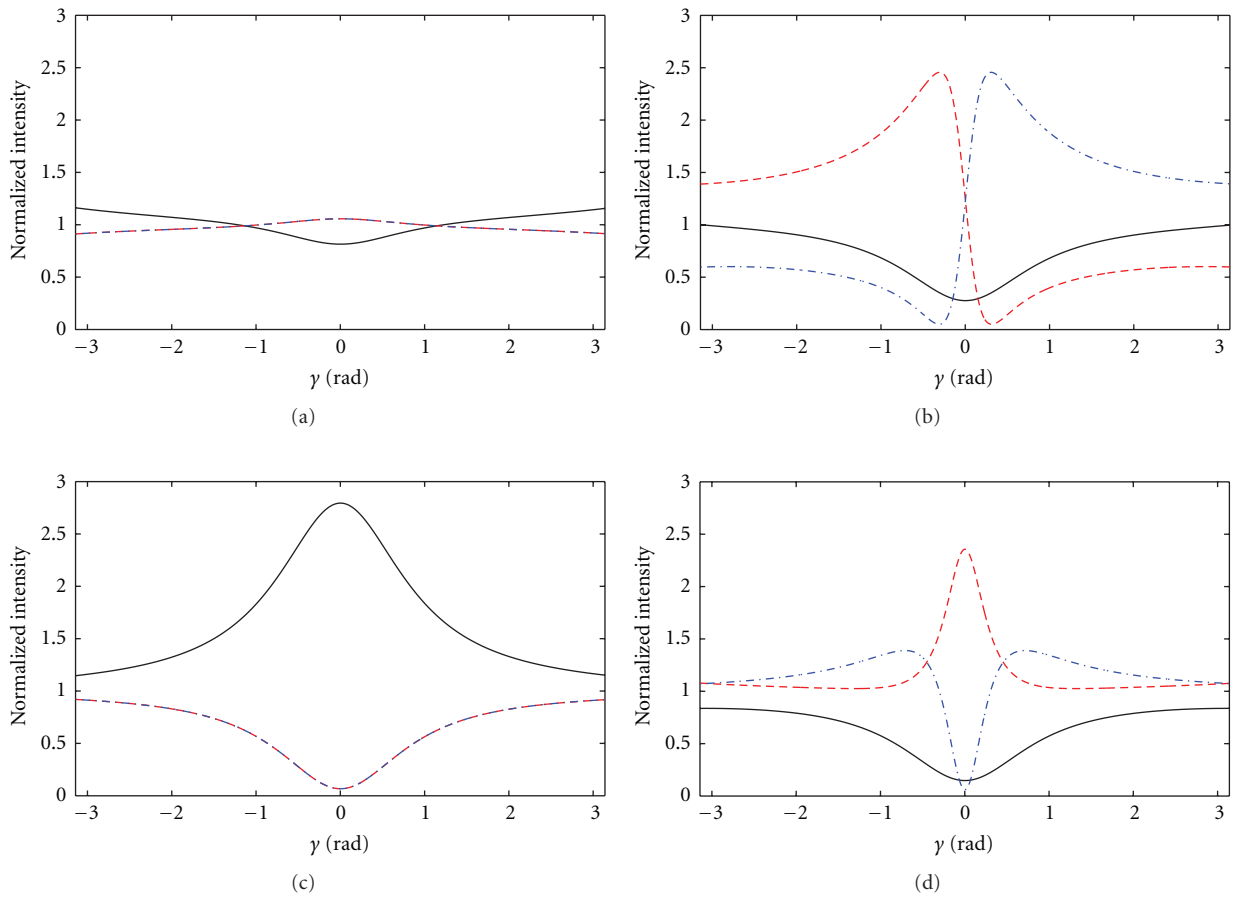

Figure 21: Spectral response of the 2×1 SCISSOR switch of Figure 16 with inputs $A_{\mathrm{In}_1} = e^{i\phi_1}$, $A_{\mathrm{Ad}} = e^{i\phi_{\mathrm{Add}}}$, $A_{\mathrm{In}_2} = e^{i\phi_2}$, and $(\phi_1, \phi_{\mathrm{Add}}, \phi_2) = (0, 0, 0)$; $(\phi_1, \phi_{\mathrm{Add}}, \phi_2) = (0,\ \pi/4,\ \pi/2)$; $(\phi_1, \phi_{\mathrm{Add}}, \phi_2) = (0, \pi, 0)$; $(\phi_1, \phi_{\mathrm{Add}}, \phi_2) = (0, \pi, \pi)$ for figures (a), (b), (c), (d), respectively (Lines as in Figure 12.)

with the matrix elements of **T** the power balance between the input and output intensities of the waves, it must hold:

$$\begin{aligned}
&|A_{\mathrm{In}_1}|^2 + |A_{\mathrm{In}_2}|^2 + |A_{\mathrm{Ad}}|^2 \\
&= |A_{\mathrm{Th}_1}|^2 + |A_D|^2 + |A_{\mathrm{Th}_2}|^2 + \mathrm{Loss} \\
&= \left(|T_{11}|^2 + |T_{21}|^2 + |T_{31}|^2\right)\left(|A_{\mathrm{In}_1}|^2 + |A_{\mathrm{In}_2}|^2\right) \\
&\quad + \left(2|T_{21}|^2 + |T_{22}|^2\right)|A_{\mathrm{Ad}}|^2 \\
&\quad + \left(T_{11}T_{31}^* + |T_{21}|^2 + T_{31}T_{11}^*\right)\left(A_{\mathrm{In}_1}A_{\mathrm{In}_2}^* + A_{\mathrm{In}_1}^*A_{\mathrm{In}_2}\right) \\
&\quad + \left(T_{11}T_{21}^* + T_{21}T_{22}^* + T_{31}T_{21}^*\right)\left(A_{\mathrm{In}_1} + A_{\mathrm{In}_1}\right)A_{\mathrm{Ad}}^* \\
&\quad + \left(T_{11}^*T_{21} + T_{21}^*T_{22} + T_{31}^*T_{21}\right)\left(A_{\mathrm{In}_1}^* + A_{\mathrm{In}_2}\right)A_{\mathrm{Ad}} + \mathrm{Loss},
\end{aligned} \tag{B.17}$$

with the last term indicating the losses of the structure. This implies the following conditions:

$$|T_{11}|^2 + |T_{21}|^2 + |T_{31}|^2 = 1, \tag{B.18}$$

$$2|T_{21}|^2 + |T_{22}|^2 = 1, \tag{B.19}$$

$$T_{11}T_{31}^* + |T_{21}|^2 + T_{31}T_{11}^* = 0, \tag{B.20}$$

$$T_{11}^*T_{21} + T_{21}^*T_{22} + T_{31}^*T_{21} = 0. \tag{B.21}$$

Conditions (B.18) and (B.20) are already satisfied by the coefficients found in the two previous cases (very cumbersome and long calculations). From (B.21), we finally obtain the last coefficient for matrix (35):

$$T_{22} = -\frac{T_{21}}{T_{21}^*}\left(T_{11}^* + T_{31}^*\right), \tag{B.22}$$

which satisfies also (B.19) through (B.20).

Acknowledgment

The authors acknowledge support of the EU through the FP7 ICT-(216405) Project Wavelength Division Multiplexed Photonic Layer on CMOS.

References

[1] T. S. El-Bawab, *Optical Switching*, Springer, 2006.

[2] A. Yariv, Y. Xu, R. K. Lee, and A. Scherer, "Coupled-resonator optical waveguide: a proposal and analysis," *Optics Letters*, vol. 24, no. 11, pp. 711–713, 1999.

[3] J. E. Heebner, R. W. Boyd, and Q. H. Park, "SCISSOR solitons and other novel propagation effects in microresonator-modified waveguides," *Journal of the Optical Society of America B*, vol. 19, no. 4, pp. 722–731, 2002.

[4] J. E. Heebner, P. Chak, S. Pereira, J. E. Sipe, and R. W. Boyd, "Distributed and localized feedback in microresonator sequences for linear and nonlinear optics," *Journal of the Optical Society of America B*, vol. 21, no. 10, pp. 1818–1832, 2004.

[5] J. Capmany, P. Muñoz, J. D. Domenech, and M. A. Muriel, "Apodized coupled resonator waveguides," *Optics Express*, vol. 15, no. 16, pp. 10196–10206, 2007.

[6] S. Y. Cho and R. Soref, "Apodized SCISSORs for filtering and switching," *Optics Express*, vol. 16, no. 23, pp. 19078–19090, 2008.

[7] D. U. Smith, H. Chang, K. A. Fuller, A. T. Rosenberger, and R. W. Boyd, "Coupled-resonator-induced transparency," *Physical Review A*, vol. 69, no. 6, Article ID 063804, 6 pages, 2004.

[8] Q. Xu, S. Sandhu, M. L. Povinelli, J. Shakya, S. Fan, and M. Lipson, "Experimental realization of an on-chip all-optical analogue to electromagnetically induced transparency," *Physical Review Letters*, vol. 96, no. 12, Article ID 123901, 4 pages, 2006.

[9] Y. F. Xiao, X. B. Zou, W. Jiang, Y. L. Chen, and G. C. Guo, "Analog to multiple electromagnetically induced transparency in all-optical drop-filter systems," *Physical Review A*, vol. 75, no. 6, Article ID 063833, 4 pages, 2007.

[10] X. Yang, M. Yu, D. L. Kwong, and C. W. Wong, "All-optical analog to electromagnetically induced transparency in multiple coupled photonic crystal cavities," *Physical Review Letters*, vol. 102, no. 17, Article ID 173902, 4 pages, 2009.

[11] M. Mancinelli, R. Guider, M. Masi et al., "Optical characterization of a SCISSOR device," *Optics Express*, vol. 19, no. 14, pp. 13664–13674, 2011.

[12] M. Masi, M. Mancinelli, A. Battarelli et al., "A silicon photonic interferometric router device based on SCISSOR concept," *Journal of Lightwave Technology*, vol. 29, no. 18, pp. 2747–2753, 2011.

[13] "Technology focus on Lithography," *Nature Photonics*, vol. 4, no. 1, 2010.

[14] G. T. Reed, G. Mashanovich, F. Y. Gardes, and D. J. Thomson, "Silicon optical modulators," *Nature Photonics*, vol. 4, article 660, 2010.

[15] K. Okamoto, *Fundamentals of Optical Waveguides*, Academic Press, 2nd edition, 2006.

[16] Y. M. Landobasa, S. Darmawan, and M. K. Chin, "Matrix analysis of 2-d microresonator lattice optical filters," *IEEE Journal of Quantum Electronics*, vol. 41, no. 11, pp. 1410–1418, 2005.

[17] J. K. S. Poon, J. Scheuer, S. Mookherjea, G. T. Paloczi, Y. Huang, and A. Yariv, "Matrix analysis of microring coupled-resonator optical waveguides," *Optics Express*, vol. 12, no. 1, pp. 90–103, 2004.

[18] C.-S. Ma, X. Yan, and X.-Y. Wang, "Matrix analysis of 2D microring resonator arrays," *Journal of Modern Optics*, vol. 55, no. 1, pp. 143–154, 2008.

[19] J. K. S. Poon, P. Chak, J. M. Choi, and A. Yariv, "Slowing light with Fabry-Perot resonator arrays," *Journal of the Optical Society of America B*, vol. 24, no. 11, pp. 2763–2769, 2007.

[20] S. Y. Cho and R. Soref, "Interferometric microring-resonant 2×2 optical switches," *Optics Express*, vol. 16, no. 17, pp. 13304–13314, 2008.

[21] F. Xia, L. Sekaric, M. O'Boyle, and Y. Vlasov, "Coupled resonator optical waveguides based on silicon-on-insulator photonic wires," *Applied Physics Letters*, vol. 89, no. 4, Article ID 041122, 3 pages, 2006.

[22] M. Masi, R. Orobtchouk, G. Fan, J. M. Fedeli, and L. Pavesi, "Towards a realistic modelling of ultra-compact racetrack resonators," *Journal of Lightwave Technology*, vol. 28, no. 22, pp. 3233–3242, 2010.

[23] U. Fano, "Sullo spettro di assorbimento dei gas nobili presso il limite dello spettro d'arco," *Nuovo Cimento*, vol. 12, no. 3, pp. 154–161, 1935.

[24] U. Fano, "Effects of configuration interaction on intensities and phase shifts," *Physical Review*, vol. 124, no. 6, pp. 1866–1878, 1961.

Hindawi Publishing Corporation
International Journal of Optics
Volume 2012, Article ID 764084, 7 pages
doi:10.1155/2012/764084

Research Article

Detailed Theoretical Model for Adjustable Gain-Clamped Semiconductor Optical Amplifier

Lin Liu,[1] Craig Michie,[1] Anthony E. Kelly,[2] and Ivan Andonovic[1]

[1] *Department of Electronic and Electrical Engineering, University of Strathclyde, Glasgow G1 1XW, UK*
[2] *Department of Electronics and Electrical Engineering, University of Glasgow, Glasgow G12 8LT, UK*

Correspondence should be addressed to Ivan Andonovic, i.andonovic@eee.strath.ac.uk

Received 1 October 2011; Revised 7 February 2012; Accepted 11 February 2012

Academic Editor: Luciano Mescia

The adjustable gain-clamped semiconductor optical amplifier (AGC-SOA) uses two SOAs in a ring-cavity topology: one to amplify the signal and the other to control the gain. The device was designed to maximize the output saturated power while adjusting gain to regulate power differences between packets without loss of linearity. This type of subsystem can be used for power equalisation and linear amplification in packet-based dynamic systems such as passive optical networks (PONs). A detailed theoretical model is presented in this paper to simulate the operation of the AGC-SOA, which gives a better understanding of the underlying gain clamping mechanics. Simulations and comparisons with steady-state and dynamic gain modulation experimental performance are given which validate the model.

1. Introduction

Semiconductor optical amplifiers (SOAs) have attracted considerable attention during the last two decades, for use in evolving optical communication networks. SOAs can be used as not only optical amplifiers, but also signal processing devices such as wavelength converters [1], optical switches [2], and electro-optical mixers [3]. In terms of optical amplification, the key issue of operating SOAs is the management of the input optical signal power, which must be maintained within the linear regime of operation; otherwise the device would be driven into saturation causing unwanted intersymbol interference (ISI) or patterning. In order to solve this implementation problem, many different types of gain-clamped semiconductor optical amplifiers (GC-SOAs) have been proposed [4, 5]. Recently, an adjustable gain-clamped semiconductor optical amplifier (AGC-SOA) designed to maximize the output saturated power at a clamped gain which can be adjusted was reported [6].

2. AGC-SOA

The AGC-SOA is a semiconductor optical amplifier topology which has the unique capability to provide variable gain and maintain linear operation through gain clamping over a wide (40 dB) dynamic range, without compromising the saturable output power of the device [6]. A key advantage of this approach is that there are no mechanical tuning elements, and hence the gain can be adjusted via direct electrical control at ns timescales. While the operation of this device has been presented previously for the static gain case [6], and its behaviour under dynamic gain modulation conditions [7], the underlying mechanics is not well understood. Here, a theoretical model for an AGC-SOA has been established, based on the wideband steady-state numerical model of a SOA [8]. The travelling amplified spontaneous emission (ASE) power and spectrum within a ring cavity, steady-state, and dynamic gain modulation have been studied. Simulations are in broad agreement with experiment results.

Figure 1 illustrates conceptually the design of the adjustable gain clamped SOA (AGC-SOA). The architecture comprises two active (gain) regions defining a data path through the signal SOA (SOA1) and a laser cavity containing SOA1 and a control SOA (SOA2). SOA1 amplifies light in the signal path. The lasing mode derives gain from both SOA1 and SOA2. The composite gain provided by both SOAs regulates the condition for the onset of lasing. This in turn defines the carrier concentration (gain) of the signal SOA. Hence,

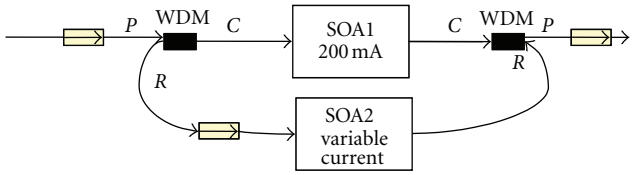

Figure 1: Counterpropagating ring laser adjustable gain-clamped SOA (AGC-SOA) implementation.

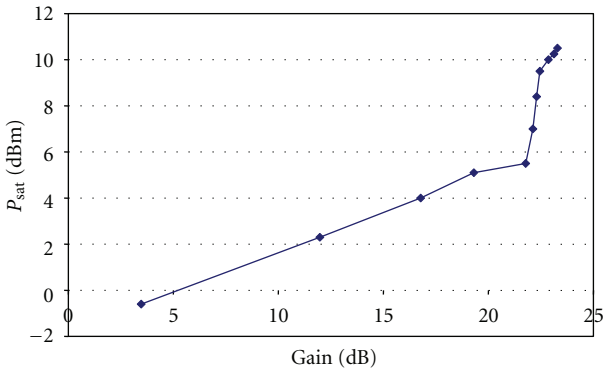

Figure 2: P_{sat} (dBm) variation as a function of SOA gain (dB).

by controlling the drive to SOA2, the gain imparted by SOA1 can be adjusted. SOA1 is continually operated at full current, and therefore, the AGC-SOA allows signals to be amplified by SOA1 at a clamped gain which is varied by SOA2. This maximises the saturation output power thereby maintaining an extended linear regime [6].

The key advantage that the AGC-SOA offers over other optical amplifiers is that it enables the gain to be adjusted directly through the drive current to the clamping SOA without the dramatic loss of P_{sat}. Hence, linear operation is maintained over a wider range of input signals. In standard SOAs, it is possible to adjust the gain by altering the drive current however, as is demonstrated in the experimental measurement shown in Figure 2, and this leads to a dramatic loss in P_{sat}.

At high gains, where the SOA is highly inverted, the P_{sat} value is at its highest. However, in this region, adjusting the small signal gain through bias current has a dramatic effect on the P_{sat} value. In the example depicted in Figure 2, at high gains the P_{sat} changes with gain at a rate of ~3 dBm/dB i.e., for every dB that the gain is reduced, the P_{sat} value drops by 3 dBm. As the drive current is further reduced, the drop in P_{sat} with gain is weaker at ~0.4 dBm/dB. However, by the time that this point has been reached, the P_{sat} value is already significantly compromised (5 dBm compared to the high gain value of 10 dBm). The AGC-SOA enables gain modulation to be achieved without this dramatic loss of P_{sat} value.

Figure 3 depicts the gain of AGC-SOA as a function of output power for a set of different clamping currents ranging from 0 mA to 200 mA. The P_{sat} values are constant over the range of clamping currents despite significant gain reduction (>20 dB), demonstrated in Figure 4.

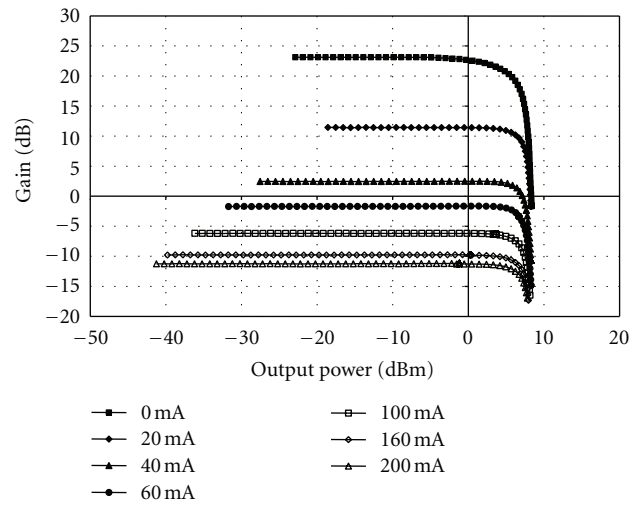

Figure 3: AGC-SOA gain as a function of output power at different clamping currents. Legend: bias current of SOA2.

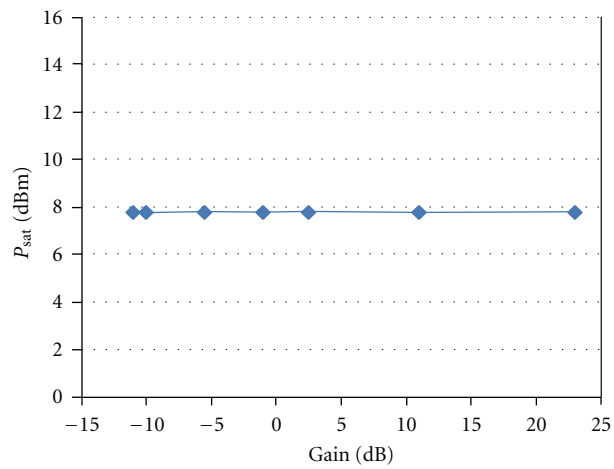

Figure 4: P_{sat} (dBm) variation as a function of AGC-SOA gain (dB).

Additional steady-state experimental results such as gain, Noise Figure (NF), and P_{sat} value were demonstrated in [6]. The dynamic gain modulation performance of AGC-SOA was further studied in [7]. In a dynamic packet equalisation scenario, the AGC-SOA is able to adjust and stabilise its gain in less than 2 ns, within the period of the guard band of the passive optical network (PON) transmission at 1.25 Gbit/s on the upstream direction, 32 bit periodsis equates to 26 ns. Similarly for 10-Gigabit-capable, PON system, the guard time is 64 bits at 2.5 Gbit/s on the upstream direction [9], this equates to 26 ns [9].

3. Model of AGC-SOA

Several numerical models have been developed to investigate the characteristics of both conventional SOAs [8] and gain-clamped SOAs using either an external [10, 11] or internal [12, 13] lasing mode. However, the underlying mechanism of gain clamping achieved by adjusting wideband amplified

Table 1: Device parameters used in AGC-SOA simulation.

Symbol	Parameters	SOA1	SOA2
L_c	Central active region length	400 μm	840 μm
L_t	Tapered active region length	200 μm	160 μm
d	Active region thickness	0.4 μm	0.1 μm
W	Active region width	0.4 μm	1.1 μm
y	Molar fraction of arsenide	0.892	0.816
Γ	Confinement factor	0.15	0.15
R_1	Input facet reflectivity	5×10^{-5}	1×10^{-5}
R_2	Output facet reflectivity	5×10^{-5}	1×10^{-5}
η_{in}	Input coupling loss	3 dB	2 dB
η_{out}	Output coupling loss	3 dB	2 dB
K_0	Carrier-independent absorption loss coefficient	6200 m^{-1}	3000 m^{-1}
K_1	Carrier-dependent absorption loss coefficient	7.5×10^{-21} m^2	6.83×10^{-21} m^2
n_1	Active region refractive index	3.22	3.56
C_1		3.7×10^8 s^{-1}	
C_2	Recombination coefficients	5.6×10^{-16} m^3/s	
C_3		3×10^{-41} m^6/s	
α_{coupler}	WDM coupler pass band insertion loss	0.5 dB	

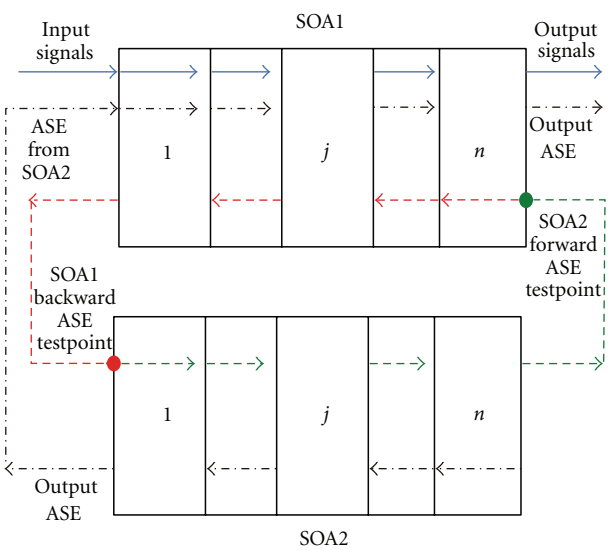

Figure 5: Schematic of the simulation model for an AGC-SOA.

spontaneous emission (ASE) power still remains largely unknown. In this study, the wideband steady-state SOA model [8] is adapted to form a ring cavity; the evolution of travelling ASE power and spectrum within the ring cavity, important for gain clamping, is then characterised. The gain, Noise Figure (NF), and maximum output power at gain saturation (P_{sat}) of an AGC-SOA under different clamping currents are also studied. Based on this model, the timescale for adjusting and stabilising the gain, crucial for dynamic packet equalisation, is evaluated.

As shown in Figure 5, ASE circulating within the AGC-SOA travels in clockwise and counterclockwise directions, however, the isolator in the ring cavity ensures that ASE travelling in the clockwise direction is not amplified. Thus, the counterclockwise ASE generated by both SOAs accounts for gain clamping. In this model, the two SOAs are simulated as independent modules using different sets of material parameters summarised in Table 1. (Typical bulk SOA parameters from [8, 14, 15]). Both SOAs generate ASE in the forward and backward directions in the active regions. In each SOA, the ASE profile extends over 1300 nm ~1650 nm and is partitioned into discrete frequency bands.

In order to simulate the wideband ASE profile for a single SOA, the material gain coefficient of the SOA active region in an InGaAsP direct bandgap bulk material is given by [8, 16]

$$\begin{aligned} g_m(\nu, n) &= \frac{c^2}{4\sqrt{2}\pi^{3/2} n_1^2 \tau \nu^2} \left(\frac{2 m_e m_{\text{hh}}}{\hbar (m_e + m_{\text{hh}})} \right)^{3/2} \\ &\quad \times \int_0^\infty \left(\nu' - \frac{E_g}{h} \right)^{1/2} \times \left(f_c(\nu') - f_v(\nu') \right) \\ &\quad \times \left(\frac{2T_0}{1 + (\nu' - \nu)^2 (2\pi T_0)^2} \right) d\nu' \\ &= \frac{c^2}{4\sqrt{2}\pi^{3/2} n_1^2 \tau \nu^2} \left(\frac{2 m_e m_{\text{hh}}}{\hbar (m_e + m_{\text{hh}})} \right)^{3/2} \\ &\quad \times \left(\nu - \frac{E_g}{h} \right)^{1/2} \times \left(f_c(\nu) - f_v(\nu) \right), \end{aligned} \tag{1}$$

where c is the velocity of light in vacuum, ν is the optical frequency, n_1 is the active region refractive index, τ is the radiative carrier recombination lifetime, $\hbar$ is the normalized Planck constant, m_e is the effective mass of an electron in conduction band (CB), m_{hh} is the effective mass of a heavy hole in valence band (VB), E_g is the band gap energy of the material, T_0 is the mean lifetime for the coherent interaction of electrons with a monochromatic field, and f_c and f_v are the Fermi-Dirac distributions for the conduction and valence bands, respectively.

The gain coefficient can be divided into two parts: stimulated emission rate R_e and stimulated absorption rate R_a,

$$g_m(\nu, n) = R_e(\nu, n) - R_a(\nu, n), \tag{2}$$

where

$$\begin{aligned} R_e(\nu, n) &= \frac{c^2}{4\sqrt{2}\pi^{3/2} n_1^2 \tau \nu^2} \left(\frac{2m_e m_{\mathrm{hh}}}{\hbar(m_e + m_{\mathrm{hh}})} \right)^{3/2} \\ &\quad \times \left(\nu - \frac{E_g}{h} \right)^{1/2} \times f_c(\nu)(1 - f_v(\nu)), \\ R_a(\nu, n) &= \frac{c^2}{4\sqrt{2}\pi^{3/2} n_1^2 \tau \nu^2} \left(\frac{2m_e m_{\mathrm{hh}}}{\hbar(m_e + m_{\mathrm{hh}})} \right)^{3/2} \\ &\quad \times \left(\nu - \frac{E_g}{h} \right)^{1/2} \times f_v(\nu)(1 - f_c(\nu)). \end{aligned} \tag{3}$$

The propagation of optical field in the SOA can be described as

$$\begin{aligned} \frac{dA_j^+}{dz} &= \left[-i\beta + \frac{1}{2}(\Gamma g_m(\nu, n) - \alpha) \right] A_j^+, \\ \frac{dA_j^-}{dz} &= \left[i\beta - \frac{1}{2}(\Gamma g_m(\nu, n) - \alpha) \right] A_j^-, \end{aligned} \tag{4}$$

where A_j^+ and A_j^- are the forward and backward travelling waves of the jth active region section, respectively, β is the propagation constant, Γ is the confinement factor, and α is the internal loss coefficient.

The propagation of the spontaneous emission field is presented as

$$\begin{aligned} \frac{dS_k^+}{dz} &= [\Gamma g_m(\nu_k, n) - \alpha] S_k^+ + R_{\mathrm{sp}}(\nu_k, n), \\ \frac{dS_k^-}{dz} &= -[\Gamma g_m(\nu_k, n) - \alpha] S_k^- - R_{\mathrm{sp}}(\nu_k, n). \end{aligned} \tag{5}$$

S_k^+ and S_k^- are the forward and backward amplified spontaneously emitted photon densities per unit frequency spacing centred at frequency ν_k. $R_{\mathrm{sp}}(\nu_k, n)$ is the ASE noise coupled into S_k^+ or S_k^-, and it is expressed as $R_{\mathrm{sp}}(\nu_k, n) = \Gamma R_e(\nu_k, n)\Delta\nu$, $\Delta\nu$ is frequency spacing.

The carrier rate equation is presented by

$$\begin{aligned} \frac{dn(Z)}{dt} &= \frac{I}{qV} - R(n(z)) - \sum_{j=1}^{n} \frac{\Gamma g_m(\nu, n)}{A_{\mathrm{cross}}} \left(A_j^+ + A_j^- \right) \\ &\quad - \sum_{k=1}^{m} \frac{2\Gamma g_m(\nu_k, n)}{A_{\mathrm{cross}}} \left(S_k^+ + S_k^- \right). \end{aligned} \tag{6}$$

The recombination rate term $R(n(z))$ is given by

$$R(n) = C_1 n + C_2 n^2 + C_3 n^3, \tag{7}$$

where C_1, C_2, and C_3 are the nonradiative recombination, bimolecular radiative recombination, and auger recombination coefficients, respectively.

The numerical model for the whole system of Figure 5 is achieved using iterative circulations. In the first iteration, the ASE in both directions of SOA2 is calculated assuming no ASE power is coupled in. Then the ASE generated by SOA2 travels in both clockwise and counterclockwise order towards SOA1. Under this boundary condition, the ASE originated from SOA2 together with the one generated by SOA1 is amplified by SOA1 as it travels through; however, only the backward ASE inside the SOA1 is input to SOA2. For any successive iterations, the ASE from SOA1 couples into SOA2 before SOA2 generates ASE. When ASE travels inside the ring cavity, the facet reflectivity and coupling loss of both SOAs, the insertion loss for the isolator, and WDM couples are taken into account. The round trip time is ~1.67 ns namely, the fibre length is about 0.5 m. Therefore, fibre loss and dispersion are neglected. The iterative procedure is terminated when the maximum difference of the ASE powers at each discrete frequency band between successive iterations is less than the desired tolerance. The numerical model is implemented using Matlab.

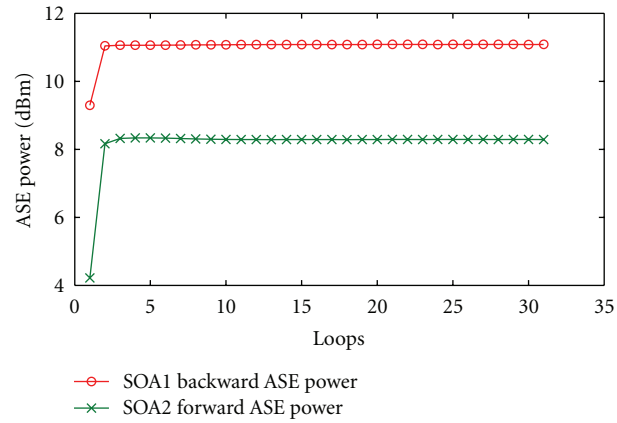

Figure 6: Counterclockwise ASE power after N loops. Cross: SOA2 output ASE power. Circle: SOA1 output ASE power.

4. Simulation Results and Discussions

The characteristics of AGC-SOA were studied from the initial state when no input signal is introduced. The ASE power after every counterclockwise ASE round trip is recorded. In Figure 6, the counterclockwise output ASE powers from SOA2 and SOA1 are displayed after each loop transit.

The ASE power increases rapidly within the first 3 loops and then stabilises. Since the cavity round trip time is ~1.7 ns, stabilising the travelling ASE power in the loop takes between 1.7 and 5.1 ns (several round trips). The ASE spectrum within the clamping mode was examined after every circulation. Figure 7 shows the SOA2 output ASE spectrum at different loop transits. In the first loop, the output ASE power from SOA2 is relatively low, and the whole spectrum is divided into two parts falling outside the C-band due to presence of the WDM coupler in the ring cavity.

Initially, the ASE power within the S-band is greater than that within the L-band. However, as the lasing mode becomes established, the output ASE power develops as predicted in Figure 6. With the ASE power within the S-band decreasing significantly, the spectrum becomes sharp and narrow.

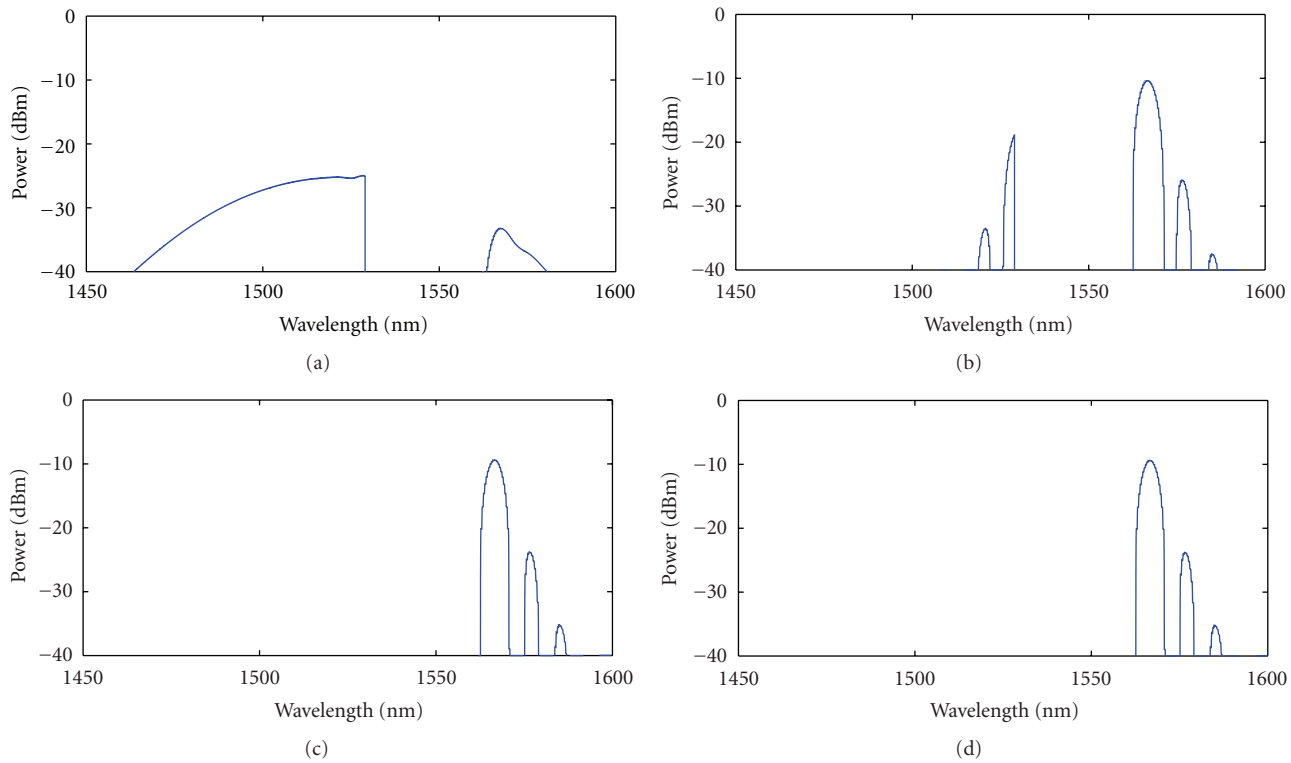

Figure 7: Modeled SOA2 ASE spectrum (counterclockwise). (a) Loop number = 1; (b) loop number = 10; (c) loop number = 20; (d) loop number = 100.

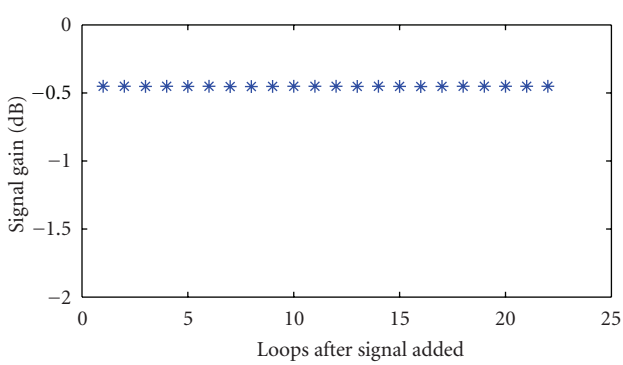

Figure 8: CW light (1550 nm, −20 dBm) gain as a function of circulating ASE loops after AGC-SOA stabilisation.

As ASE circulations progress, ASE emission in the S-band is further restrained becoming negligible, and ASE within the L-band accounts for gain clamping. This results from the fact that the lasing threshold is lower at longer wavelengths hence once lasing action is established, the shorter wavelength energy states are depleted. The results agree well with experimental observation.

Having established the steady-state conditions of model operation, an input optical signal was introduced after the ASE inside the AGC-SOA cavity stabilizes. The gain of 1550 nm CW light as a function of travelling ASE loop numbers is depicted in Figure 8. An optical signal power of −20 dBm was injected into SOA1. The drive current of SOA1 was set at 200 mA, and SOA2 at 65 mA. The simulation demonstrates that the signal gain settles within the first ASE loop transit and then remains unchanged; thus, after AGC-SOA stabilizes from the initial state (shown in the evolution depicted in Figure 7), it takes <2 ns (within one loop time) for the gain to settle.

The variation of the gain with clamping SOA drive current was modelled over a range of clamping currents to corroborate that the model faithfully reproduced the experimental behaviour of the AGC-SOA. The model outputs (Figure 9) indicate broadly that the model is predicting the trends. There is no significant loss of P_{sat} with gain reduction, however, the exact values of gain and P_{sat} differ slightly from experimental measurements. This difference most likely derives from small differences between the physical parameters used in the model and the real device.

The DC parametric operation of the AGC-SOA can be estimated using the above model. CW light (1550 nm) was introduced into AGC-SOA once the steady-state operation was established. The input signal power was then increased steadily from −35 dBm to 20 dBm, and the normal performance metrics of gain, maximum output power at gain saturation (P_{sat}), and noise figure (NF) were recorded for a given clamping current condition; the clamping current is changed from 0 mA to 200 mA. The simulation results are presented as a function of clamping current in Figure 10. The overall trends given by the models are in good agreement with previously reported experimental characterizations [6]. Gain clamping begins at a clamping bias current of greater than

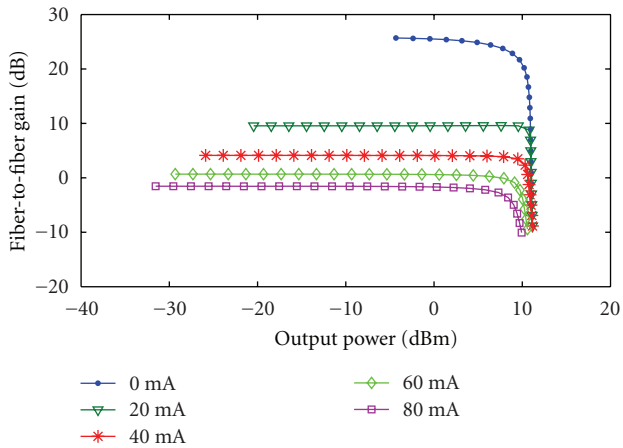

Figure 9: AGC-SOA gain as a function of output power at different clamping currents (modeling result).

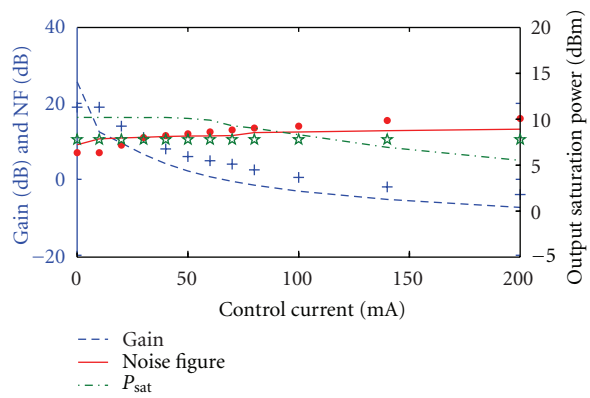

Figure 10: Experimental [6] and theoretical steady-state AGC-SOA performance comparisons. Red line: simulation results of NF. Red dot: experimental results of NF. Blue line: simulation results of gain. Blue cross: experimental results of gain. Green line: simulation results of P_{sat}. Green star: experimental results of P_{sat}.

0 mA. Experimentally this value was observed to be nearer 10 mA before there was sufficient gain within the clamping SOA to overcome loop losses and allow the lasing mode to stabilize. This difference is mainly due to the overestimation of ASE noise within the model [8]. Strong clamping is observed when the control SOA is operated at high gain levels; here, the AGC-SOA is driven into attenuation. As the gain is clamped, the NF increases, but in the main, the P_{sat} value remains relatively constant when the clamping current is <100 mA.

The theoretical model could also be used to better understand the dynamic behaviour of the AGC-SOA. In order to do this, the model was run under the following conditions. Firstly, stable operation of the AGC-SOA was ensured by running the simulation with only ASE for the first 30 loop iterations and at an SOA2 (clamping SOA) bias of 20 mA. At this point, a 0 dBm input signal was introduced, and it can be seen that the gain of the AGC-SOA is around 10 dB. The clamping SOA bias current was then increased every 10

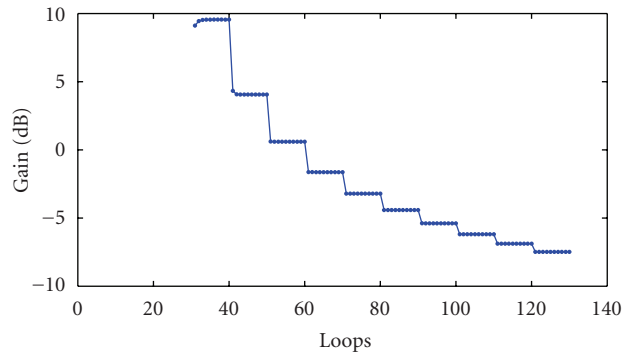

Figure 11: Dynamic gain variation as a function of clamping current.

loops, from 20 mA to 200 mA, in steps of 20 mA and the gain change observed (Figure 11). It is clear from these simulations that the gain is indeed adjusted and stabilized within 1 or 2 loops of the model iteration. This implies therefore that the gain can be adjusted within nanosecond timescales which agree with experimental results [7].

5. Conclusion

A detailed wideband model for adjustable gain-clamped semiconductor optical amplifier (AGC-SOA) has been established, which can be used to analyse steady-state and dynamic gain modulation performance of the device. The simulations agree with the experimental results, showing the advantage of AGC-SOA not only lies in extended linear amplification regime and adjustable device gains, but also the ability of adjusting and stabilising its gain within nanosecond timescales. This feature could enable the device to work as power equalizer and linear amplifier in packet-based dynamic systems such as passive optical networks (PONs).

Acknowledgments

Strathclyde University gratefully acknowledges funds received from the British Council under the Prime Ministers Initiative II, Research Cooperation. This work was also supported in part by the Glasgow Research Partnership in Engineering (GRPe).

References

[1] L. Banchi, M. Presi, A. D'Errico, G. Contestabile, and E. Ciaramella, "All-optical wavelength 10 and 40 Gbit/s RZ-to-NRZ format and wavelength conversion using semiconductor optical amplifiers," *Journal of Lightwave Technology*, vol. 28, no. 1, pp. 32–38, 2010.

[2] A. Rostami, H. B. A. Nejad, R. M. Qartavol, and H. R. Saghai, "Tb/s optical logic gates based on quantum-dot semiconductor optical amplifiers," *IEEE Journal of Quantum Electronics*, vol. 46, no. 3, pp. 354–360, 2010.

[3] C. Bohémond, A. Sharaiha, T. Rampone, and H. Khaleghi, "Electro-optical radiofrequency mixer based on semiconductor optical amplifier," *Electronics Letters*, vol. 47, no. 5, pp. 331–333, 2011.

[4] P. Doussiere, F. Pommereau, J. Y. Emery et al., "1550 nm polarization independent DBR gain clamped SOA with high dynamic input power range," in *Proceedings of the 22nd European Conference on Optical Communication (ECOC '96)*, vol. 3, pp. 169–172, September 1996.

[5] D. A. Francis, S. P. DiJaili, and J. D. Walker, "A single-chip linear optical amplifier," in *Proceedings of the Optical Fiber Communication Conference*, pp. PD13/1–PD13/3, Anaheim, Calif, USA, March 2001.

[6] C. Michie, A. E. Kelly, I. Armstrong, I. Andonovic, and C. Tombling, "An adjustable gain-clamped semiconductor optical amplifier (AGC-SOA)," *Journal of Lightwave Technology*, vol. 25, no. 6, pp. 1466–1473, 2007.

[7] L. Liu, C. Michie, A. E. Kelly, and I. Andonovic, "Packet equalisation in PONs using adjustable gain-clamped semiconductor optical amplifiers (AGC-SOA)," in *Proceedings of the International Conference on Transparent Optical Networks (ICTON '11)*, pp. 1–4, Stockholm, Sweden, June 2011.

[8] M. J. Connelly, "Wideband semiconductor optical amplifier steady-state numerical model," *IEEE Journal of Quantum Electronics*, vol. 37, no. 3, pp. 439–447, 2001.

[9] ITU-T Recommendation G.987.2, "10-Gigabit-capable passive optical networks (XG-PON): physical media dependent (PMD) layer specification," January 2010.

[10] X. H. Jia, "Theoretical investigation of gain-clamped semiconductor optical amplifiers using the amplified spontaneous emission compensating effect," *Journal of the Optical Society of America B*, vol. 23, no. 12, pp. 2503–2510, 2006.

[11] A. Matsumoto, K. Nishimura, K. Utaka, and M. Usami, "Operational design on high-speed semiconductor optical amplifier with assist light for application to wavelength converters using cross-phase modulation," *IEEE Journal of Quantum Electronics*, vol. 42, no. 3, Article ID 01597418, pp. 313–323, 2006.

[12] C. Y. Jin, Y. Z. Huang, L. J. Yu, and S. L. Deng, "Detailed model and investigation of gain saturation and carrier spatial hole burning for a semiconductor optical amplifier with gain clamping by a vertical laser field," *IEEE Journal of Quantum Electronics*, vol. 40, no. 5, pp. 513–518, 2004.

[13] S. Verspurten, G. Morthier, and R. Baets, "Experimental and numerical small-signal analysis of two types of gain-clamped semiconductor optical amplifiers," *IEEE Journal of Quantum Electronics*, vol. 42, no. 3, Article ID 01597417, pp. 302–312, 2006.

[14] S. L. Chuang, *Physics of Optoelectronic Devices*, Wiley-Interscience, New York, NY, USA, 1995.

[15] M. J. Connelly, "Wide-band steady-state numerical model and parameter extraction of a tensile-strained bulk semiconductor optical amplifier," *IEEE Journal of Quantum Electronics*, vol. 43, no. 1, pp. 47–56, 2007.

[16] A. Yariv, *Optical Electronics in Modern Communications*, Oxford University Press, New York, NY, USA, 5th edition, 1997.

Hindawi Publishing Corporation
International Journal of Optics
Volume 2012, Article ID 354156, 17 pages
doi:10.1155/2012/354156

Review Article

High-Energy Passive Mode-Locking of Fiber Lasers

Edwin Ding,[1] William H. Renninger,[2] Frank W. Wise,[2] Philippe Grelu,[3] Eli Shlizerman,[4] and J. Nathan Kutz[4]

[1] *Department of Mathematics and Physics, Azusa Pacific University, P.O. Box 7000, Azusa, CA 91702-7000, USA*
[2] *Department of Applied Physics, Cornell University, Ithaca, NY 14853, USA*
[3] *Laboratoire Interdisciplinaire Carnot de Bourgogne, UMR 5209 CNRS, Université de Bourgogne, 21000 Dijon, France*
[4] *Department of Applied Mathematics, University of Washington, Box 352420, Seattle, WA 98195-2420, USA*

Correspondence should be addressed to Edwin Ding, eding@apu.edu

Received 1 October 2011; Accepted 18 January 2012

Academic Editor: Francesco Prudenzano

Mode-locking refers to the generation of ultrashort optical pulses in laser systems. A comprehensive study of achieving high-energy pulses in a ring cavity fiber laser that is passively mode-locked by a series of waveplates and a polarizer is presented in this paper. Specifically, it is shown that the multipulsing instability can be circumvented in favor of bifurcating to higher-energy single pulses by appropriately adjusting the group velocity dispersion in the fiber and the waveplate/polarizer settings in the saturable absorber. The findings may be used as practical guidelines for designing high-power lasers since the theoretical model relates directly to the experimental settings.

1. Introduction

The invention of the laser by Maiman in 1960 is a historical landmark of advanced scientific innovation. Lasers serve as lightwave sources for pulsed electromagnetic energy and have a large variety of applications, ranging from small-scale problems such as ocular surgeries and biological imaging to large-scale problems such as optical communication systems and nuclear fusion. In the context of telecommunications and broadband sources, the laser is required to robustly produce optical pulses on the scale of picoseconds or even femtoseconds. The generation of such short pulses is often referred to as *mode-locking*. Depending on the design of the laser cavity, mode-locking can be classified as either active or passive. The active mode-locking mechanism uses an external signal to induce a modulation on the propagating electromagnetic field inside the laser cavity, whereas the passive mode-locking mechanism relies on placing some discrete element(s) into the laser cavity which causes self-amplitude modulation of the field. This paper discusses some of the latest theoretical developments in high-power passive mode-locked lasers.

A common feature to all mode-locked lasers is the intensity discrimination that is achieved by the mode-locking mechanism [1–3]. Such intensity discrimination, also known as saturable absorption, is the underlying mechanism responsible for passive mode-locking [4]. Figure 1 shows a typical passively mode-locked fiber laser that utilizes a ring configuration [1, 5, 6]. The laser cavity consists a piece of single-mode fiber (SMF), an output coupler that extracts the signal out of the cavity after each round trip, and a bandwidth-limited energy pump that compensates the energy lost during propagation. The saturable absorber considered here consists of a linear polarizer and a series of waveplates. When combined with the laser cavity polarization rotation, bandwidth-limited saturating gain, chromatic dispersion, and self-phase modulation, a uniform train of stable mode-locked pulses may be formed from white noise after a certain number of round trips. Saturable absorption can also be achieved by a variety of other physical mechanisms including nonlinear polarization rotation [7–10], nonlinear interferometry [11–14], graphene-based lattices [15, 16], and nonlinear mode-coupling [17–20], but the primary focus in this paper is the saturable absorption achieved by the polarizer and waveplates.

Since its first proposed use in the early 90s, the fiber ring cavity laser mode-locked by a passive polarizer and a series of

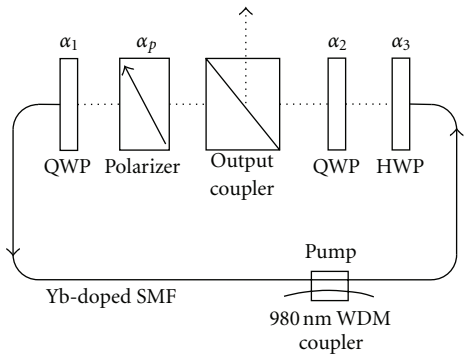

Figure 1: Experimental configuration of a ring laser cavity that includes quarter-waveplates (QWP), passive polarizer, half-waveplate (HWP), ytterbium-doped amplification, and output coupler. The Yb-doped section of the fiber is fused with standard single-mode fiber and treated in a distributed fashion. The angles α_1, α_2, α_3, and α_p of the discrete mode-locking elements can all be measured with reasonable accuracy. The dotted lines denote free space (from [6]).

quarter- and half-waveplates (see Figure 1) has become one of the most reliable and compact sources for robust ultrashort optical pulses [1, 3, 7–9]. Such fiber lasers offer major practical advantages over solid-state configurations. For example, they are relatively cheap and compact and do not require careful alignment of the optical cavity since the light is contained in a waveguide. The possibility of using fibers in short-pulse laser devices has motivated research for nearly two decades. However, limitations in the energy output have limited their impact in comparison to their solid-state counterparts. Indeed, fiber lasers have lagged well behind solid-state lasers in the key performance parameters—pulse energy and duration. Recently, new insights into pulse-propagation physics [21–23] have provided glimpses of order-of-magnitude increases in the pulse energy and peak power in femtosecond fiber lasers. However, the design and optimization of high-performance fiber devices is impeded by the so-called *multipulsing instability* (MPI), which ultimately imposes a fundamental limitation on a single mode-locked pulse energy [5, 24].

To compete directly with solid-state technologies, it is critical to understand the limiting effects of the MPI. A number of theoretical and computational models have been introduced over the past two decades in an attempt to quantify the mode-locking dynamics in a laser cavity with a passive polarizer. The master mode-locking equation first proposed by Haus [1] is the most well-known and recognized model to date. This model, later augmented by a quintic nonlinearity to account for the experimentally observed robust nature of the mode-locked pulses [3, 6, 25], is also known as the cubic-quintic Ginzburg-Landau equation (CQGLE). In this model, the discrete laser dynamics are averaged out and replaced by a truncated Taylor expansion addressing the Kerr nonlinearity and saturable absorption. Although the CQGLE gives good qualitative descriptions of the averaged mode-locking dynamics that are consistent with experiments [5, 6] and allows for extensive theoretical and numerical analysis [26–28], it is shown that the model fails to capture the potential high-energy pulses that are practically important to the community [29].

This paper gives an overview of the theoretical models that are used to describe the pulse propagation in the laser cavity [1, 3]. The primary focus is to exploit the system parameters with the aim of circumventing the MPI in favor of bifurcating to high-energy single-pulse solutions of the mode-locking models. The analysis and numerical simulations presented here provide mathematical insights into the underlying mode-locking dynamics and, more importantly, guidelines for experimentalists to optimize the performance in the mode-locked laser.

2. Governing Equations

As with all other electromagnetic phenomena, the propagation of the electric field in the laser cavity shown in Figure 1 is governed by Maxwell's equations. A multiscale asymptotic expansion of the solution to Maxwell's equation can be performed to separate the slowly varying envelope from the transverse dependence of the electric field [30, 31]. To describe the propagation of the electric field envelope, the dominant physical effects must be accounted for. These include chromatic dispersion, fiber birefringence, Kerr nonlinearity, cavity attenuation, bandwidth-limited saturable gain, and the discrete effects of the waveplates and polarizer. Under certain choice of the angles α_1, α_2, α_3, and α_p, the waveplates and the polarizer provide an effective intensity discrimination (saturable absorption) to shape the electric field circulating in the cavity [6, 25].

2.1. Full Governing Equations. The full governing equations for modeling the pulse evolution in the laser shown in Figure 1 can be divided into two parts: (i) the intra-cavity dynamics induced by the interactions of chromatic dispersion, Kerr nonlinearity gain saturation, and so forth and (ii) the discrete application of the waveplates and polarizer after each cavity round trip. It has been shown that the intracavity evolution is described by a pair of dimensionless coupled nonlinear Schrödinger equations (CNLS) [30–33]:

$$\begin{aligned} i\frac{\partial u}{\partial z} + \frac{D}{2}\frac{\partial^2 u}{\partial t^2} - Ku + \left(|u|^2 + A|v|^2\right)u + Bv^2u^* &= iR_u, \\ i\frac{\partial v}{\partial z} + \frac{D}{2}\frac{\partial^2 v}{\partial t^2} + Kv + \left(A|u|^2 + |v|^2\right)v + Bu^2v^* &= iR_v. \end{aligned} \tag{1}$$

In the above system, $u(z,t)$ and $v(z,t)$ represent the two orthogonally polarized electric field envelopes in an optical fiber with birefringence K and are usually referred to as the fast and slow components of the electric field, respectively. The z coordinate denotes the propagating distance normalized by the length of the cavity, and t denotes the retarded time normalized by the full width at half-maximum of the pulse. D is the averaged group velocity dispersion of the cavity and is positive for anomalous dispersion and negative for normal dispersion. The material properties of the optical fiber determine the values of the nonlinear coupling parameters A

(cross-phase modulations) and B (four-wave mixing). These parameters satisfy $A + B = 1$ by axisymmetry and, for the silica fiber considered, take on the specific values $A = 2/3$ and $B = 1/3$ [32, 33]. The dissipative terms R_u and R_v, accounting for the saturable, bandwidth-limited gain (from the Yb-doped amplification) and attenuation, take the form

$$R_\sigma = G(z)(1 + \tau\partial_t^2)\sigma - \Gamma\sigma, \tag{2}$$

with

$$G(z) = \frac{2g_0}{1 + (1/e_0)\int_{-\infty}^{\infty}\left(|u|^2 + |v|^2\right)dt}. \tag{3}$$

Here, g_0 and e_0 are the nondimensional pumping strength and the saturating energy of the gain medium, respectively. The parameter τ characterizes the bandwidth of the pump, and Γ measures the distributed losses caused by the output coupling and the fiber attenuation.

The discrete effect of the waveplates and passive polarizer after each cavity round trip can be modeled by the corresponding Jones matrices [5, 6]. The standard Jones matrices for the quarter-waveplate, half-waveplate, and polarizer are given, respectively, by

$$W_{\lambda/4} = \begin{pmatrix} e^{-i\pi/4} & 0 \\ 0 & e^{i\pi/4} \end{pmatrix}, \quad W_{\lambda/2} = \begin{pmatrix} -i & 0 \\ 0 & i \end{pmatrix}, \quad W_p = \begin{pmatrix} 1 & 0 \\ 0 & 0 \end{pmatrix}. \tag{4}$$

These matrices are valid only when the principal axes of the devices are aligned with the fast field of the cavity. For arbitrary orientation α_j ($j = 1, 2, 3, p$) shown in Figure 1, the matrices are modified according to

$$J_j = R\left(\alpha_j\right) W R\left(-\alpha_j\right), \tag{5}$$

where W is the Jones matrix of the device given in (4) and R is the rotation matrix

$$R\left(\alpha_j\right) = \begin{pmatrix} \cos\alpha_j & -\sin\alpha_j \\ \sin\alpha_j & \cos\alpha_j \end{pmatrix}. \tag{6}$$

The field $(u, v)^+$ immediately after any mode-locking element J_j can be related back to the field $(u, v)^-$ immediately before the element by

$$\begin{pmatrix} u \\ v \end{pmatrix}^+ = J_j \begin{pmatrix} u \\ v \end{pmatrix}^-. \tag{7}$$

To help make clear the modeling of the laser cavity dynamics subject to (1)–(6), consider a single round trip passage through the cavity. The propagation of the field starts immediately after the polarizer with orientation α_p for which the pulse is linearly polarized. The quarter-waveplate (with angle α_1) to the left of the polarizer converts the polarization state from linear to elliptical, thus creating a polarization ellipse. The two polarization components u and v then propagate through the fiber as governed by (1). At the end of the fiber, the half-waveplate (with angle α_3) further rotates the polarization ellipse through a certain angle. The quarter-waveplate (with angle α_2) converts the polarization state from elliptical back to linear, and the polarizer finally aligns the field with its own principal axis.

The CNLS (1) together with Jones matrices (5) gives a full description of pulse propagation in the laser system. We first apply a fast Fourier transform to convert the temporal domain of the CNLS to the spectral domain. An adaptive step-size fourth-order Runge-Kutta algorithm is then used to propagate the initial data (in the spectral domain) over one cavity round trip. The Jones matrices of the waveplates and polarizer are then applied to the end data sequentially, and the entire procedure is repeated. The discrete application of Jones matrices after each cavity round trip acts like a filter that can be tuned to control the mode-locking behavior. Depending on their orientations, the waveplates and the polarizer can either destabilize the field propagating in the cavity or provide an effective intensity discriminating mechanism to lock it into a robust pulse. Figure 2 shows how stable, self-starting mode-locking can be achieved in the laser cavity shown in Figure 1. At a pumping strength $g_0 = 1$ (Figures 2(a) and 2(b)), the initial white noise is mode-locked into a stable pulse after about two hundred cavity round trips. When the pumping strength is increased to $g_0 = 2.7$ (Figures 2(c) and 2(d)), stable single-pulse mode-locking cannot be achieved. Specifically, the increased pumping strength broadens the frequency spectrum of the pulse, which eventually exceeds the bandwidth of the pump. In this case the initial white noise quickly evolves into the next energetically favorable state of two identical pulses. The bifurcation of a single pulse into multiple pulses (multipulsing instability (MPI)) is the main focus of this paper.

2.2. The Master Mode-Locking Equation. Although it is not difficult to simulate the full governing system (1)–(5) [21, 23, 26, 34–38], extracting analytic results remains a mathematical challenge due to the discrete nature of the implementation of the waveplates and polarizer. This has led to the consideration of averaged evolution models that distribute all the lumped effects over the entire cavity while retaining the key mode-locking dynamics [39, 40]. The master mode-locking equation proposed by Haus [1, 7–9] was the first theoretical model used to describe the mode-locking dynamics in the ring cavity laser shown in Figure 1. This model is essentially the complex Ginzburg-Landau equation (CGLE) where a cubic nonlinearity is used to describe the action of the saturable absorber. A quintic term is usually added to the master mode-locking equation to account for the robustness of the pulses observed in experiments, and the resulting equation, generally known as the cubic-quintic Ginzburg-Landau equation (CQGLE), takes the form

$$\begin{aligned} i\psi_z + \frac{D}{2}\psi_{tt} + \gamma|\psi|^2\psi + \nu|\psi|^4\psi \\ = ig(z)(1 + \tau\partial_t^2)\psi - i\delta\psi + i\beta|\psi|^2\psi + i\mu|\psi|^4\psi. \end{aligned} \tag{8}$$

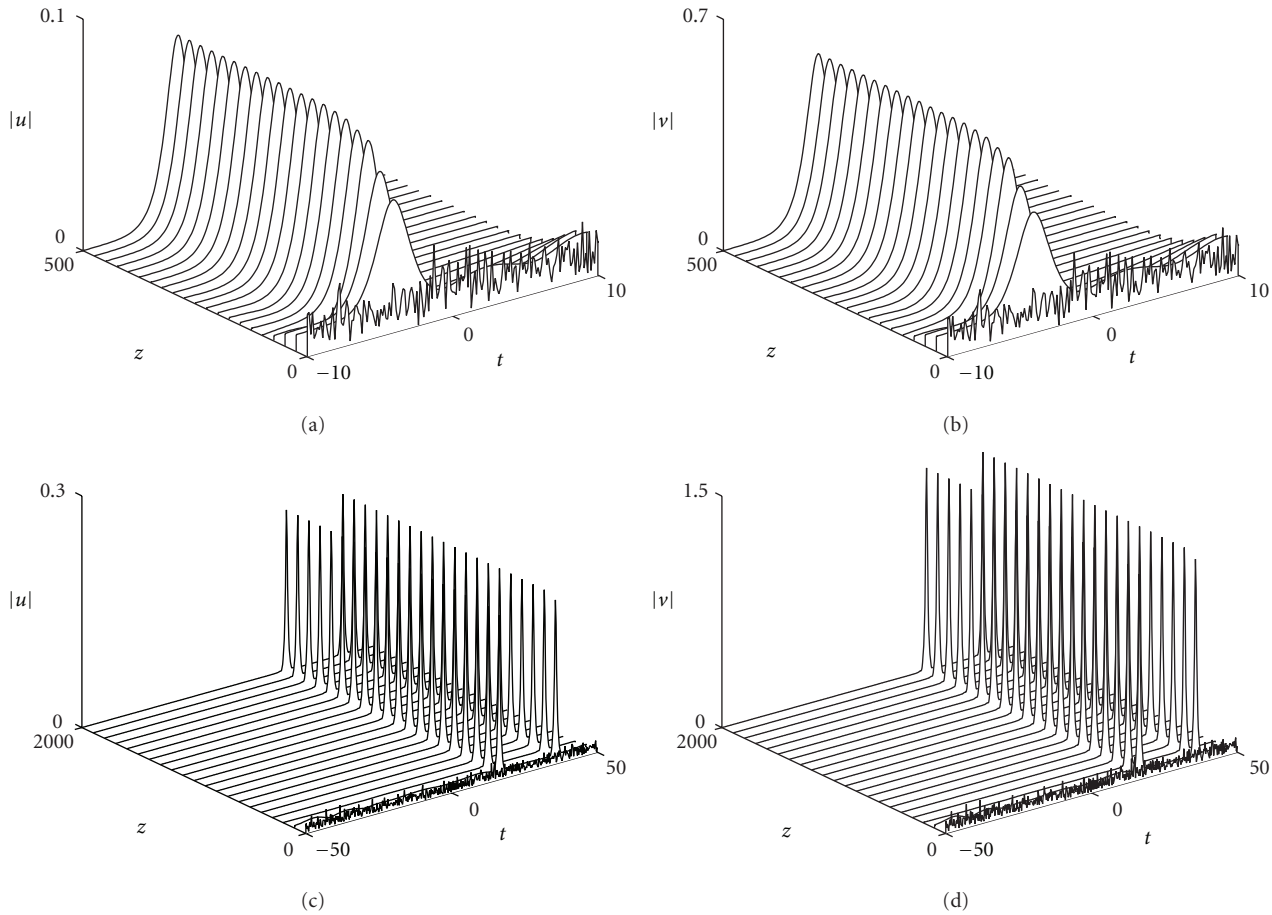

Figure 2: Self-starting mode-locking from white noise. (a) and (b) Stable single-pulse mode-locking when $g_0 = 1$. (c) and (d) Stable double-pulse mode-locking when $g_0 = 2.7$. The rest of the parameters are $D = 0.4$, $K = 0.1$, $e_0 = 1$, $\tau = 0.1$, $\Gamma = 0.1$, $\alpha_1 = 0$, $\alpha_2 = 0.82\pi$, $\alpha_3 = 0.1\pi$, and $\alpha_p = 0.45\pi$.

Here, ψ represents the overall envelope of the electric field and the saturating gain is

$$g(z) = \frac{2g_0}{1 + (1/e_0)\int_{-\infty}^{\infty} |\psi|^2 dt}. \tag{9}$$

The derivation of the CQGLE that relates the coefficients to the experimental setup in Figure 1 was first given by Komarov et al. [5, 25]. In the derivation they assumed that the orientations of the two quarter-waveplates add up to zero ($\alpha_1 + \alpha_2 = 0$) and that the field is polarized along the fast component, that is, $\alpha_p = 0$. Here, we will use a more general approach that can be found in [6, 29].

The key idea in deriving the CQGLE is to separate the linear and nonlinear effects in the CNLS (1), assuming that these effects occur on a length scale much longer than the fiber length [5, 6, 25, 29]. We follow the circulating electric field in the laser cavity coming out from the polarizer. Ignoring the birefringence K (which will be treated separately), the linear terms in (1) alone yield the evolution equation

$$i\psi_z + \frac{D}{2}\psi_{tt} = ig(z)(1 + \tau\partial_t^2)\psi - i\Gamma\psi. \tag{10}$$

The field envelope ψ is related to the two orthogonally polarized components in the CNLS through the transformation $u = \psi\cos\alpha_p$ and $v = \psi\sin\alpha_p$, where α_p is the orientation of the polarizer. On the other hand, the nonlinear evolution

$$\begin{aligned} i\frac{\partial u}{\partial z} + \left(|u|^2 + A|v|^2\right)u + Bv^2u^* &= 0, \\ i\frac{\partial v}{\partial z} + \left(A|u|^2 + |v|^2\right)v + Bu^2v^* &= 0 \end{aligned} \tag{11}$$

can be solved analytically to get

$$\begin{pmatrix} u^- \\ v^- \end{pmatrix} = e^{iI_n}J_{\mathrm{NL}}\begin{pmatrix} u_n \\ v_n \end{pmatrix} = e^{iI_n}\begin{pmatrix} \cos w & \sin w \\ -\sin w & \cos w \end{pmatrix}\begin{pmatrix} u_n \\ v_n \end{pmatrix}, \tag{12}$$

where $I_n = |u_n|^2 + |v_n|^2$ is the total power of the field at the beginning of the fiber section during the nth round-trip and $w = BI_n \sin 2(\alpha_1 - \alpha_p)$. The above map shows that the field undergoes an intensity-dependent polarization rotation (governed by J_{NL}) as it propagates along the fiber. The effect of the fiber birefringence K alone is

$$i\frac{\partial u}{\partial z} - Ku = 0, \quad i\frac{\partial v}{\partial z} + Kv = 0, \tag{13}$$

which leads to $u(z,t) = u(0,t)\exp(-iKz)$ and $v(z,t) = v(0,t)\exp(iKz)$, respectively. In other words, the birefringence induces a $2K$-phase shift between the two polarization components at the end of the fiber segment, that is, at $z = 1$. Therefore, we approximate the birefringence using the matrix

$$J_K = \begin{pmatrix} e^{-iK} & 0 \\ 0 & e^{iK} \end{pmatrix}. \tag{14}$$

Applying this birefringent matrix and the Jones matrices given in (5) to (12) results in the scalar map

$$\begin{aligned} \psi_{n+1} &= e^{i|\psi_n|^2} Q(I_n)\psi_n, \\ &= e^{i|\psi_n|^2 + \log Q}\psi_n, \end{aligned} \tag{15}$$

where the complex function Q is given by

$$\begin{aligned} Q = \frac{1}{2}\Big\{ & e^{-iK}\Big[\cos\big(2\alpha_2 - 2\alpha_3 - \alpha_p\big) + i\cos\big(2\alpha_3 - \alpha_p\big)\Big] \\ & \times \Big[i\cos\big(2\alpha_1 - \alpha_p - w\big) - \cos\big(\alpha_p - w\big)\Big] \\ & + e^{iK}\Big[\sin\big(2\alpha_2 - 2\alpha_3 - \alpha_p\big) - i\sin\big(2\alpha_3 - \alpha_p\big)\Big] \\ & \times \Big[\sin\big(\alpha_p - w\big) - i\sin\big(2\alpha_1 - \alpha_p - w\big)\Big]\Big\}. \end{aligned} \tag{16}$$

This complex quantity is explicitly related to the birefringence as well as the settings of the waveplates and polarizer. Equations (10) and (15) are the leading order approximation to the pulse propagation in the laser cavity shown in Figure 1. The initial data is first evolved forward over one round trip according to the linear equation (10). The discrete, nonlinear map (15) is then applied to the resulting field and the process is repeated.

The effect of the nonlinear transfer function Q can be averaged into the evolution by taking a continuous limit of (15), yielding the differential equation [6]

$$\psi_z = \Big(i|\psi|^2 + \log Q\big(|\psi|^2\big)\Big)\psi. \tag{17}$$

The leading order approximation to the overall evolution is obtained by combining (10) and (17), that is,

$$i\psi_z + \frac{D}{2}\psi_{tt} + |\psi|^2\psi = ig(z)(1 + \tau\partial_t^2)\psi - i\Gamma\psi + i\log(Q)\psi. \tag{18}$$

We refer to this equation as the sinusoidal Ginzburg-Landau equation (SGLE) [29]. The coefficients in the CQGLE (8) can be related to the experimental settings by expanding the logarithmic term in the SGLE as power series in $|\psi|^2$ (assuming it is small) and truncating at the term $|\psi|^4$. Specifically, the CQGLE coefficients are calculated as

$$\begin{aligned} \delta &= \Gamma - \log|Q(0)|, \\ \gamma &= 1 + Im\,(Q'(0)/Q(0)), \\ \beta &= Re\,(Q'(0)/Q(0)), \\ \nu &= Im\,\Big[\big(Q(0)Q''(0) - Q'^2(0)\big)/Q^2(0)\Big]/2, \\ \mu &= Re\,\Big[\big(Q(0)Q''(0) - Q'^2(0)\big)/Q^2(0)\Big]/2, \end{aligned} \tag{19}$$

where the derivatives are taken with respect to $|\psi|^2$. In the case of the master mode-locking model (CGLE), the quintic coefficients ν and μ are set to zero. When the parameters are appropriately chosen, the CQGLE model supports solitary wave solutions that are known as *dissipative solitons* in the optics community [17]. It should be noted that in what follows the term soliton is used in a much broader sense than the strict mathematical definition of the localized solution of a completely integrable nonlinear evolution equation [41]. The form of the dissipative soliton is solely determined by the system parameters rather than by the initial condition as in the classical soliton theory.

In the CGLE, one has to adjust the orientations of the waveplates and polarizer in order that the cubic dissipation β is always positive so that self-amplitude modulation (intensity discrimination) is possible. There is, however, only a small range of β values that allows stable mode-locking to occur [42, 43]. Outside this range, the cubic gain is either too low for pulse formation or too large so that the pulse amplitude blows up to infinity after several cavity round trips. In reality, the pulse governed by the full equations (1) and (5) can never blow up since it always experiences a net loss upon passing through the mode-locking elements (waveplates and polarizer). The CQGLE prevents the pulse from blowing up by saturating the cubic gain with a quintic loss ($\mu < 0$). This is a better description of the saturable absorption process, which makes the CQGLE a physically more relevant model than the master mode-locking equation. In the regime where both the cubic and quintic dissipations are positive, there is no higher-order saturation in the model to prevent the blow-up of pulses, and thus the CQGLE becomes suspect as it admits a large number of unphysical behaviors. Therefore, the condition

$$\beta > 0 > \mu \tag{20}$$

is considered for the CQGLE to be a physically relevant model that does not exhibit blow-up. With an appropriate choice of parameters, the real part of the transfer function Q provides an effective intensity discriminating mechanism (saturable absorption) to shape the circulating field. In this process the saturable absorber sifts out those intensities whose polarization state is commensurate with the orientation of the waveplates and polarizer, thus forming a stable mode-locked pulse. Figure 3 shows the experimentally (Figure 3(a)) and numerically predicted (Figure 3(b)) operating regimes of the laser depicted in Figure 1. In

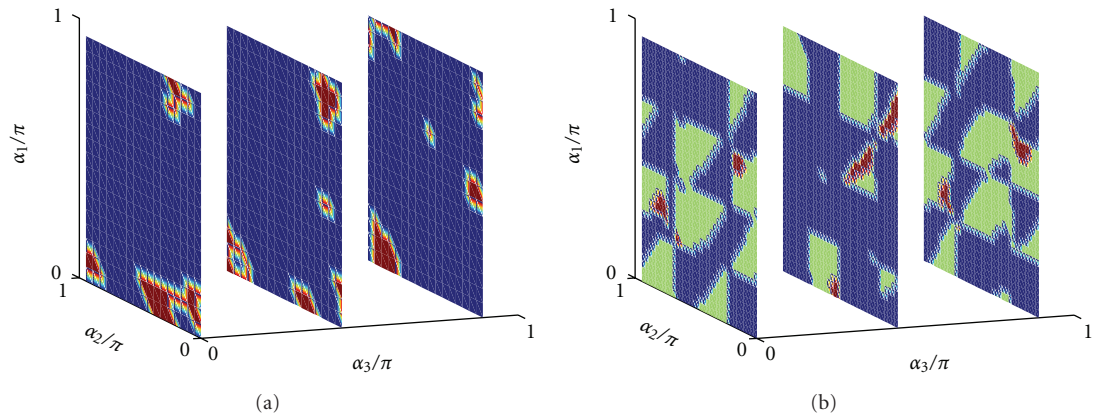

Figure 3: (a) Experimental operating regimes (red) of the laser shown in Figure 1. (b) Predicted operating regimes (red) of the CQGLE (8). The green region satisfies condition (20) but no stable pulses are found. Here $B = 1/3$, $K = 0.1$, $g_0 = \delta$, $D = -0.3$, $\tau = 0.2$, and $\alpha_p = 0.45\pi$ (from [6]).

the numerical result, mode-locking is only achievable in the red region. The green region satisfies condition (20), but stable mode-locked pulses cannot be found. This suggests that condition (20) alone is not sufficient to guarantee mode-locking. A quantitative comparison between experiment and theory is difficult as the birefringence K and the orientation of the fast axis of the fiber are hard to measure in practice. However, the theory reproduces the islands of stable regions, which are a key feature that is also observed in experiments.

3. Dissipative Soliton Resonance

When more energy is injected into the laser cavity, the mode-locked pulse splits into multiple pulses (see Figure 2) instead of becoming a more intense single pulse. When the full set of cavity parameters that includes chromatic dispersion is taken into account, it is possible to find a certain region in the laser cavity vast parameter space for which the mode-locked pulse becomes wider instead of splitting into multiple pulses as the cavity energy is increased. This specific method of using the cavity dispersion to circumvent MPI is referred to as dissipative soliton resonance (DSR) [44–46].

The CQGLE (8) is the standard theoretical model describing the averaged pulse dynamics in a ring cavity laser [1, 3, 5, 6, 37]. Previous studies on DSR were phenomenological while the parameters in the CQGLE were chosen randomly. Comparing to the previous works on DSR [45, 46], the results here present two important additional features that pave the way for experimental investigations [44]. First, the parameters in the governing model are explicitly related to the waveplate/polarizer angles through expressions (19), allowing for a connection between theory and experiment. Second, a saturable, instead of a constant, gain is studied. This provides a more physically realistic picture that takes into account the finite pumping power budget [1, 3].

Without loss of generality, the self-phase modulation γ in the CQGLE (8) can be normalized to one. Figure 4 shows the normalized cubic-quintic nonlinearities as functions of the quarter-waveplate angle α_1 while the other parameters are fixed. Mode-locking dynamics, and in particular DSR, will be explored in regions where $\beta > 0 > \mu$ (see condition (20)). Other regions are considered as physically irrelevant since either the pulse will experience a blow-up in amplitude, or there is a lack of intensity discrimination [6]. The saturating gain is considered here, namely,

$$g = \frac{2g_0}{1 + \|\psi\|^2/e_0}. \tag{21}$$

This is a more physically realizable model than the constant gain model since the pump cannot maintain a fixed gain at arbitrary high cavity energy. In fact, it has been shown that the pulse solution of the master mode-locking equation (CQGLE with $\nu = \mu = 0$) with constant gain is always unstable [27, 28, 42, 43].

In order to investigate the energy limiting effects of the saturable gain dynamics on the DSR, we use both D and the saturating energy e_0 as control parameters with the results summarized in Figure 5. Usually for a fixed dispersion, the mode-locked pulse will become unstable when e_0 is too large. Such an instability is usually characterized by a Hopf bifurcation and marks the onset of MPI [24]. The cavity dispersion D is the crucial factor in determining the dominant effect in the competition between DSR and MPI. Specifically, there is a critical limit $D = D_c$ such that the system favors DSR when $D < D_c$, and MPI when $D > D_c$. For the parameters considered in Figure 5, we found (numerically) that $D_c \approx -1.2$. Consider, for instance, the case where $D = -1.6 < D_c$. The Gaussian-looking pulse (blue solid curve) at low e_0 values first grows in amplitude until a saturating amplitude is reached (red dashed curve) and then in width to form a high-energy, flat-top structure (green dash-dot curve) at high e_0 values. The observed transformations in pulse shape and the chirp profile are signatures of the DSR although now infinite pulse energy cannot be achieved due to the finite saturation energy e_0. However, the physically unrealistic infinite pulse energy solutions of the constant gain DSR [45, 46] were key for motivating the present work with saturating, finite energy behavior. Remarkably, the onset of MPI is not observed even when the saturating energy is

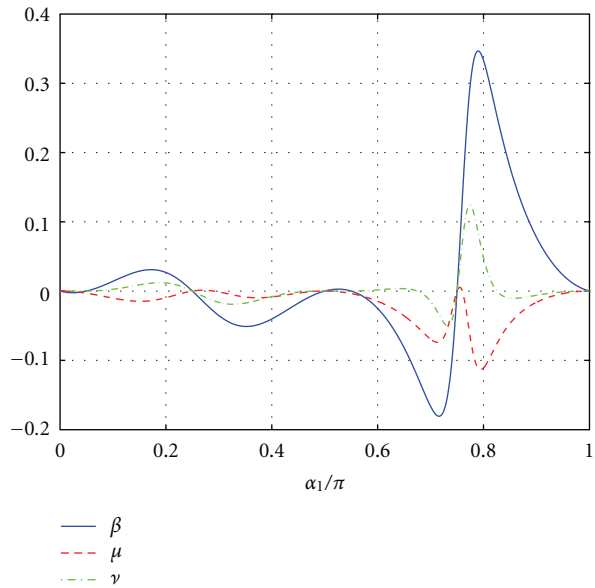

Figure 4: Normalized coefficients of the CQGLE as a function of α_1 at $\alpha_2 = 0.16\pi$, $\alpha_3 = 0.63\pi$, $\alpha_p = 0$, and $K = 0.1$ (from [44]).

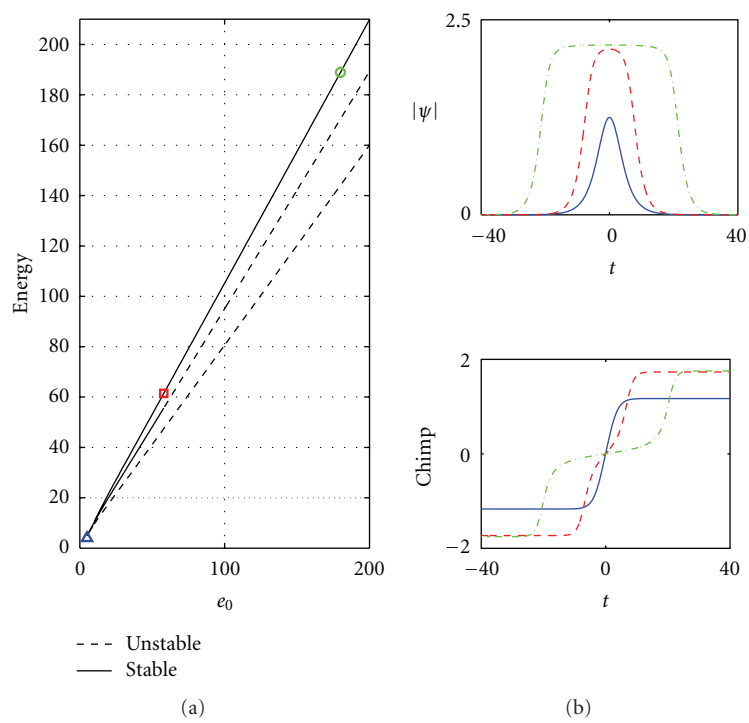

Figure 5: DSR in the case of saturating gain. (a) Pulse energy $\|\psi\|^2$ as a function of e_0 at $D = -1.6$ (top), $D = -1.2$ (middle), and $D = -0.8$ (bottom), respectively. The rest of the parameters are $g_0 = 2.3991$, $\tau = 0.1667$, $\alpha_1 = 0.7863\pi$, $\alpha_2 = 0.3\pi$, $\alpha_3 = \alpha_p = 0$, $K = 0.1$, and $\Gamma = 0.1$. (b) The corresponding pulse shape (top) and frequency chirp profile (bottom) at $e_0 = 5$ (blue solid curves), $e_0 = 58$ (red dashed curves), and $e_0 = 180$ (green dash-dot curves) along the $D = -1.6$ line, respectively (from [44]).

as large as $e_0 = 200$. On the other hand, the Gaussian-looking mode-locked pulse becomes unstable long before the formation of the high-energy, flat-top pulse when $D = -0.8 > D_c$. The simulations here show that DSR can be used as an effective mechanism to circumvent MPI, provided the dispersion D is appropriately chosen.

4. Periodic Transmission: The Sinusoidal Ginzburg-Landau Equation

It was shown in Section 2.2 that the CQGLE (8) can be obtained from the sinusoidal Ginzburg-Landau equation (18) by Taylor expanding the logarithmic term with $Q(|\psi|^2)$

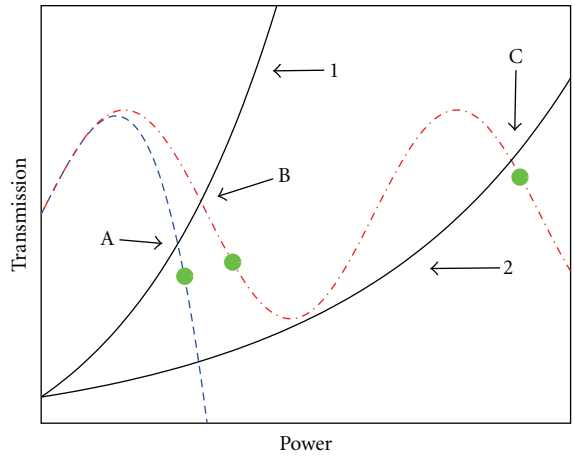

Figure 6: The red dash-dot line and the blue dashed line represent the transmission of the SGLE and the CQGLE, respectively. The black solid lines denote the saturating gain curves. The intersection of the gain and transmission curves represents a stable mode-locked pulse. The green circles are the maximum power allowed in the laser cavity. When energy is increased, gain curve 1 shifts towards gain curve 2, causing the mode-locked pulses A and B to exceed the maximum power allowed. In the CQGLE, the solution jumps to the next most energetically favorable configuration of a double-pulse solution (not shown). A high-energy single-pulse solution (point C) can exist in the SGLE model (from [29], 2011, IEEE).

being the periodic transmission produced by the saturable absorber (waveplates and polarizer). One has to choose the waveplate/polarizer settings such that the cubic-quintic coefficients satisfy condition (20) in order for the model to be physically relevant. Specifically, $\beta > 0$ provides an effective pulse shaping mechanism in the laser cavity and $\mu < 0$ saturates the cubic growth when the pulse amplitude becomes too large [3, 6]. Condition (20) is an artificial constraint that arises solely from mathematical considerations and is the byproduct of using a truncated Taylor series. However, a series representation of the transmission function can lead to the elimination of important high-energy solution branches since the fundamental periodic transmission function is destroyed by the finite truncation. This fact has motivated the incorporation of the full logarithmic term rather than using its Taylor series in the averaged model, that is, using the SGLE (18) as the governing equation in the laser cavity. We will show that this model is able to support high-energy pulses that are not captured by the CQGLE [29].

4.1. Principle of Operation. To illustrate the key idea of the SGLE model, consider the generic transmission curves shown in Figure 6, which summarizes the main findings in the recent work of Li et al. [24]. The red dash-dot line and the blue dashed line represent the typical transmission function of the SGLE and the CQGLE, respectively. The black solid lines, on the other hand, denote the saturating gain curves in the cavity [1, 24, 29, 47]. The intersection of the gain curve and the transmission curve describes a mode-locked solution where the cavity energy is in equilibrium. The points A and B along the gain curves represent the single mode-locked solution of the CQGLE and SGLE, respectively. When the saturation energy is increased, the power of the mode-locked pulse acquires a larger value which in turn shifts gain curve 1 towards gain curve 2 [24]. Eventually the power of the mode-locked solution exceeds the maximum value allowed (the green circles) in the laser system as computed from numerical simulations. In the case of CQGLE, the solution jumps to the next most energetically favorable configuration of a multipulse solution (not shown). For the SGLE, however, the solution is expressed as a stable single high-energy pulse at the point C, which is not captured by the CQGLE transmission.

The advantage of incorporating the full sinusoidal transmission in the mode-locking model is twofold. First, since the transmission is not approximated by series expressions, the SGLE is able to give a more accurate description of the underlying mode-locking dynamics. Second, as shown above, high-energy pulses are possible only when a full analysis of the sinusoidal transmission curve is used [24, 29]. Thus, the SGLE model can serve as a design tool to maximize the energy output by adjusting the orientations of the waveplates and polarizer. Although analytical results are nontrivial due to the complexity of the equation, the SGLE is relatively easy to analyze with efficient numerical algorithms and reduction techniques [48–50].

4.2. Comparison of the SGLE with Different Mode-Locking Models. In this section, we will first establish that the SGLE is a valid mode-locking model that exhibits the essential dynamics in the nonlinear polarization rotation laser. Then, we will show that it is able to reproduce the high-energy pulses of the full governing system, solutions which are precluded from the master mode-locking theory and the CQGLE model.

4.2.1. Stable Mode-Locking and Multipulsing. We first compare the mode-locking performance governed by the full lumped mode-locking system (1)–(6) (CNLS in conjunction with the Jones matrices) and the SGLE (18). Figure 7

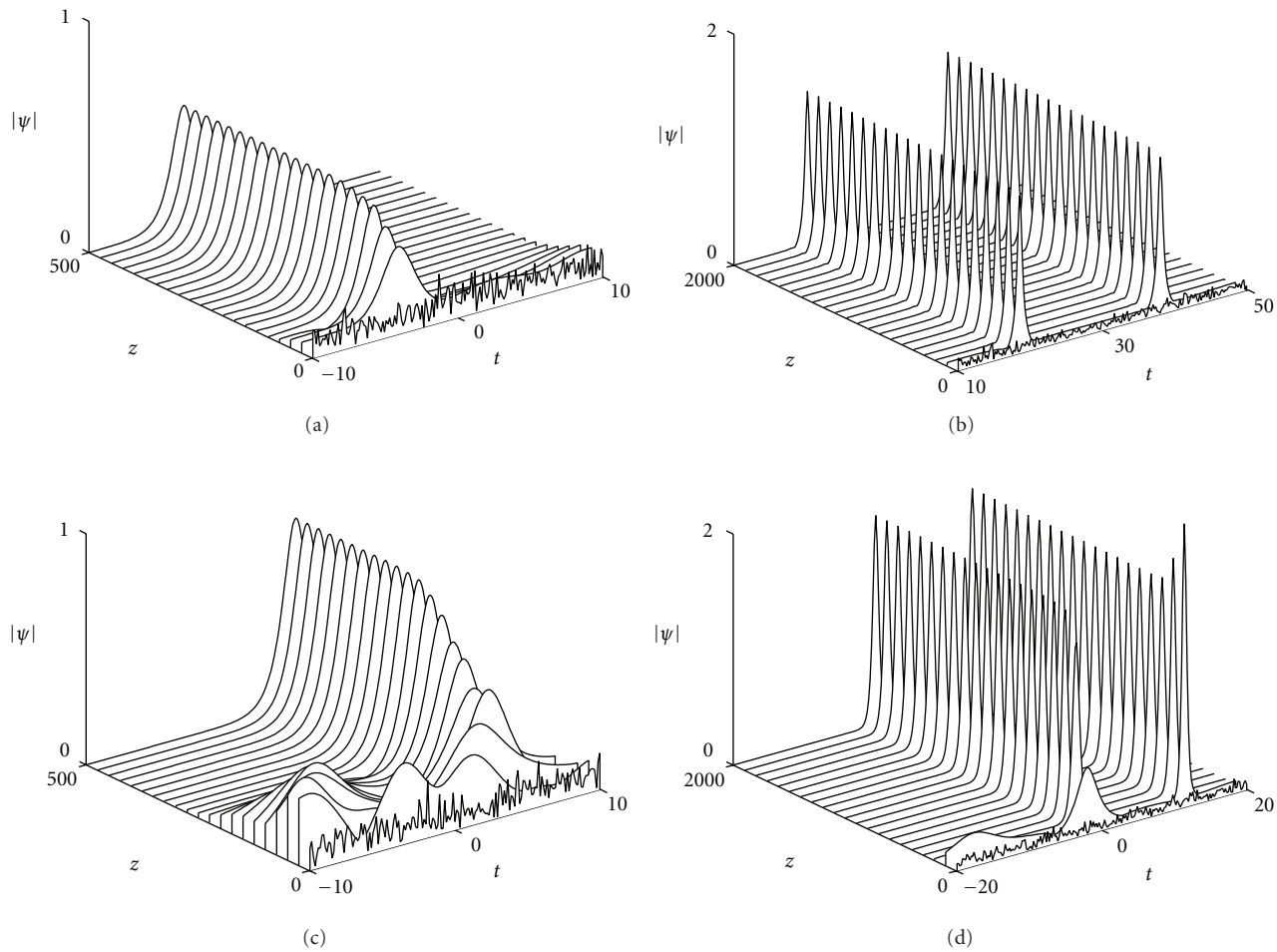

Figure 7: Numerical simulations of the full discrete governing system ((a) and (b), recall that $|\psi|^2 = |u|^2 + |v|^2$) and the SGLE ((c) and (d)) at different gain values g_0 in the anomalous dispersion regime. (a) and (c) Stable single-pulse evolution starting from white noise at $g_0 = 1$. (b) and (d) The initial white noise quickly evolves into two identical pulses per cavity round trip at $g_0 = 2.7$. The rest of the parameters in the simulations are $D = 0.4$, $\alpha_1 = 0$, $\alpha_2 = 0.82\pi$, $\alpha_3 = 0.1\pi$, $\alpha_p = 0.45\pi$, $K = 0.1$, $\Gamma = 0.1$, $e_0 = 1$, and $\tau = 0.1$(from [29], 2011, IEEE).

demonstrates the self-starting behavior of the laser from a white noise initial condition in the anomalous dispersion regime ($D > 0$) with a particular waveplate/polarizer setting. In Figures 7(a) and 7(c), the pumping strength is set at $g_0 = 1$, and the initial white noise is dynamically locked into a stable stationary pulse after several hundred cavity round trips in both the full system (Figures 7(a) and 7(b)) and the SGLE (Figures 7(c) and 7(d)). The temporal location at which the pulse forms is completely arbitrary since random initial data is used. When the energy injected into the system is increased by increasing the gain g_0, the laser undergoes the commonly observed MPI [24]. In this situation, the initial condition quickly evolves into two or more pulses with identical energies, depending on the strength of the gain. It can be seen that the SGLE is capable of capturing qualitatively the MPI that occurs in the full system (Figures 7(b) and 7(d)) at a high gain level (e.g., $g_0 = 2.7$).

Qualitative matching between the SGLE model and full evolution is also achieved in the normal dispersion regime ($D < 0$), as shown in Figure 8. For the parameters considered, a single mode-locked pulse can be formed in both the full governing equations and the SGLE at $g_0 = 1$ (Figures 8(a) and 8(c)). When the gain is increased to $g_0 = 3$, the laser cavity no longer supports a stable single-pulse solution and a double-pulse configuration is observed (Figures 8(b) and 8(d)). From Figures 7 and 8, one can see that the two main differences between the full dynamics and the SGLE dynamics are (i) the duration of the transient evolution and (ii) the mode-locked amplitude. In the case of anomalous dispersion, for instance, it takes approximately 300 and 350 cavity round trips for the full system and the SGLE to mode-lock into a stable pulse, respectively. The mode-locked peak amplitude is 0.52 for the full model and 0.81 for the SGLE. The discrepancy is intrinsic for the averaged evolution

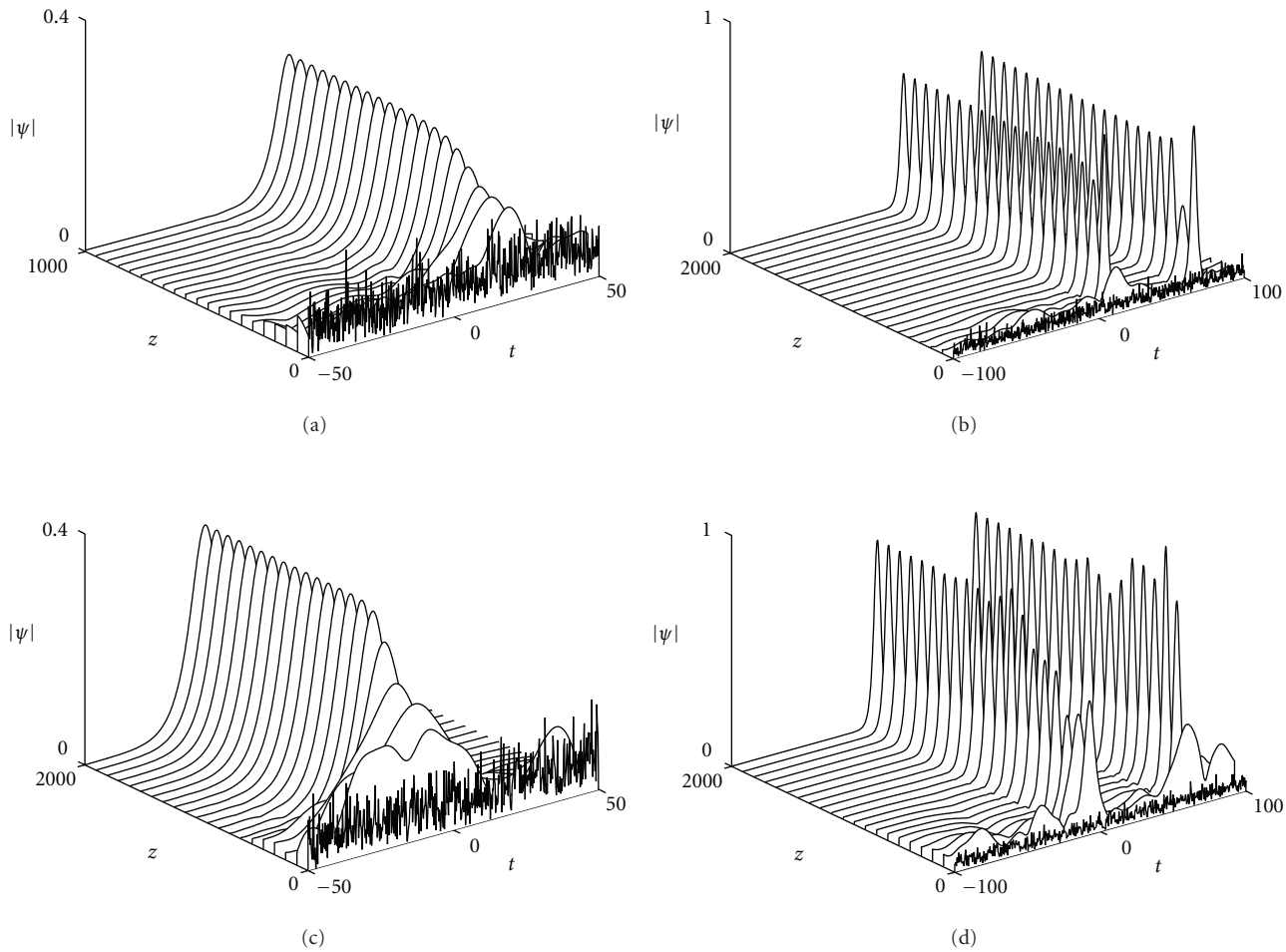

Figure 8: Numerical simulations of the full governing system ((a) and (b)) and the SGLE ((c) and (d)) at different gain values g_0 in the normal dispersion regime. (a) and (c) Stable single-pulse evolution starting from white noise at $g_0 = 1$. (b) and (d) The initial white noise evolves into two identical pulses per cavity round trip at $g_0 = 3$. The rest of the parameters in the simulations are $D = -0.4$, $\alpha_1 = 0.1\pi$, $\alpha_2 = 0.554\pi$, $\alpha_3 = 0.23\pi$, $\alpha_p = 0.43\pi$, $K = 0.1$, $\Gamma = 0.1$, $e_0 = 1$, and $\tau = 0.2$ (from [29], 2011, IEEE).

equations (including the CGLE and CQGLE). Nevertheless, this does not impact the usefulness of the SGLE model as it captures the self-starting nature of the laser and is easier to analyze than the full governing equations, that is, it is one scalar equation versus two coupled equations with discrete application of four Jones matrices.

4.2.2. Transition Dynamics. When the waveplate/polarizer angles α_1, α_2, α_3, and α_p are chosen appropriately such that mode-locking is achievable, the initial data can evolve into an arbitrary number of stable pulses depending on the pumping strength g_0. In general, the transition from an n-pulse solution to an $(n+1)$-pulse solution is not a discrete process. Various types of transition dynamics can be obtained by modifying the waveplate/polarizer settings as well as other system parameters, as confirmed by theory and experiments [24, 51, 52]. Usually these transitional states are difficult to capture as they often happen in a small parameter regime, and fine tuning of the parameters is required to visualize them. Figure 9 shows a typical transition state of the laser cavity in the anomalous dispersion regime ($D > 0$). The pumping strength g_0 is chosen to be between the stable single- and double-pulse operations shown in Figure 7. Note that the g_0 values used in the full and SGLE models are different as one cannot expect an averaged or approximated model to match the original model at the exact same parameter values. The transitional state contains a tall pulse at the origin and one short pulse on each side of it. These side pulses are developed from the background. The entire structure undergoes small amplitude oscillations (at the order of 10^{-4}). A remarkable agreement between the full governing equations (Figures 9(a) and 9(b)) and the SGLE mode (Figures 9(c) and 9(d)) is observed. This periodic state is stable and persists over long propagating distances. When

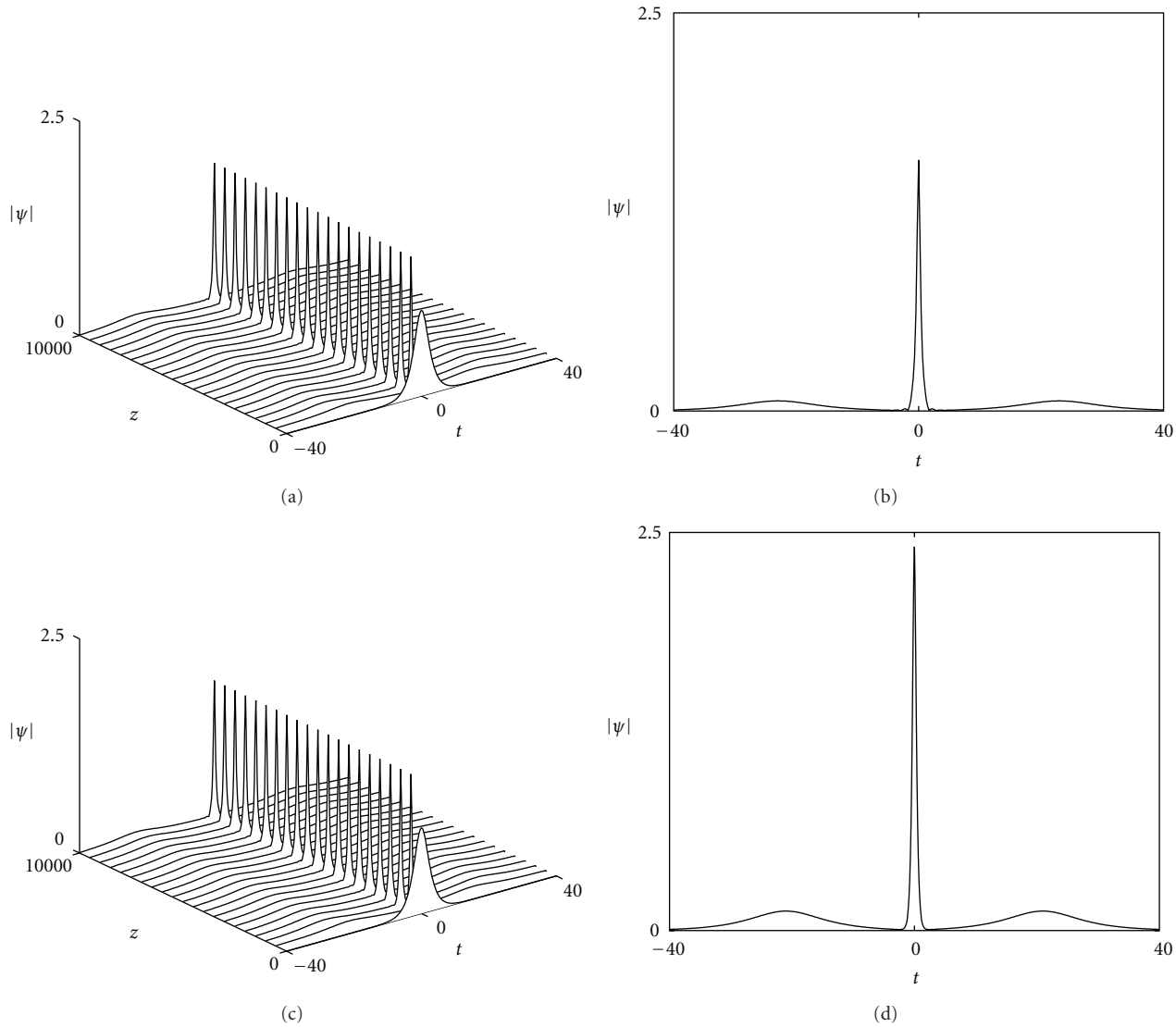

Figure 9: Transition dynamics observed in the anomalous dispersion regime. (a) and (b) Simulations of the full governing equations at $g_0 = 1.9$ ((a) and (c)) and the corresponding pulse profile ((b) and (d)). (c) and (d) Simulations of the SGLE at $g_0 = 2.25$ ((a) and (c)) and the corresponding pulse profile ((b) and (d)). The rest of the parameters in the simulations are $D = 0.4$, $\alpha_1 = 0$, $\alpha_2 = 0.82\pi$, $\alpha_3 = 0.1\pi$, $\alpha_p = 0.45\pi$, $K = 0.1$, $\Gamma = 0.1$, $e_0 = 1$, and $\tau = 0.1$. The initial conditions in all the simulations are $\psi(0,t) = \operatorname{sech} 0.5t$ (from [29], 2011, IEEE).

g_0 exceeds a critical value, the tall central pulse experiences a slight decrease in amplitude. At the same time, one of the side pulses is attenuated while the other one is amplified to the height of the central pulse, thus forming a double-pulse solution. The results found here match with those in a recent study on the CQGLE [49].

The transition dynamics are more subtle in the normal dispersion regime as depicted in Figure 10. Similar to the case of anomalous dispersion, a periodic structure with a tall central pulse and two flat side pulses is quickly developed (see Figures 10(a) and 10(b)). However, this periodic structure is unstable and eventually loses its stability after several thousand cavity round trips. A transient chaotic evolution is then observed followed by a stable copropagation of two well-separated pulses with different amplitudes. While the CQGLE (Figures 10(c) and 10(d)) is able to give a general qualitative approximation to the transitional state observed in the full simulation (Figures 10(a) and 10(b)), the SGLE model (Figures 10(e) and 10(f)) additionally gives a precise description of the transient chaotic behavior. This feature of the SGLE dynamics clearly demonstrates the improved description of the true discrete cavity dynamics.

4.2.3. Unphysical Blow-Up of Pulses. As mentioned in the beginning of the section, the field ψ governed by the CQGLE may experience a blow-up with certain waveplate/polarizer settings when condition (20) is not satisfied. This blow-up is unphysical since energy is always lost when the electric field

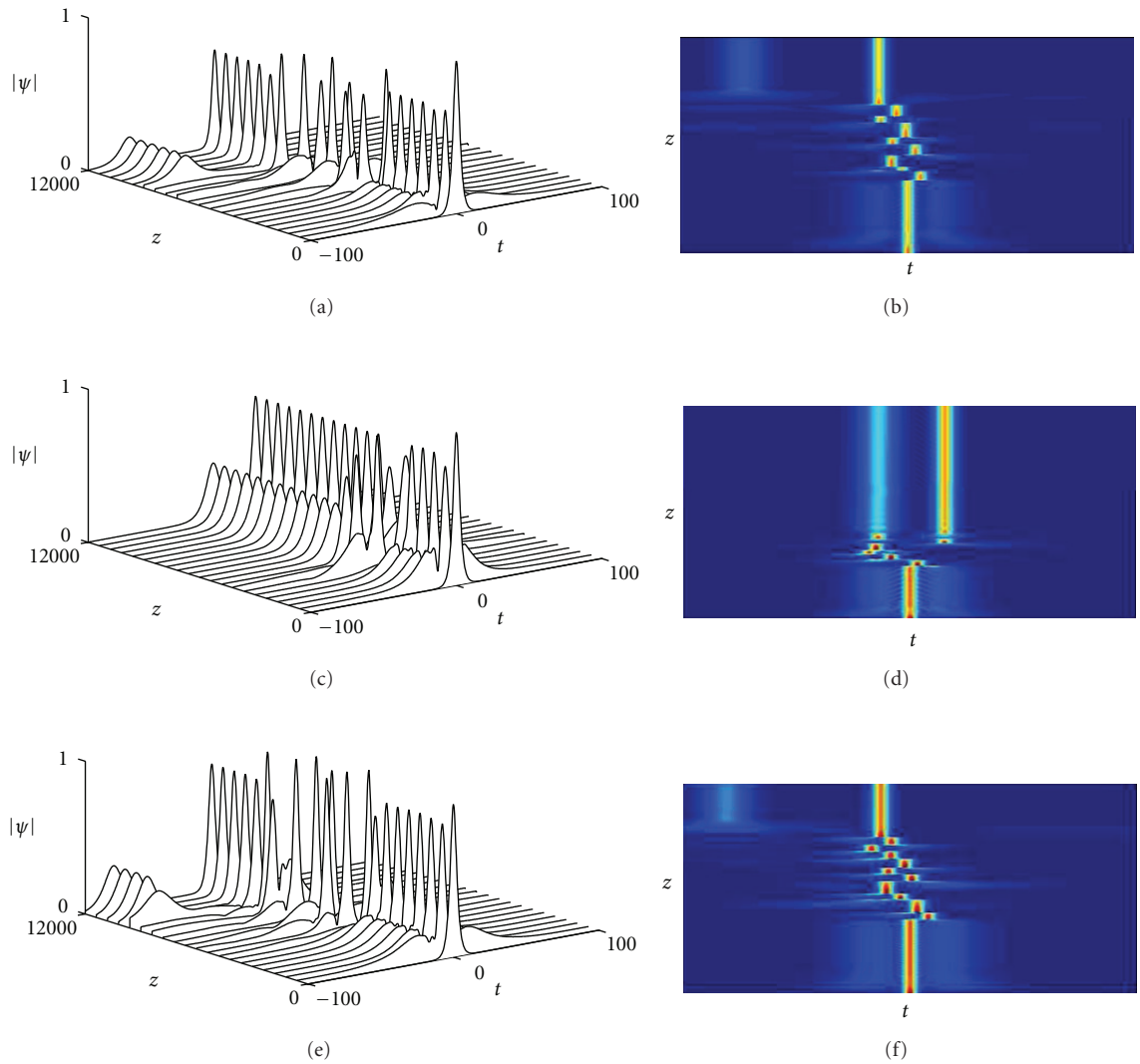

Figure 10: Periodic evolution observed in the full governing equations ((a) and (b), $g_0 = 2.27$), CQGLE ((c) and (d), $g_0 = 2.2$), and SGLE ((e) and (f), $g_0 = 2.2$). The simulated evolutions are shown in (a), (c), and (e) and the corresponding pseudocolor plots are shown in (b), (d), and (f). The rest of the parameters in the simulations are $D = -0.4$, $\alpha_1 = 0.1\pi$, $\alpha_2 = 0.554\pi$, $\alpha_3 = 0.23\pi$, $\alpha_p = 0.43\pi$, $K = 0.1$, $\Gamma = 0.1$, $e_0 = 1$, and $\tau = 0.2$. The initial conditions in all the simulations are $\psi(0,t) = \operatorname{sech} 0.5t$ (from [29], 2011, IEEE).

passes through the mode-locking elements and is a result of the finite truncation of the periodic transmission function $\log Q$. It is our intent to show that the artificial restriction (20) is unnecessary for modeling the laser cavity.

To show that the SGLE does not have the above limitations, we study the transmission function $T(|\psi|^2)$ which can be defined as the sum of the linear loss and the nonlinear dissipation. The transmission function of the CQGLE (T_{cq}) and the SGLE (T_s) are given by

$$T_{\text{cq}}\left(|\psi|^2\right) = -\delta + \beta|\psi|^2 + \mu|\psi|^4,$$
$$T_s\left(|\psi|^2\right) = -\Gamma + Re\left(\log Q\left(|\psi|^2\right)\right). \tag{22}$$

In the last equation, the imaginary part of the logarithmic term is neglected since it is not responsible for intensity discrimination and energy transfer. The imaginary terms only act to shift the intensity-dependent index of refraction response due to the field intensity. Shown in Figure 11 are the transmission curves for the CQGLE (blue dotted line) and SGLE (red solid line) at two different quarter-waveplate angles (Figure 11(a): $\alpha_2 = 0.554\pi$, Figure 11(b): $\alpha_2 = 0.4\pi$). The transmission function T_{cq} of the CQGLE is quadratic in the field power $|\psi|^2$. It curves downward at $\alpha_2 = 0.554\pi$ and upward at $\alpha_2 = 0.4\pi$. Figure 12 illustrates the pulse evolutions for the full governing equations (Figures 12(a) and 12(b)), CQGLE (Figures 12(c) and 12(d)), and the SGLE (Figures 12(e) and 12(f)) corresponding to the two α_2 values considered in Figure 11. At $\alpha_2 = 0.554\pi$ (Figures 12(a),

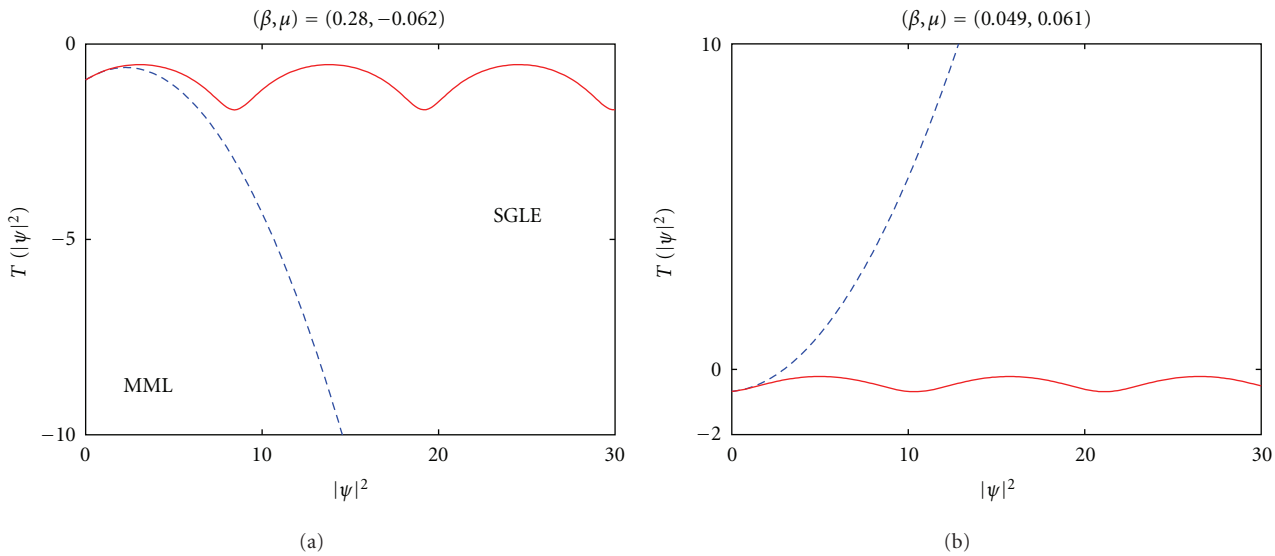

Figure 11: The transmission curve for the CQGLE (blue dashed line) and SGLE (red solid line) for $\alpha_2 = 0.554\pi$ (a) and $\alpha_2 = 0.4\pi$ (b). The rest of the parameters are $\alpha_1 = 0.1\pi$, $\alpha_3 = 0.23\pi$, $\alpha_p = 0.43\pi$, $\Gamma = 0.1$, $e_0 = 1$, and $K = 0.1$ (from [29], 2011, IEEE).

12(c), and 12(e)), the evolutions governed by all three models are always of finite amplitude. Blowing up of pulses is observed in the CQGLE at $\alpha_2 = 0.4\pi$ since self-saturation is impossible when both the nonlinear coefficients β and μ are positive (Figures 12(b), 12(d) and 12(f)). For both α_2 values considered, the SGLE does not have the problem of unphysical blow-up since it incorporates the full transmission $\log Q$ induced by the waveplates and polarizer. This allows for a drastically broader and more realistic range of waveplate/polarizer settings for which stable solutions can be achieved.

4.2.4. High-Energy Mode-Locking. As illustrated in Figure 6, the CQGLE uses a quadratic polynomial in the field power $|\psi|^2$ (see (22)) to approximate the full sinusoidal transmission. This can severely restrict the maximum amplitude a single pulse can reach before it splits. Figure 13 shows the tallest possible stable pulse generated by the full governing equations (black dash-dot line), CQGLE (red dashed line), and SGLE (green solid line) at two different half-waveplate angles α_3. These pulses are recorded right before the MPI occurs when the pumping strength g_0 exceeds the multipulsing threshold. At $\alpha_3 = 0.2\pi$ (Figure 13(a)), the full and the SGLE models produce pulses with amplitudes of about 3.1. The total cavity energy, which is given by the L^2-norm

$$E = \int_{-\infty}^{\infty} |\psi|^2 dt, \tag{23}$$

is calculated for each model. For the SGLE, the limiting pumping strength $g_0 = 3.58$ gives a pulse energy of $E = 4.52$. For the full model, the tallest pulse has an energy of $E = 3$ with pumping strength of $g_0 = 3.38$. One can see that the limiting g_0 value for a stable single-pulse operation in the present case is higher than that for a double-pulse operation ($g_0 = 2.7$) shown in Figure 7. The energy confined in each individual pulse of the double-pulse solution shown in Figure 7 is $E = 2.37$ for the SGLE and $E = 1.11$ for the full governing equations, which is significantly less than the energy output in the present case. The limiting pumping strength for the CQGLE model is only $g_0 = 2.51$, and the resulting pulse does not match well with the full simulation and the SGLE since it is much shorter and wider. With the same set of parameters, the maximum energy in the single-pulse solution of the CQGLE is $E = 2.87$, which is only approximately 60% of the SGLE model.

At $\alpha_3 = 0.25\pi$ (Figure 13(b)), the maximum pulse amplitudes allowed in both the full and the SGLE models increase to about 4. The corresponding pulse energies are $E = 6.58$ ($g_0 = 11.7$) and $E = 8.516$ ($g_0 = 15.4$), respectively, which are about twice the *total* energy of the double-pulse solutions shown in Figure 7. This is a remarkable achievement in terms of maximizing the energy output of the laser without going through multi pulsing. On the other hand, such a high-intensity pulse is not supported by the CQGLE with the parameters considered. In particular, expressions (19) reveal that the transmission T_{cq} of the CQGLE (c.f. (22)) is characterized by $\beta = -0.63$ and $\mu = 5.74$. At high intensities, the quintic gain always dominates the cubic loss and consequently leads to an unphysical blow-up of the solution, as happens in this case.

The above simulations show that, indeed, the SGLE can support high-intensity pulses with enormous energies observed in the full governing system, including those that are unpredicted by the CQGLE model. Although these simulations are done with anomalous dispersion, similar trends are also observed in the normal dispersion regime. Given the vast parameter space of the SGLE, it is possible to obtain other types of interesting mode-locking dynamics such as soliton shaking and period doubling bifurcation [24, 53]. The ability to support, model, and characterize high-intensity and high-energy mode-locked solutions is the key reason for our development of the proposed SGLE theory. In the work

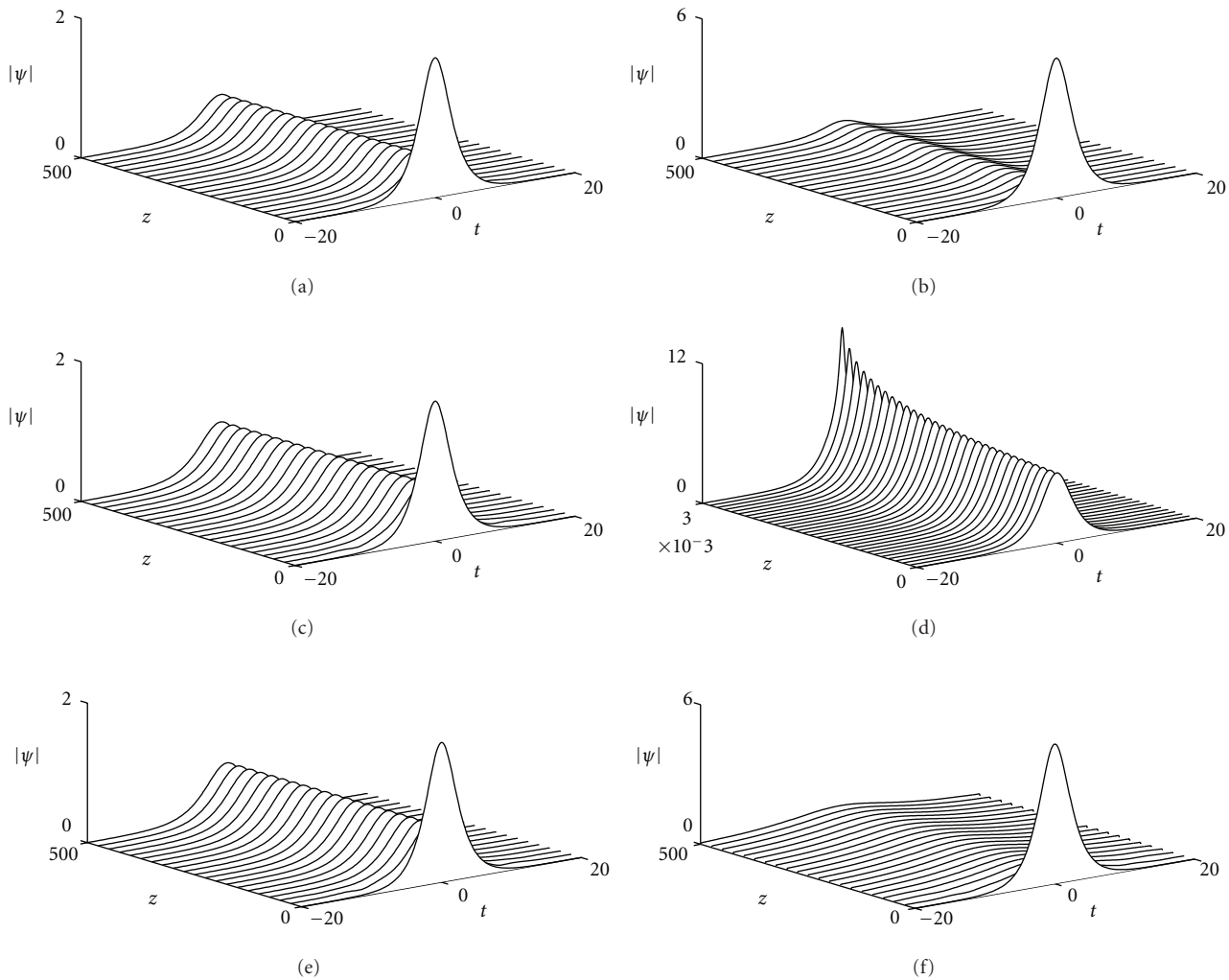

Figure 12: Pulse evolution predicted by the full governing equations ((a) and (b)), CQGLE ((c) and (d)), and SGLE ((e) and (f)). The plots on the left ((b), (d), and (f)) column correspond to the left (b) in Figure 11. The initial conditions for the plots on the left are $\psi(0,t) = 2\ \mathrm{sech}\ 0.5t$, while those for the right plots are $\psi(0,t) = 6\,\mathrm{sech}\ 0.5t$. The dispersion and pumping strength in all the simulations are $D = -0.4$ and $g_0 = 2$ (from [29], 2011, IEEE).

by Renninger et al. [37], it was found that a number of high-energy pulsed solutions existed in the CQGLE with both positive cubic (β) and quintic (μ) nonlinearities. The SGLE discussed here may provide for an effective way to stabilize such high-energy solutions. Ultimately, it is critical in modern mode-locked lasers to understand how to achieve pulses with maximal energy. The SGLE theory provides a basis for exploring such pulses.

5. Summary

We have studied the phenomenon of dissipative soliton resonance (DSR) in the context of the CQGLE and have extended previous findings to coefficients that can be explicitly related to the settings of the ring cavity laser depicted in Figure 1. In addition to the constant gain model, which was studied previously [45, 46], DSR is also achievable in the physically relevant case of saturating gain, but it is subjected to the onset of MPI if the cavity is not carefully engineered. Specifically, we found that there is a critical normal cavity dispersion D_c above which the DSR phenomenon is favored over MPI. Due to its linear chirp profile, the wide pulse created by DSR may be compressed effectively by linear dispersive delay lines, thus forming a short, intense pulse with enormous amount of energy.

In addition to varying the cavity dispersion D, high-energy mode-locked pulses can also be achieved by carefully adjusting the waveplate/polarizer settings, which in turn alters the characteristics of the sinusoidal transmission. The SGLE (sinusoidal Ginzburg-Landau equation) theory predicts that one can significantly increase the maximum pumping strength g_0 allowed before pulse splitting occurs. The resulting high-intensity single pulses can deliver significantly more energy than previous theoretical predictions by

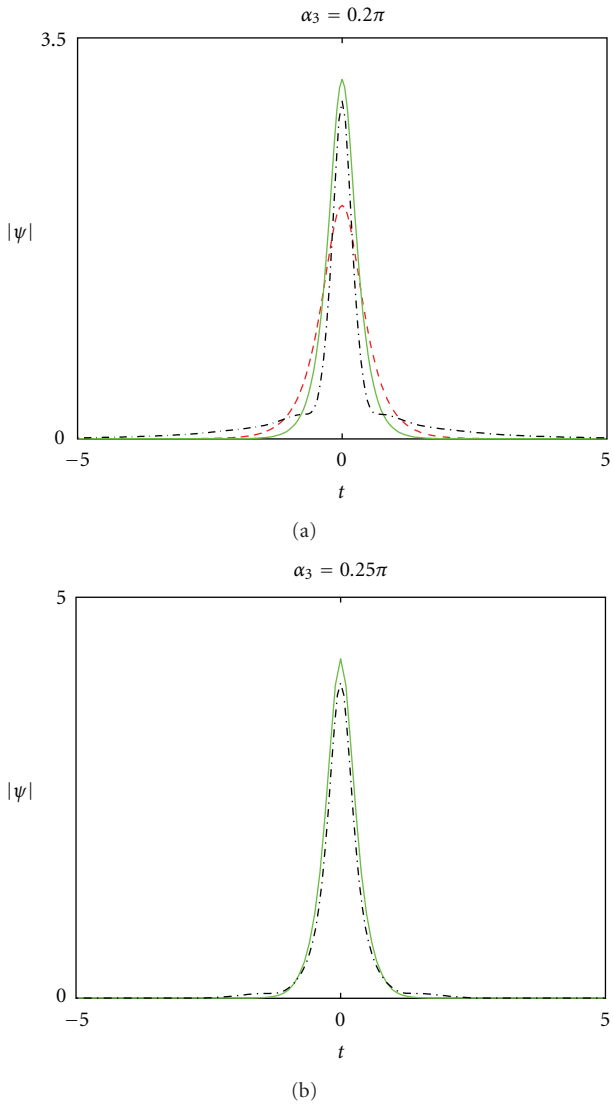

Figure 13: Stable single-pulse solution with the largest possible amplitude of the full governing system (black dash-dot curve), CQGLE (red dashed curve), and SGLE (green solid curve) at $\alpha_3 = 0.2\pi$ (a) and $\alpha_3 = 0.25\pi$ (b). The rest of the parameters are $D = 0.4$, $\tau = 0.1$, $e_0 = 1$, $\Gamma = 0.1$, $\alpha_1 = 0$, $\alpha_2 = 0.49\pi$, $\alpha_p = 0.45\pi$, and $K = 0.1$. The initial conditions are $\psi(0, t) = 0.5\ \mathrm{sech}\, t$ (from [29], 2011, IEEE).

the conventional CQGLE and are thus practically important to high-power applications. These pulses can exist in the parameter regime that is not allowed by the existing theories [6]. Thus, the SGLE can be used as an excellent design tool for enhancing the energy output of the laser. The current theoretical treatment of DSR and periodic transmission illustrate how the orders of magnitude increase in pulse energy can be achieved in order to make fiber lasers directly competitive with leading solid state mode-locking configurations. The tremendous benefits of fiber lasers in terms of cost, readily available technology, and ease of use lend importance to the theoretical developments proposed in this dissertation. DSR in the context of the SGLE will be investigated in the future in order to bring the pulse energy to an even higher level.

Acknowledgments

J. N. Kutz acknowledges support from the National Science Foundation (NSF) (DMS-1007621) and the US Air Force Office of Scientific Research (AFOSR) (FA9550-09-0174). W. Renninger and F. Wise acknowledge the support by the National Science Foundation (ECCS-0901323) and the National Institutes of Health (EB002019). Ph. Greulu acknowledges the support from the Agence Nationale de la Recherche (Grant ANR-2010-BLANC-0417-01-SOLICRISTAL).

References

[1] H. A. Haus, "Mode-locking of lasers," *IEEE Journal on Selected Topics in Quantum Electronics*, vol. 6, no. 6, pp. 1173–1185, 2000.

[2] I. N. Duling III and M. L. Dennis, *Compact Sources of Ultrashort Pulses*, Cambridge University Press, 1995.

[3] J. N. Kutz, "Mode-locked soliton lasers," *SIAM Review*, vol. 48, no. 4, pp. 629–678, 2006.

[4] C. Spielmann, P. F. Curley, T. Brabec, E. Winter, and F. Krausz, "Generation of sub-20 fs mode-locked pulses from Ti:sapphire laser," *Electronics Letters*, vol. 28, no. 16, pp. 1532–1534, 1992.

[5] A. Komarov, H. Leblond, and F. Sanchez, "Multistability and hysteresis phenomena in passively mode-locked fiber lasers," *Physical Review A*, vol. 71, no. 5, Article ID 053809, 9 pages, 2005.

[6] E. Ding and J. N. Kutz, "Operating regimes, split-step modeling, and the Haus master mode-locking model," *Journal of the Optical Society of America B*, vol. 26, no. 12, pp. 2290–2300, 2009.

[7] H. A. Haus, J. G. Fujimoto, and E. P. Ippen, "Analytic theory of additive pulse and Kerr lens mode locking," *IEEE Journal of Quantum Electronics*, vol. 28, no. 10, pp. 2086–2096, 1992.

[8] K. Tamura, H. A. Haus, and E. P. Ippen, "Self-starting additive pulse mode-locked erbium fibre ring laser," *Electronics Letters*, vol. 28, no. 24, pp. 2226–2228, 1992.

[9] H. A. Haus, E. P. Ippen, and K. Tamura, "Additive-pulse modelocking in fiber lasers," *IEEE Journal of Quantum Electronics*, vol. 30, no. 1, pp. 200–208, 1994.

[10] M. E. Fermann, M. J. Andrejco, Y. Silberberg, and M. L. Stock, "Passive mode-locking by using nonlinear polarization evolution in a polarizing-maintaining erbiumdoped fiber laser," *Optics Letters*, vol. 29, p. 447, 1993.

[11] I. N. Duling, "Subpicosecond all-fibre erbium laser," *Electronics Letters*, vol. 27, no. 6, pp. 544–545, 1991.

[12] D. J. Richardson, R. I. Laming, D. N. Payne, V. J. Matsas, and M. W. Phillips, "Self-starting, passively modelocked erbium fiber laser based on the amplifying Sagnac switch," *Electronics Letters*, vol. 27, p. 542, 1991.

[13] M. L. Dennis and I. N. Duling, "High repetition rate figure eight laser with extracavity feedback," *Electronics Letters*, vol. 28, no. 20, pp. 1894–1896, 1992.

[14] F. Ö. Ilday, F. W. Wise, and T. Sosnowski, "High-energy femtosecond stretched-pulse fiber laser with a nonlinear optical loop mirror," *Optics Letters*, vol. 27, no. 17, pp. 1531–1533, 2002.

[15] Q. Bao, H. Zhang, Y. Wang et al., "Atomic-layer craphene as a saturable absorber for ultrafast pulsed lasers," *Advanced Functional Materials*, vol. 19, no. 19, pp. 3077–3083, 2009.

[16] H. Zhang, D. Tang, R. J. Knize, L. Zhao, Q. Bao, and K. P. Loh, "Graphene mode locked, wavelength-tunable, dissipative soliton fiber laser," *Applied Physics Letters*, vol. 96, no. 11, Article ID 111112, 3 pages, 2010.

[17] N. N. Akhmediev and A. Ankiewicz, *Dissipative Solitons*, Springer, 2005.

[18] J. L. Proctor and J. N. Kutz, "Passive mode-locking by use of waveguide arrays," *Optics Letters*, vol. 30, no. 15, pp. 2013–2015, 2005.

[19] J. Proctor and J. N. Kutz, "Nonlinear mode-coupling for passive mode-locking: application of waveguide arrays, dual-core fibers, and/or fiber arrays," *Optics Express*, vol. 13, no. 22, pp. 8933–8950, 2005.

[20] K. Intrachat and J. N. Kutz, "Theory and simulation of passive modelocking dynamics using a long-period fiber grating," *IEEE Journal of Quantum Electronics*, vol. 39, no. 12, pp. 1572–1578, 2003.

[21] A. Chong, J. Buckley, W. Renninger, and F. Wise, "All-normal-dispersion femtosecond fiber laser," *Optics Express*, vol. 14, no. 21, pp. 10095–10100, 2006.

[22] A. Chong, W. H. Renninger, and F. W. Wise, "All-normal-dispersion femtosecond fiber laser with pulse energy above 20 nJ," *Optics Letters*, vol. 32, no. 16, pp. 2408–2410, 2007.

[23] A. Chong, W. H. Renninger, and F. W. Wise, "Properties of normal-dispersion femtosecond fiber lasers," *Journal of the Optical Society of America B*, vol. 25, no. 2, pp. 140–148, 2008.

[24] F. Li, P. K. A. Wai, and J. N. Kutz, "Geometrical description of the onset of multipulsing in mode-locked laser cavities," *Journal of the Optical Society of America B*, vol. 27, no. 10, pp. 2068–2077, 2010.

[25] A. Komarov, H. Leblond, and F. Sanchez, "Quintic complex Ginzburg-Landau model for ring fiber lasers," *Physical Review E*, vol. 72, no. 2, Article ID 025604, 4 pages, 2005.

[26] B. C. Collings, S. T. Cundiff, N. N. Akhmediev, J. M. Soto-Crespo, K. Bergman, and W. H. Knox, "Polarization-locked temporal vector solitons in a fiber laser: experiment," *Journal of the Optical Society of America B*, vol. 17, no. 3, pp. 354–365, 2000.

[27] J. M. Soto-Crespo, N. N. Akhmediev, and V. V. Afanasjev, "Stability of the pulselike solutions of the quintic complex Ginzburg-Landau equation," *Journal of the Optical Society of America B*, vol. 13, no. 7, pp. 1439–1449, 1996.

[28] J. M. Soto-Crespo, N. N. Akhmediev, V. V. Afanasjev, and S. Wabnitz, "Pulse solutions of the cubic-quintic complex Ginzburg-Landau equation in the case of normal dispersion," *Physical Review E*, vol. 55, no. 4, pp. 4783–4796, 1997.

[29] E. Ding, E. Shlizerman, and J. N. Kutz, "Generalized master equation for high-energy passive mode-locking: the sinusoidal Ginzburg-Landau equation," *IEEE Journal of Quantum Electronics*, vol. 47, no. 5, pp. 705–714, 2011.

[30] G. P. Agrawal, *Nonlinear Fiber Optics*, Academic Press, 2001.

[31] A. Hasegawa, *Optical Solitons in Fibers*, Springer, 2003.

[32] C. R. Menyuk, "Nonlinear pulse propagation in birefringent optical fibers," *IEEE Journal of Quantum Electronics*, vol. 23, no. 2, pp. 174–176, 1987.

[33] C. R. Menyuk, "Pulse propagation in an elliptically birefringent Kerr medium," *IEEE Journal of Quantum Electronics*, vol. 25, no. 12, pp. 2674–2682, 1989.

[34] D. Y. Tang, W. S. Man, and H. Y. Tam, "Stimulated soliton pulse formation and its mechanism in a passively mode-locked fibre soliton laser," *Optics Communications*, vol. 165, no. 4, pp. 189–194, 1999.

[35] D. Y. Tang, L. M. Zhao, B. Zhao, and A. Q. Liu, "Mechanism of multisoliton formation and soliton energy quantization in passively mode-locked fiber lasers," *Physical Review A*, vol. 72, no. 4, Article ID 043816, 9 pages, 2005.

[36] D. Y. Tang, W. S. Man, H. Y. Tam, and P. D. Drummond, "Observation of bound states of solitons in a passively mode-locked fiber laser," *Physical Review A*, vol. 64, no. 3, Article ID 033814, 3 pages, 2001.

[37] W. H. Renninger, A. Chong, and F. W. Wise, "Dissipative solitons in normal-dispersion fiber lasers," *Physical Review A*, vol. 77, no. 2, Article ID 023814, 4 pages, 2008.

[38] P. E. Langridge, G. S. McDonald, W. J. Firth, and S. Wabnitz, "Self-sustained mode locking using induced nonlinear birefringence in optical fibre," *Optics Communications*, vol. 97, no. 3-4, pp. 178–182, 1993.

[39] H. Leblond, M. Salhi, A. Hideur, T. Chartier, M. Brunel, and F. Sanchez, "Experimental and theoretical study of the passively mode-locked ytterbium-doped double-clad fiber laser," *Physical Review A*, vol. 65, no. 6, Article ID 063811, 9 pages, 2002.

[40] M. Salhi, H. Leblond, and F. Sanchez, "Theoretical study of the stretched-pulse erbium-doped fiber laser," *Physical Review A*, vol. 68, no. 3, Article ID 033815, 7 pages, 2003.

[41] M. J. Ablowitz and H. Segur, *Solitons, Nonlinear Evolution Equations and Inverse Scattering*, Cambridge University Press, New York, NY, USA, 1991.

[42] T. Kapitula, J. N. Kutz, and B. Sandstede, "Stability of pulses in the master mode-locking equation," *Journal of the Optical Society of America B*, vol. 19, no. 4, pp. 740–746, 2002.

[43] T. Kapitula, N. Kutz, and B. Sandstede, "The Evans function for nonlocal equations," *Indiana University Mathematics Journal*, vol. 53, no. 4, pp. 1095–1126, 2004.

[44] E. Ding, P. Grelu, and J. N. Kutz, "Dissipative soliton resonance in a passively mode-locked fiber laser," *Optics Letters*, vol. 36, no. 7, pp. 1146–1148, 2011.

[45] P. Grelu, W. Chang, A. Ankiewicz, J. M. Soto-Crespo, and N. Akhmediev, "Dissipative soliton resonance as a guideline for high-energy pulse laser oscillators," *Journal of the Optical Society of America B*, vol. 27, no. 11, pp. 2336–2341, 2010.

[46] N. Akhmediev, J. M. Soto-Crespo, and P. Grelu, "Roadmap to ultra-short record high-energy pulses out of laser oscillators," *Physics Letters, Section A*, vol. 372, no. 17, pp. 3124–3128, 2008.

[47] S. Namiki, E. P. Ippen, H. A. Haus, and C. X. Yu, "Energy rate equations for mode-locked lasers," *Journal of the Optical Society of America B*, vol. 14, no. 8, pp. 2099–2111, 1997.

[48] C. R. Jones and J. N. Kutz, "Stability of mode-locked pulse solutions subject to saturable gain: computing linear stability with the Floquet-Fourier-Hill method," *Journal of the Optical Society of America B*, vol. 27, no. 6, pp. 1184–1194, 2010.

[49] E. Ding, E. Shlizerman, and J. N. Kutz, "Modeling multipulsing transition in ring cavity lasers with proper orthogonal decomposition," *Physical Review A*, vol. 82, no. 2, Article ID 023823, 10 pages, 2010.

[50] B. G. Bale and J. N. Kutz, "Variational method for mode-locked lasers," *Journal of the Optical Society of America B*, vol. 25, no. 7, pp. 1193–1202, 2008.

[51] B. G. Bale, K. Kieu, J. N. Kutz, and F. Wise, "Transition dynamics for multi-pulsing in mode-locked lasers," *Optics Express*, vol. 17, no. 25, pp. 23137–23146, 2009.

[52] Q. Xing, L. Chai, W. Zhang, and C. Y. Wang, "Regular, period-doubling, quasi-periodic, and chaotic behavior in a self-mode-locked Ti:sapphire laser," *Optics Communications*, vol. 162, no. 1, pp. 71–74, 1999.

[53] J. M. Soto-Crespo, P. Grelu, N. Akhmediev, and N. Devine, "Soliton complexes in dissipative systems: vibrating, shaking, and mixed soliton pairs," *Physical Review E*, vol. 75, no. 1, Article ID 016613, 9 pages, 2007.

Hindawi Publishing Corporation
International Journal of Optics
Volume 2012, Article ID 475056, 6 pages
doi:10.1155/2012/475056

Research Article

Tunable Single-Longitudinal-Mode High-Power Fiber Laser

Jonas K. Valiunas and Gautam Das

Department of Physics, Lakehead University, 955 Oliver Road, Thunder Bay, ON, Canada P7B 5E1

Correspondence should be addressed to Gautam Das, gdas@lakeheadu.ca

Received 1 October 2011; Accepted 5 December 2011

Academic Editor: Frédéric Smektala

We report a novel CW tunable high-power single-longitudinal-mode fiber laser with a linewidth of ~9 MHz. A tunable fiber Bragg grating provided wavelength selection over a 10 nm range. An all-fiber Fabry-Perot filter was used to increase the longitudinal mode spacing of the laser cavity. An unpumped polarization-maintaining erbium-doped fiber was used inside the cavity to eliminate mode hopping and increase stability. A maximum output power of 300 mW was produced while maintaining single-longitudinal-mode operation.

1. Introduction

Fiber lasers are established as robust and reliable devices with a variety of applications in industry and medicine due to their unique characteristics, such as all-fiber designs, compact size, cost-effective production and operation, and the no need for realignment or external cooling. High-power single-wavelength and multiwavelength infrared fiber lasers are very attractive for applications in optical communications, sensing, spectroscopy, biomedical instrumentation, and nonlinear optics. The continued progress in fiber pumping techniques, advanced fiber designs, and fabrication processes, as well as the availability of high-power pump diodes, has assisted in the development of high-power fiber lasers [1–5]. Fiber lasers have found applications in temperature and strain sensors [6–11], medical diagnostics [12–14], and industrial processing [15]. High-power fiber lasers using erbium-ytterbium codoped fibers as the gain medium, which operates in the eye-safe (1.5 μm to 1.6 μm) spectral range, can now compete with traditional solid-state bulk lasers. The applications of recently reported single-wavelength [16, 17] and multiwavelength [18, 19] high-power fiber lasers were limited due to large linewidth of the lasing wavelength, multi-longitudinal-mode oscillations, small tuning range, and complex designs.

In this paper we present a novel tunable, high-power, single-wavelength, single-longitudinal-mode, fiber ring laser.

2. Experimental Setup

The experimental setup of the fiber laser is shown in Figure 1. The resonant cavity consists of a high-power polarization-independent optical isolator (OI), which guaranteed the unidirectional propagation and thus eliminated the spatial hole-burning effects [20]; an all-fiber polarization controller; a commercially available tunable fiber Bragg grating (TFBG) with a tuning range of 10 nm (1565 nm–1575 nm); a 4 m long double-clad erbium-ytterbium codoped (DC-EYDF) fiber with core/cladding diameters of 10/131 μm which was used as the gain medium. In general to produce high output power from a ring laser, a longer length of the active medium is required which leads to a smaller longitudinal-mode spacing and a narrower laser linewidth. A double-clad erbium-ytterbium codoped fiber (DC-EYDF), with high conversion efficiency, as an active medium eliminated the requirement for a long length of the active medium. The DC-EYDF (CorActive) had much greater absorption and coupling efficiency compared to that of a circularly symmetric double-clad fiber due to its hexagonal inner cladding [21]. An unpumped polarization-maintaining erbium-doped fiber (PM-EDF) was used as a saturable absorber (SA) inside the cavity to reduce the mode hopping of the lasing wavelength. The SA had an elliptical core with dimensions, peak absorption, cut-off wavelength, and a numerical aperture of $3.8 \times 14.8\,\mu$m, 10.8 dB/m at 1535 nm, 1371 nm, and 0.15, respectively. To

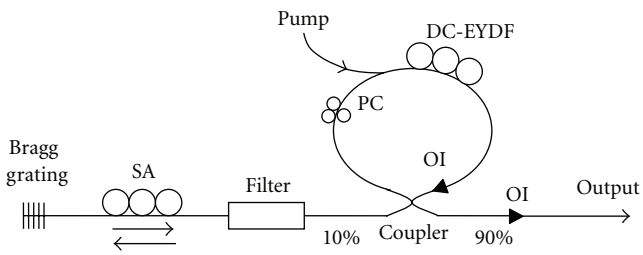

Figure 1: Experimental setup of our fiber laser.

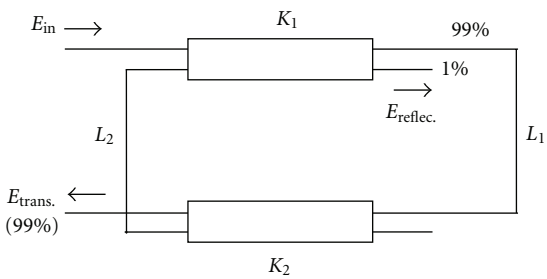

Figure 2: All-fiber Fabry-Perot filter [22].

increase the effective longitudinal-mode spacing and stability of the laser wavelength, an all-fiber Fabry-Perot filter with wide free spectral range (FSR) was used within the cavity. The Fabry-Perot filter was formed by splicing two 2×2 single-mode fused fiber couplers (split ratio 99 : 1) together (Figure 2), which helped to eliminate the mode hopping of the laser wavelength by increasing the effective longitudinal-mode spacing of the laser cavity [22]. In general the length of the ring cavity is longer than the FP filter cavity; thus, the presence of the filter inside the cavity produces the vernier effect and increases the longitudinal-mode spacing of the cavity [23–25]. In our experiment the length of the Fabry-Perot filter was ~0.4 m, which corresponds to a free spectral range of $FSR_{FP} \approx 514$ MHz. A multimode laser diode at 976 nm with a maximum output power of 10 W was used to pump the laser cavity. A multimode fused fiber coupler (6×1 multimode pump power combiner) was used as a 976/1550 nm wavelength division multiplexing coupler to couple power from the pump laser into the DC-EYDF fiber. The fiber Bragg grating, saturable absorber, Fabry-Perot filter, and the ring together formed an overlapping cavity configuration, where the output of the ring resonator was modulated by the output of the Fabry-Perot cavity. The output of the laser was obtained from the 90% port of a 90 : 10 fused fiber coupler. A polarization-independent optical isolator was used to reduce any back reflection from the output port. The output of the laser was monitored using an optical spectrum analyzer with a resolution of 1.25 GHz, a scanning Fabry-Perot spectrum analyzer (SFPSA) of resolution 6.7 MHz and a power meter.

3. Results and Discussions

Figure 3 shows the tunable characteristics of the laser for an input pump power of ~700 mW at a wavelength of 976 nm.

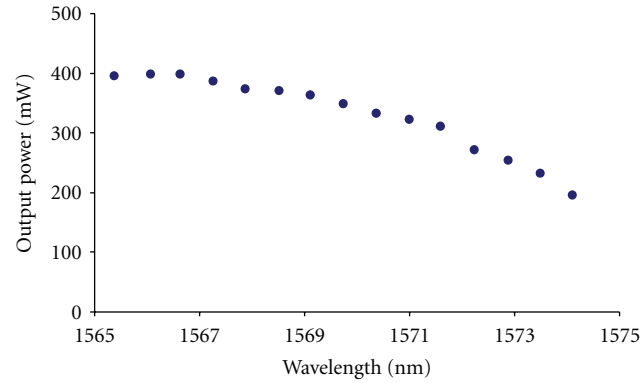

Figure 3: Output power of the laser at ~0.6 nm intervals from 1565 nm to 1575 nm.

The laser was tunable from 1565 nm to 1575 nm, which was limited by the tunability of the grating, and the minimum tunable interval was 0.01 nm. The nonuniform output power over the wavelength range is due to the erbium-ytterbium codoped fiber emission, which decreases in this region.

Figure 4(a) shows the output of the laser obtained by the OSA without any saturable absorber inside the cavity, and Figure 4(b) is the input-output characteristics of the laser. The maximum power obtained from the laser was ~600 mW for a pump power of ~1300 mW at $\lambda = 1565.52$ nm. The threshold pump power and efficiency of the laser were ~200 mW and ~49%, respectively. The effective length of our ring cavity and the length of the FP filter were ~9 m and ~0.4 m, respectively. The corresponding FSR of the ring cavity was ~24 MHz and of the Fabry-Perot filter was ~514 MHz. The theoretical resonance linewidth (FWHM) of the FP filter was 2 MHz. The presence of this filter resulted in an effective longitudinal-mode spacing of 514 MHz for the laser cavity.

To study the longitudinal-mode structure of the laser, a scanning Fabry-Perot spectrum analyzer (FSR = 2 GHz) of resolution 6.7 MHz and NuView software developed by EXFO was used. The maximum output power with single-longitudinal-mode oscillation was less than 50 mW with a 4 m DC-EYDF. The experiment was repeated using 1 m of DC-EYDF fiber to reduce the effective cavity length to 6 m, which corresponds to longitudinal-mode spacing of 34 MHz. This allowed us to maintain a lasing wavelength that was single-longitudinal-mode and free from mode hopping to a maximum output of 100 mW. Figure 5 was obtained using the scanning Fabry-Perot spectrum analyzer (SFPSA) and confirmed the single-longitudinal-mode oscillation of the laser. At high output powers, the laser suffered from mode hopping and oscillations of multiple longitudinal modes.

In order to improve the stability of the laser output at high power, we incorporated an unpumped polarization maintaining erbium-doped fiber as a saturable absorber into the cavity. A series of experiments were carried out using 1 m, 3 m, and 5 m of PM-EDF to find the optimum length of the SA, which would increase the stability of the lasing wavelength, by reducing mode hopping, and without

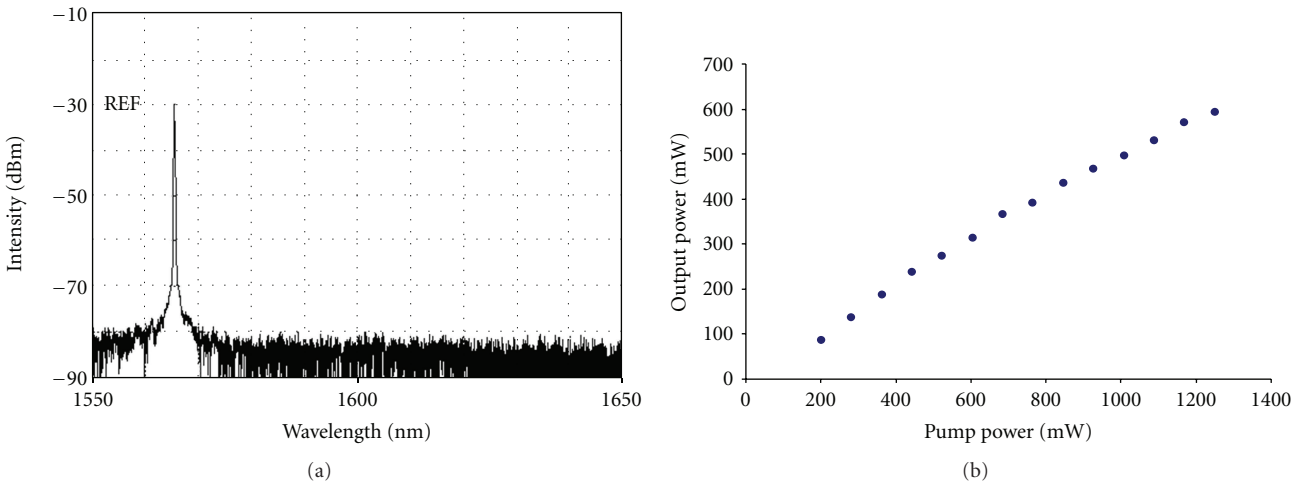

Figure 4: (a) Output of the laser obtained with OSA; (b) input-output characteristics of the laser without the SA for $\lambda = 1565.52$ nm.

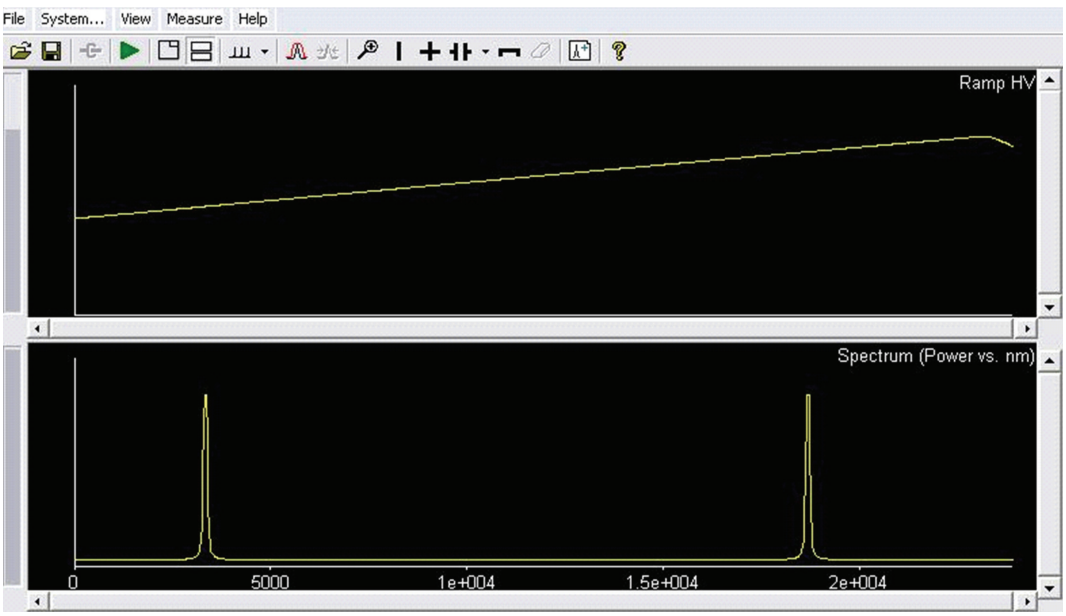

Figure 5: Output of the laser obtained using scanning Fabry-Perot spectrum analyzer.

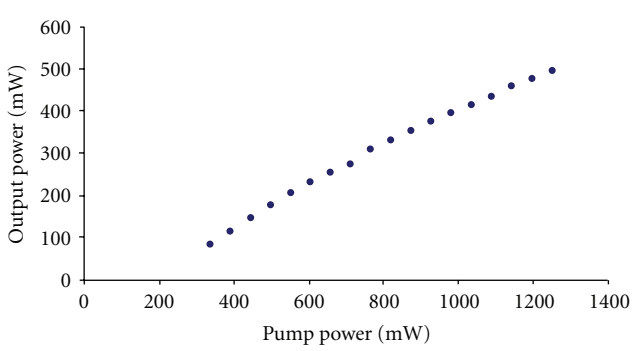

Figure 6: Input-output characteristics of the laser with 5 m of SA inside the cavity at $\lambda = 1565.52$ nm.

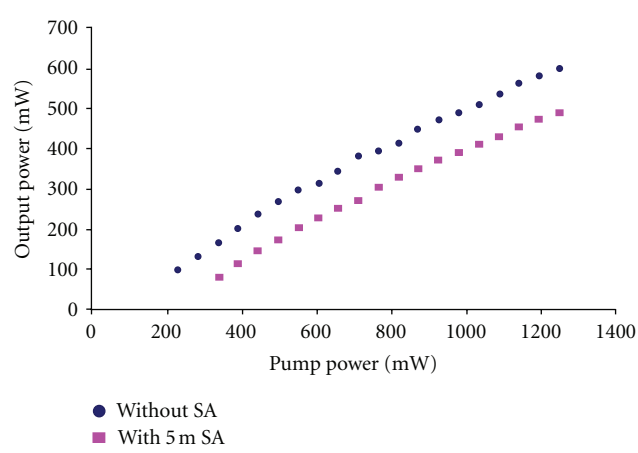

Figure 7: Input-output characteristics of the laser with and without the SA.

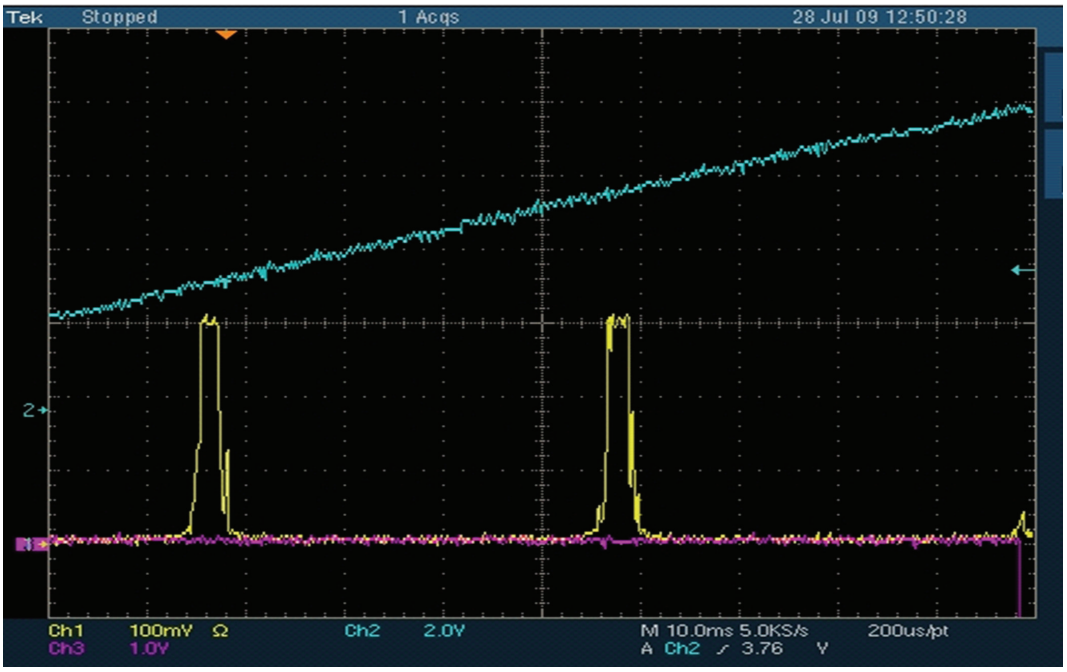

Figure 8: Output of the laser obtained using SFPSA when the laser operated in the pulsed regime.

largely attenuating the laser output power. We found that the 5 m PM-EDF provided the stability needed while still allowing a high output power. Figure 6 shows the input-output characteristics of the laser with a SA inside the cavity. The polarization controller and polarization-maintaining EDF helped to produce and maintain quasilinearly polarized light inside the saturable absorber and thus increased the stability of the transient grating. The maximum output power achieved while maintaining single-longitudinal-mode operations was more than 300 mW with the SA.

The counter-propagating light waves inside the saturable absorber formed a transient grating with a reflection bandwidth of 20 MHz. The transient grating acted as a tracking filter, where the central frequency tracked the lasing mode and thus eliminated mode hopping. The transient grating was capable of adjusting itself, within a few milliseconds, to any sudden changes in the laser cavity, such as changes in temperature or other environmental fluctuations [26]. The effective cavity length of the laser was ~19 m, which corresponds to a longitudinal-mode spacing of ~10 MHz. Though the longer cavity length decreased the longitudinal-mode spacing of the cavity, the presence of the Fabry-Perot filter increased the longitudinal-mode spacing to 514 MHz.

Figure 7 shows the input-output characteristics of the laser with and without the SA, which shows the effect of SA on the output of the laser. The laser was oscillating in single-longitudinal-mode when more than 300 mW of output power was produced.

The 3-dB linewidth of the laser at lower power (~100 mW) was ~8.75 MHz as measured by the SFPSA and NuView software. The linewidth of the laser at high pump power was larger when compared to the theoretical value based on the Schawlow-Townes formula [27]. We found that the linewidth of the laser increased with increasing pump power. It was reported that the wider linewidth in the erbium-ytterbium-co-doped fiber laser is due to the temperature fluctuations induced by the pump intensity noise inside the core of the fiber or due to four-wave mixing between various longitudinal modes in the laser cavities [28–31].

We found that it was possible to maintain the relative phases of the modes by adjusting the polarization controller plates inside the cavity when the laser was oscillating in multiple longitudinal modes. This phenomenon is referred to as passive mode locking and produced periodic pulses at the output of the laser. Figure 8 shows the output of the laser at high power obtained from the scanning Fabry-Perot spectrum analyzer, after achieving mode locking through adjustments of the polarization controller plates inside the cavity. At the optimum location of the polarization controller plates all the modes collapsed into a single pulse with a large bandwidth (~60 MHz). This result was due to the presence of the saturable absorber inside the cavity and is known as passive mode locking. We also found that even without the presence of the saturable absorber the laser produces pulses at high powers when the polarization controller plates were adjusted properly. This is another type of passive mode locking known as nonlinear polarization rotation mode locking.

Figure 9 is the output of the laser when operated at high power and was obtained with a high-speed photo detector (2.5 GHz) and an oscilloscope with a 1 GHz bandwidth. Thus, we could operate the laser in either CW or pulsed mode by adjusting the polarization controller plates inside the cavity.

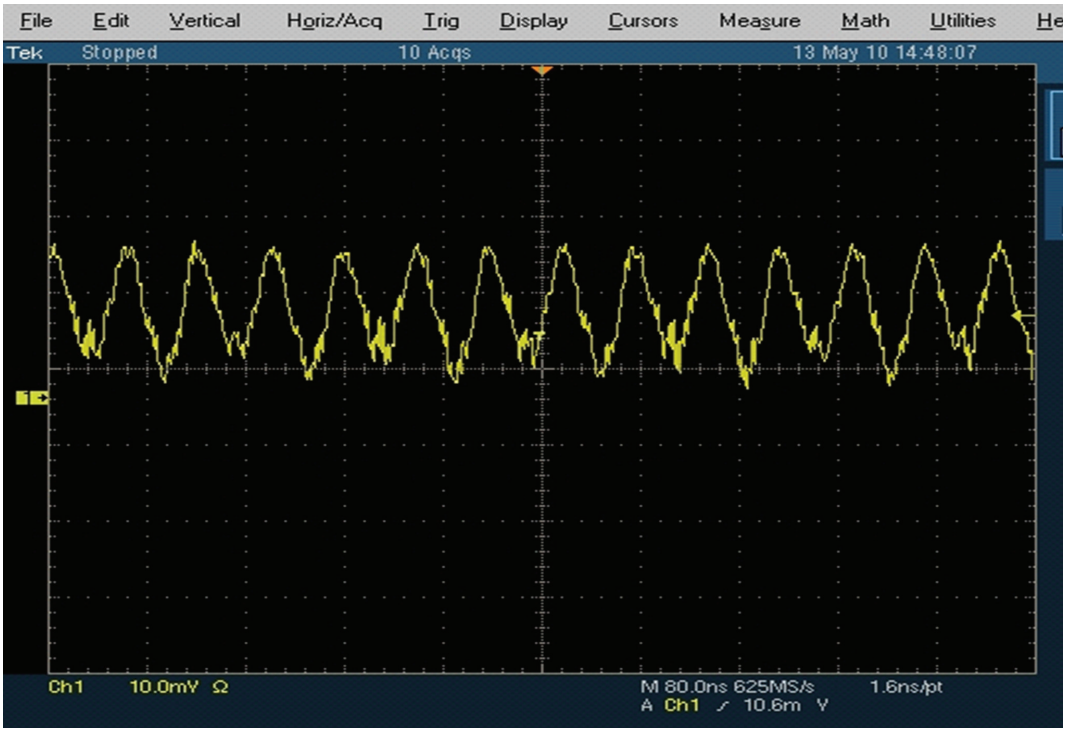

Figure 9: Output of the laser obtained from the oscilloscope.

4. Conclusion

We have demonstrated a high-power single-wavelength, single-longitudinal-mode fiber laser. The laser was free from mode hopping to a maximum output power of ~300 mW. The laser was tunable over 1565 nm to 1575 nm and had a linewidth of ~9 MHz. The presence of SA inside the cavity increased the stability of the laser. The laser could be operated in the CW and pulsed mode through manipulation of the polarization controller. Due to the narrow linewidth and high output power, this laser could find applications in developing sensor based on nonlinear effects such as stimulated Brillouin scattering.

References

[1] J. Nilsson, J. K. Sahu, Y. Jeong et al., "High power fiber lasers: new developments," in *Proceedings of the SPIE: Advances in Fiber Devices*, vol. 4974, pp. 50–59, January 2003.

[2] J. K. Sahu, Y. Jeong, C. Codemard et al., "Tunable narrow linewidth high power erbium: ytterbium co-doped fiber laser," in *Proceedings of the Conference on Lasers and Electro-Optics (CLEO '04)*, vol. 1, pp. 159–160, May 2004.

[3] M. Laroche, P. Jander, W. A. Clarkson, J. K. Sahu, J. Nilsson, and Y. Jeong, "High power cladding-pumped tunable Er, Yb-doped fibre laser," *Electronics Letters*, vol. 40, no. 14, pp. 855–856, 2004.

[4] Y. Jeong, J. K. Sahu, D. N. Payne, and J. Nilsson, "ytterbium-doped large-core fiber laser with 1.36 kW continuous-wave output power," *Optics Express*, vol. 12, no. 25, pp. 6088–6092, 2004.

[5] Y. Jeong, J. Nilsson, J. K. Sahu et al., "Single-mode plane-polarized ytterbium-doped large-core fiber laser with 633-W continuous-wave output power," *Optics Letters*, vol. 30, no. 9, pp. 955–957, 2005.

[6] Q. Wang, L. Zhang, C. Sun, and Q. Yu, "Multiplexed fiber-optic pressure and temperature sensor system for down-hole measurement," *IEEE Sensors Journal*, vol. 8, no. 11-12, Article ID 4666724, pp. 1879–1883, 2008.

[7] S. Watson, M. J. Gander, W. N. MacPherson et al., "Laser-machined fibers as Fabry-Perot pressure sensors," *Applied Optics*, vol. 45, no. 22, pp. 5590–5596, 2006.

[8] S. Trpkovski, S. A. Wade, S. F. Collins, and G. W. Baxter, "Er^{3+}: Yb^{3+} doped fibre with embedded FBG for simultaneous measurement of temperature and longitudinal strain," *Measurement Science and Technology*, vol. 16, no. 2, pp. 488–496, 2005.

[9] J. Mandal, S. Pal, T. Sun, K. T. V. Grattan, A. T. Augousti, and S. A. Wade, "Bragg grating-based fiber-optic laser probe for temperature sensing," *IEEE Photonics Technology Letters*, vol. 16, no. 1, pp. 218–220, 2004.

[10] H. H. Kee, G. P. Lees, and T. P. Newson, "All-fiber system for simultaneous interrogation of distributed strain and temperature sensing by spontaneous Brillouin scattering," *Optics Letters*, vol. 25, no. 10, pp. 695–697, 2000.

[11] M. Niklès, L. Thévenaz, and P. A. Robert, "Simple distributed fiber sensor based on Brillouin gain spectrum analysis," *Optics Letters*, vol. 21, no. 10, pp. 758–760, 1996.

[12] P. M. Talaia, A. Ramos, I. Abe et al., "Plated and intact femur strains in fracture fixation using fiber Bragg gratings and strain gauges," *Experimental Mechanics*, vol. 47, no. 3, pp. 355–363, 2007.

[13] E. J. Seibel, R. E. Carroll, J. A. Dominitz et al., "Tethered capsule endoscopy, a low-cost and high-performance alternative

technology for the screening of esophageal cancer and Barrett's esophagus," *IEEE Transactions on Biomedical Engineering*, vol. 55, no. 3, pp. 1032–1042, 2008.

[14] Y. Sasaki, S. Tanosaki, J. Suzuki et al., "Fundamental imaging properties of transillumination laser CT using optical fiber applicable to bio-medical sensing," *IEEE Sensors Journal*, vol. 3, no. 5, pp. 658–667, 2003.

[15] L. Quintino, A. Costa, R. Miranda, D. Yapp, V. Kumar, and C. J. Kong, "Welding with high power fiber lasers—a preliminary study," *Materials and Design*, vol. 28, no. 4, pp. 1231–1237, 2007.

[16] A. Polynkin, P. Polynkin, M. Mansuripur, and N. Peyghambarian, "Single-frequency fiber ring laser with 1 W output power at 1.5 μm," *Optics Express*, vol. 13, no. 8, pp. 3179–3184, 2005.

[17] Y. Jeong, C. Alegria, J. K. Sahu et al., "A 43-W C-band tunable narrow-linewidth erbium-ytterbium codoped large-core fiber laser," *IEEE Photonics Technology Letters*, vol. 16, no. 3, pp. 756–758, 2004.

[18] Z. G. Lu, F. G. Sun, G. Z. Xiao, P. Lin, and P. Zhao, "High-power multiwavelength Er^{3+}-Yb^{3+} codoped double-cladding fiber ring laser," *IEEE Photonics Technology Letters*, vol. 17, no. 9, pp. 1821–1823, 2005.

[19] X. X. Yang, L. Zhan, Q. S. Shen, and Y. X. Xia, "High-power single-longitudinal-mode fiber laser with a ring Fabry-Pérot resonator and a saturable absorber," *IEEE Photonics Technology Letters*, vol. 20, no. 11, pp. 879–881, 2008.

[20] P. W. Milonni and J. H. Eberly, *Laser Physics*, John Wiley & Sons, New York, NY, USA, 2010.

[21] D. Kouznetsov and J. V. Moloney, "Efficiency of pump absorption in double-clad fiber amplifiers. II. Broken circular symmetry," *Journal of the Optical Society of America B*, vol. 19, no. 6, pp. 1259–1263, 2002.

[22] G. Das and Z. J. Chaboyer, "Single-wavelength fiber laser with 250 mW output power at 1.57 μm," *Optics Express*, vol. 17, no. 10, pp. 7750–7755, 2009.

[23] P. Urquhart, "Compound optical-fiber-based resonators," *Journal of the Optical Society of America A*, vol. 5, no. 6, pp. 803–812, 1988.

[24] S. J. Hogeveen and H. Vandestadt, "Fabry-Perot interferometers with 3 mirrors," *Applied Optics*, vol. 25, no. 22, pp. 4181–4184, 1986.

[25] H. Vandestadt and J. M. Muller, "Multimirror Fabry-Perot interferometers," *Journal of the Optical Society of America A*, vol. 2, no. 8, pp. 1363–1370, 1985.

[26] Y. Cheng, J. T. Kringlebotn, W. H. Loh, R. I. Laming, and D. N. Payne, "Stable single-frequency traveling-wave fiber loop laser with integral saturable-absorber-based tracking narrow-band-filter," *Optics Letters*, vol. 20, no. 8, pp. 875–877, 1995.

[27] A. L. Schawlow and C. H. Townes, "Infrared and optical masers," *Physical Review*, vol. 112, no. 6, pp. 1940–1949, 1958.

[28] N. Y. Voo, P. Horak, M. Ibsen, and W. H. Loh, "Anomalous linewidth behavior in short-cavity single-frequency fiber lasers," *IEEE Photonics Technology Letters*, vol. 17, no. 3, pp. 546–548, 2005.

[29] P. Horak, N. Y. Voo, M. Ibsen, and W. H. Loh, "Pump-noise-induced linewidth contributions in distributed feedback fiber lasers," *IEEE Photonics Technology Letters*, vol. 18, no. 9, pp. 998–1000, 2006.

[30] M. A. Lapointe and M. Piché, "Linewidth of high-power fiber lasers," in *Proceedings of the SPIE: Photonics North*, vol. 7386, pp. 73860S-1–73860S-8, 2009.

[31] V. Roy, M. Piché, F. Babin, and G. W. Schinn, "Nonlinear wave mixing in a multilongitudinal-mode erbium-doped fiber laser," *Optics Express*, vol. 13, no. 18, pp. 6791–6797, 2005.